University of New Hampshire

University of New Hampshire Scholars' Repository

Doctoral Dissertations Student Scholarship

Fall 2015

Unraveling depositional and diagenetic signals in magnetic susceptibility in methane-bearing sediments along the Indian, Cascadia, and Japanese margins

Stephen C. Phillips
University of New Hampshire, Durham

Follow this and additional works at: https://scholars.unh.edu/dissertation

Recommended Citation

Phillips, Stephen C., "Unraveling depositional and diagenetic signals in magnetic susceptibility in methane-bearing sediments along the Indian, Cascadia, and Japanese margins" (2015). *Doctoral Dissertations*. 2226.
https://scholars.unh.edu/dissertation/2226

This Dissertation is brought to you for free and open access by the Student Scholarship at University of New Hampshire Scholars' Repository. It has been accepted for inclusion in Doctoral Dissertations by an authorized administrator of University of New Hampshire Scholars' Repository. For more information, please contact Scholarly.Communication@unh.edu.

UNRAVELING DEPOSITIONAL AND DIAGENETIC SIGNALS IN MAGNETIC SUSCEPTIBILITY IN METHANE-BEARING SEDIMENTS ALONG THE INDIAN, CASCADIA, AND JAPANESE MARGINS

BY

STEPHEN C. PHILLIPS

BS Geology, Michigan Technological University, 2004

MS Earth Sciences, University of New Hampshire, 2007

DISSERTATION

Submitted to the University of New Hampshire
in Partial Fulfillment of
the Requirements for the Degree of
Doctor of Philosophy
in
Oceanography

September, 2015

This thesis/dissertation has been examined and approved in partial fulfillment of the requirements for the degree of Doctor of Philosophy in Oceanography by:

Dr. Joel E. Johnson, dissertation director
Associate Professor of Geology
Department of Earth Sciences

Dr. Julia G. Bryce
Associate Professor of Geochemistry
Department of Earth Sciences

Dr. William C. Clyde
Professor of Geology
Department of Earth Sciences

Dr. Jo Laird
Associate Professor of Geology
Department of Earth Sciences

Dr. John W. Pohlman
Research Geochemist
U.S. Geological Survey

Original approval signatures are on file with the University of New Hampshire Graduate School.

TABLE OF CONTENTS

ACKNOWLEDGEMENTS

I would like to thank my adviser Joel Johnson for the guidance and support along the way. I would also like to thank my committee: Will Clyde, Jo Laird, Julie Bryce, and John Pohlman for their support and advice during this work.

For the work presented in Chapter 1, I wish to thank the NGHP01 shipboard scientific party for the collection and initial interpretation of these cores, including Joel Johnson, Liviu Giosan, and Kelly Rose, who were co-authors on this manuscript. I thank Ellen Roosen for assistance with core curation and sampling at the WHOI Seafloor Samples Laboratory. I thank Andrew Ouimette and Rachel Mixon of the UNH Stable Isotope Laboratory for assistance with carbon and nitrogen isotope samples, and Kate Korotky for picking foraminifera used to develop the age model. I thank Lars Paulson and Emily Raterman for assistance with XRD sample preparation at the DOE National Energy Technology Lab in Albany, Oregon. I thank Corrine Disenhof (DOE NETL-URS Corp.) and Jake Setera (UNH) for assistance with the particle size analysis and Linda Kalnejais (UNH) for assistance with silica analysis. This project was supported by DGH India, U.S. Geological Survey (contract #07CRSA0708), and the UNH Natural Resources and Earth System Science Program Student Support Fund.

For the work presented in Chapter 2, I thank the expedition scientists of ODP Leg 204 and IODP Expedition 311, as well as the captain and crew of the D/V JOIDES Resolution for recovery of sediments and initial analyses and interpretations. I would like to thank Joel Johnson, Will Clyde, WeiLi Hong, and Marta Torres for discussions and guidance as co-authors. I thank Phil Rumford and student workers at the IODP Gulf Coast Repository in College Station, TX for sediment core sub-sampling. I greatly appreciate the assistance of David Houpt and Shari Hilding-Kronforst at the Ocean Drilling and Sustainable Earth Science XRF facility at Texas

A&M University. I thank Eduardo Miranda, Corinne Disenhof for assistance with CHN analysis, and Jake Setera with CHNS and IRM analysis. I thank Ben Harlow and the Washington State University Isotope Core for EA-IR-MS analysis. I thank Lora Wingate and the University of Michigan Stable Isotope Laboratory. This research was supported by the U.S. Department of Energy National Energy Technology Laboratory Methane Hydrates Program Award # DE-FE0010120, a Geological Society of America Graduate Student Grant, and the American Association of Petroleum Geologists Paul Danheim Nelson Named Grant.

For the work presented in Chapter 3, I would like to thank the Captain and crew of *D/V Chikyu* and all IODP Expedition 337 Scientists for core collection and initial onboard analysis. I would like to thank Joel Johnson, Will Clyde, Jake Setera, and Natascha Riedinger who are co-authors on this manuscript. This research was supported by a Post-Expedition Award from the Consortium for Ocean Leadership – U.S. Science Support Program. I thank Sam Taylor for helpful discussions on magnetic mineralogy, and Tomoyuki Hori for helpful discussions about iron reduction.

LIST OF TABLES

CHAPTER 1

CHAPTER 2

CHAPTER 3

LIST OF FIGURES

CHAPTER 1

CHAPTER 2

CHAPTER 3

ABSTRACT

UNRAVELING DEPOSITIONAL AND DIAGENETIC SIGNALS IN MAGNETIC SUSCEPTIBILITY IN METHANE-BEARING SEDIMENTS ALONG THE INDIAN, CASCADIA, AND JAPANESE MARGINS

by

Stephen C. Phillips

University of New Hampshire, September, 2015

Magnetic susceptibility is a bulk measure that reveals variation in ferromagnetic mineral content. High-resolution measurement of magnetic susceptibility in ocean drilling records reveals variability that can be attributed to primary depositional processes and/or secondary diagenetic processes that occur after deposition. Each chapter of my dissertation investigates magnetic susceptibility records along with geochemical, mineralogical, and rock magnetic techniques in methane-bearing marine sediments along the Indian, Cascadia, and Japanese margins. The overall goal of this work is to improve the understanding of the effects of detrital and biogeochemical processes on magnetic mineralogy, and thus magnetic susceptibility, in these continental margin marine environments..

In the first study (Chapter 1; Phillips et al., 2014), using a multi-proxy approach, I investigated variation in productivity and weathering over the last 110,000 years in the northern Indian Ocean within the core Indian monsoon rainfall zone. These results reveal an increase in productivity due to reduced stratification and a decrease in weathering during the last glacial period due to a weakened summer monsoon. This work reveals a relationship between Zr/Rb and magnetic susceptibility that can be utilized to predict primary detrital magnetic susceptibility.

In the second study, I used an elemental analysis and rock magnetic approach to decouple detrital and diagenetic patterns in magnetic susceptibility at three sites along the Cascadia accretionary wedge. Each site reveals intervals of diagenetic loss in magnetic susceptibility that is balanced by an increase in sulfur due to dissolution of magnetite and precipitation of pyrite. The diagenetic loss of magnetic susceptibility is influenced by organic matter availability as well as upward methane flux.

In the third study, I used a rock magnetic approach to investigate the magnetic mineralogy in a deep sediment record down to ~2.5 km below the seafloor offshore northern Honshu, Japan. The magnetic susceptibility record reveals cm-scale increases that are likely the result of density sorting causing concentration of heavy minerals. The magnetic mineral assemblage is dominated by titanomagnetite with an increase in Ti-rich titanomagnetite associated with deeply buried (~2 km) coal beds. This change along the titanomagnetite solid solution series, may represent selective dissolution of Ti-poor, iron(III)-rich magnetite during microbial iron reduction since burial.

INTRODUCTION

Magnetic susceptibility is a measure of how readily a material can be magnetized in the presence of an applied field, and in essence, tracks the composition and concentration of ferromagnetic minerals within a material. In marine sediments, magnetic susceptibility is measured routinely using discrete sample, core logging, and/or wireline logging techniques. These measurements can be useful tools for first-order interpretation of depositional and diagenetic processes in a variety of environments (e.g. Verosub and Roberts, 1995; Liu et al., 2012). Often, magnetic susceptibility measurements are a mixed signal of both primary depositional and secondary diagenetic processes, in which a detrital magnetic mineral assemblage is altered by post-depositional reactions within the sediments. The utility of magnetic susceptibility measurements becomes more effective when these data are integrated with rock magnetic, geochemical, and mineralogical data to reveal a more complete picture of a complex natural system.

Primary detrital ferromagnetic minerals are carried to the ocean via weathering of terrestrial rocks and transferred to the ocean via fluvial (e.g. Canfield et al., 1997; Chakrapani and Subramanian, 1990), eolian (e.g. Lowrie and Heller, 1982; Doh et al., 1988), or glacial (e.g. Hall and King, 1989; Richter et al., 2001) transport. Further transport and reworking of ferrimagnetic minerals can occur on continental margins via mass flows such as turbidites (e.g. Karlin and Abella, 1994; Wynn et al., 2002), and these heavy minerals can be concentrated by winnowing (e.g. Shor et al., 1984; de Menocal et al., 1988). Aquatic magnetotactic bacteria can also contribute to the flux of magnetite to marine sediments (Bazylinski, 1996). After deposition, magnetotactic bacteria can precipitate magnetite or greigite (e.g. Karlin et al., 1987; Mann et al., 1990), and during early diagenesis, magnetic iron oxides can be dissolved and re-precipitated as paramagnetic and ferrimagnetic iron oxides (e.g. Canfield and Berner, 1987; Sweeney and Kaplan, 1973).

During scientific ocean drilling expeditions (e.g., the International Ocean Discovery Program/Integrated Ocean Drilling Program (IODP), the Ocean Drilling Program (ODP), Deep Sea Drilling Project (DSDP)) measurement of magnetic susceptibility using a multi-sensor core logger is a standard procedure that provides high resolution (cm-scale) data sets of magnetic susceptibility. Due to the interdisciplinary nature of most scientific drilling expeditions, downhole variation in magnetic susceptibility can provide a first-pass view of variation in magnetic mineral content that can serve to guide post-expedition research involving the geological and biogeochemical evolution of continental margins.

Each chapter of my dissertation is a project that further investigates patterns in magnetic susceptibility observed in records generated during scientific drilling expeditions. Chapter 1 is an investigation of cyclic variability in magnetic susceptibility, $CaCO_3$, and the $\delta^{13}C$ of total organic carbon (TOC) observed in Quaternary sediments of the Mahanadi Basin, offshore India (Phillips et al., 2014). In this work, monsoon-driven variation in weathering and productivity is inferred based on variation in $CaCO_3$, δ^{13}TOC, sedimentation rate, grain size distribution, magnetic susceptibility, and Zr/Rb. Based on a key result of the relationship of magnetic susceptibility and Zr/Rb from Chapter 1, I worked to decouple detrital and depositional signals in magnetic susceptibility at three sites along the Cascadia margin in Chapter 2. Chapter 2 links the role of sulfate reduction and anerobic oxidation of methane in producing intervals of reduced magnetic susceptibility. In Chapter 3, I use rock magnetic results to further understand the magnetic mineral assemblage driving magnetic susceptibility in an IODP record offshore northern Honshu. These results are interpreted in terms of provenance, depositional environment, and biogeochemical implications. Overall, the research presented in this dissertation integrates magnetic susceptibility with geochemical, rock magnetic and physical property data to more completely constrain and reconstruct the complex geological evolution preserved in methane and methane-hydrate rich continental margin settings.

1. MONSOON-INFLUENCED VARIATION IN PRODUCTIVITY AND LITHOGENIC SEDIMENT FLUX SINCE 110 KA IN THE OFFSHORE MAHANADI BASIN, NORTHERN BAY OF BENGAL

ABSTRACT

The Indian monsoon drives seasonal changes in precipitation and weathering across India as well as circulation and productivity in the northern Indian Ocean. Variation in paleo-monsoon intensity and its effect on productivity and lithogenic fluxes is poorly constrained in the Bay of Bengal. In this paper, I present analysis of a sediment record from the offshore Mahanadi Basin recovered during the Indian National Gas Hydrate Program Expedition 01 (Site NGHP-01-19B). I reconstruct variation in biogenic and lithogenic components during the last 110 kyr using measurements of total organic carbon (TOC), total nitrogen (TN), TOC/TN, $CaCO_3$, biogenic silica (BSi), δ^{13}TOC, δ^{15}TN, bulk mineralogy from X-ray diffraction, bulk and lithogenic grain size distribution, magnetic susceptibility, bulk density, and Ca, Br, and Zr/Rb from X-ray fluorescence (XRF). The mass-accumulation rate (MAR) of $CaCO_3$, a function of marine productivity, drastically increased between 70 ka and 10 ka under glacial conditions and is correlated to previously-documented elevated Asian dust fluxes and increased Bay of Bengal salinity during a weakened southwest monsoon. Decreased freshwater input over this period likely diminished stratification, allowing for increased mixing and nutrient availability, thus enhancing productivity despite weaker southwest monsoon winds. The MAR of lithogenic material is highest during the Holocene suggesting that sediment supply driven by monsoon intensity is a stronger control on margin sedimentation than sea level at the Mahanadi Basin. Over the entire record, magnetic susceptibility and XRF Zr/Rb are strongly correlated with $CaCO_3$, suggesting higher primary mineral input under a weakened southwest monsoon.

TOC/TN and δ^{13}TOC also increase under glacial conditions, suggesting higher relative input of terrestrial C4 organic matter. These results highlight the Mahanadi Basin as a supply-dominated margin where terrigenous sedimentation is strongly influenced by monsoon intensity, and that productivity is limited by variation in monsoon-driven stratification on glacial-interglacial timescales rather than a direct response to monsoon winds.

INTRODUCTION

The northern Indian Ocean and peninsular India are influenced by monsoon-driven environmental variability occurring on orbital and suborbital timescales (e.g. Clemens and Prell, 1990; Kutzback, 1981, Overpeck et al., 1996; Prell and Kutzbach, 1987; Sirocko et al., 1993). The modern Asian monsoon system varies in strength and precipitation across the region, and can be generally subdivided into the Indian, East Asian, and western North Pacific monsoons (Wang et al., 2001; Wang and Ho, 2002). The Indian monsoon system is a seasonal reversal in prevailing winds as a response to the migration of the intertropical convergence zone (ITCZ) driven by insolation of the Indian subcontinent and Tibetan Plateau (Chao, 2000; Chao and Chen, 2001; Gadgil, 2003). The summer monsoon, or southwest (SW) monsoon, occurs during the northward migration of the ITCZ and the resultant southwesterly winds result in wet, higher precipitation conditions over the Indian region. The winter monsoon, or northeast (NE) monsoon, occurs during the southward migration of the ITCZ and the resultant northeasterly winds produce drier conditions over the Indian region. The monsoon is influenced externally by teleconnections with northern high latitudes (e.g. Gupta et al., 2003; Schulz et al., 1998; Sirocko et al., 1996; Wang et al., 2001), Pacific Ocean (e.g. Krishnamurthy and Goswami, 2000; Kumar et al., 1999; Mehta and Lau, 1997), and Southern Hemisphere climate (Clemens and Oglesby, 1992; An et al., 2011). Uplift of the Tibetan Plateau during the Late Cenozoic intensified the

Asian monsoon and influenced global climate (Molnar et al., 1993; Raymo and Ruddiman, 1992; Ruddiman and Kutzback, 1989; Zachos et al., 2001). The specific timing of uplift-driven intensification remains unresolved, but ranges between 24 and 2.6 Ma (e.g. Clift et al., 2004; Clift, 2006; Nie et al., 2008; An et al., 2001).

The Asian monsoon influences 11 of the 20 rivers with the highest sediment discharge to the oceans (Milliman and Meade, 1983), and also acts as a driver of marine productivity (e.g. Brink et al., 1998; Brock et al., 1991; Curry et al., 1992; Liu et al., 2002), thus making the monsoon a major factor in terrigenous and marine biogenic sedimentation in the northern Indian Ocean and western Pacific Ocean. Past changes in the monsoon, on time scales ranging from decadal to millions of years, have been investigated through a wide array of paleoenvironmental and paleoceanographic proxies applied to records including marine sediments (e.g. Clift et al., 2008; Emeis et al., 1995; Oppo and Sun, 2005; Prell et al., 1980; Weber et al., 1997), loess and paleosol deposits (e.g. An et al., 1991, Ding et al., 2001; Guo et al., 2004; Kukla et al., 1988; Maher and Thompson, 1995; Quade and Cerling, 1995;), speleothems (e.g. Burns et al., 2002; Dykoski et al., 2005; Fleitman et al., 2007; Wang et al., 2001, 2008; Zhao et al., 2010), ice cores (e.g. Thompson et al., 2000), lake sediments (e.g. Enzel et al., 1999; Morrill et al., 2006; Wei and Gassse, 1999; Xiao et al., 1995), tree rings (e.g. Feng et al., 1999; Hughes et al., 1994), and corals (e.g. Charles et al., 2003; Tudhope et al., 1996). Like the modern monsoon system, regional variation in the monsoon system can be reflected in paleomonsoon records (Wang et al., 2003). Many unresolved questions remain in understanding the past and continued evolution of the monsoon (see Wang et al., 2005 for a review of these issues and proxy methods), particularly involving uncertainties in the timing of the monsoon (e.g. Caley et al., 2011; Clemens and Prell, 1990, 2007; Clemens et al., 2008, 2010; Kutzbach, 1981; Ruddiman et al., 2006).

As an archive for paleo-monsoon records, the northern Indian Ocean, the Bay of Bengal is relatively under-sampled compared to the Arabian Sea. In the Arabian Sea, the strength of the monsoon has been shown to influence terrigenous sediment flux (e.g. Caley et al., 2011; Clemens and Prell, 1990;1991; Clift and Gaedicke, 2002; deMenocal et al., 1991; Kumar et al., 2005), sea surface temperature (SST) and salinity (SSS) (e.g. Anand et al., 2008; Govil and Naidu, 2010; Prell et al., 1980;) and productivity (e.g. Altabet et al., 2002; Gupta et al., 2011; Hermelin and Shimmield, 1995; Kroon et al., 1991; Reichart et al., 1998; Schulz et al., 1998; Ziegler et al., 2010). Fewer records exist in the Bay of Bengal; however, the influence of the monsoon in the Bay of Bengal has been observed using terrigenous flux proxies (e.g. Burton and Vance, 2000; Colin et al., 1998; Weber et al., 1997), organic geochemical proxies (e.g. Fontugne and Duplessy, 1986; Ponton et al., 2012), and proxies of SST and salinity (e.g. Cullen et al., 1981; Prell et al., 1980; Govil and Naidu, 2011; Rashid et al., 2011; Schulenberg, 2011) that indicate monsoon-influenced changes in surface ocean conditions and terrestrial weathering on glacial-interglacial and suborbital timescales. The research presented here using a sediment core recovered during the Indian National Gas Hydrate Program Expedition 1 (NGHP01) provides an opportunity to investigate variability in lithogenic and biogenic sedimentary constituents in the western Bay of Bengal, as potential effects of monsoon-induced changes in erosion/weathering and biological productivity.

GEOLOGIC AND OCEANOGRAPHIC SETTING

Tectonic Setting and Terrigenous Inputs

The Mahandi Basin is a sedimentary basin on the eastern margin of India formed during the Jurassic rifting of Gondwanaland (Rao et al., 1997; Sastri et al., 1981; Subrahmanyam et al., 2008). The basin extends both onshore and offshore, and the post-rifting evolution of the basin has involved multiple marine transgressions and regressions (Fuloria, 1993). The Mahanadi River drains the Precambrian Eastern Ghat province (Rickers et al., 2001) including one of the richest mineral belts on the Indian sub-continent, resulting in higher concentrations of trace metals in suspended river sediments compared to other rivers in peninsular India (Chakrapani and Subramanian, 1990a). Kaolinite, chlorite, quartz, dolomite, and minor montmorillonite and illite are characteristic suspended sediments discharged by the Mahanadi River to the Bay of Bengal (Chakrapani and Subramanian, 1990a; Subramanian, 1980). The Mahanadi River discharges approximately 15 x 10^6 metric tons of sediment to the Bay of Bengal each year, dominated by the coarse silt-size fraction (Chakrapani and Subramanian, 1990b). The monsoon is the primary control of present-day sediment discharge in the Mahanadi Basin with 90% of the annual sediment delivery to the Bay of Bengal occurring between July and September during the summer monsoon (Chakrapani and Subramanian, 1990b).

Physical Oceanography and Biological Productivity

Surface ocean circulation in the Bay of Bengal is driven primarily by the Indian monsoon, and consists of seasonally-reversing gyres (Potemra et al., 1991; Schott and McCreary, 2001; Schott et al., 2009; Shetye et al., 1993; Varkey et al., 1996). These circulation patterns result in a seasonal reversal along the western boundary East India Coastal Current (EICC): northward during the SW monsoon and spring inter-monsoon, and southward during the NE monsoon and fall inter-monsoon (Shankar et al., 1996). During the SW monsoon, Ekman-driven coastal upwelling occurs along the eastern peninsular Indian margin, although this upwelling is limited to within 40 km of the coast due to stratification from enhanced freshwater input (Shetye et al., 1991). These major circulation patterns initiate mesoscale eddy currents in all seasons (e.g. Babu et al., 1991, 2003; Nuncio and Prasana Kumar, 2012; Prasana Kumar et al., 2004 Shetye et al., 1993). These seasonal variations also generate Kelvin waves along the east coast of India, which in turn instigate propagation of Rossby waves (Potemra et al., 1991; Yu et al., 1991) that can also initiate the incursion of the Southwest Monsoon Current into the Bay of Bengal east of Sri Lanka (Vinayachandran et al., 1999) during the summer monsoon. Intermediate water masses in the Bay of Bengal are sourced from primarily Indonesian Intermediate Water, Antarctic Intermediate Water and Red Sea Intermediate Water (You et al., 1998; Sengupta et al., 2013). Below 1500 m, deep waters are derived from beyond the northern Indian Ocean (Mantyla and Reid, 1995), but are primarily composed of Indian Ocean Deep Water (Varkey et al., 1996; Sengupta et al., 2013). Sediments in the Bay of Bengal are a source of nutrients and a sink of oxygen for bottom water (Broecker et al., 1980).

Seasonal variation in precipitation results in a large, seasonally-shifting salinity gradient in the surface waters of the Bay of Bengal. Annual average salinities in the mixed layer range from 27 to 35 ‰ increasing from the northern reaches of the bay to 5° N (Antonov et al., 2010; Talley, 2013; Varkey et al., 1996). This salinity gradient becomes more extreme during the summer monsoon due to increased precipitation, ranging from 21 to 35 ‰ along the north-south gradient. The water balance of the surface Bay of Bengal results in net precipitation and runoff gain of 63.7 cm during the summer monsoon, and net evaporation of 11.5 cm during the winter monsoon, resulting in an overall annual net excess of precipitation (Varkey et al., 1996).

Biological productivity in surface ocean of the Bay of Bengal is generally high but significantly less than that observed in the Arabian Sea, due to strong stratification driven by freshwater runoff that limits nutrient recycling by wind-driven mixing, as well as cloud cover and suspended particulates that disrupt light availability for phytoplankton (Gomes et al., 2000;

Madhupratap et al., 2003; Prasanna Kumar et al., 2002). During the summer monsoon, chlorophyll-a is approximately 4 to 5 times lower in the Bay of Bengal compared to the Arabian Sea (Prasanna Kumar et al., 2002). Productivity and downward particle flux is highest during the southwest monsoon, but also elevated during the northeast monsoon (Guptha et al., 1997). Overall, productivity in the Bay of Bengal is driven not by regional upwelling, like in the Arabian Sea, but by local upward pumping of nutrient-rich water by eddies most strongly during the southwest monsoon, but also during the northeast monsoon and inter-monsoon seasons (Prasanna Kumar et al., 2004, 2007; Vinayachandran and Mathew, 2003; Vidya and Prasanna Kumar, in press).

NGHP Site 19 Lithostratigraphy

Site NGHP-01-19B (Site 19) is located approximately 70 km offshore India (18° 58.6568'N, 85° 39.5202'E) at a water depth of 1422 m (Collett et al., 2008) (Fig. 1-1). Site 19 is bathymetrically shallower than the Bengal Fan, which contacts the lower continental slope of eastern India (Curray et al., 2003) at a depth of approximately 2000 m. Thus, terrigenous sedimentation at Site 19 is primarily influenced by peninsular India margin processes. Two holes were drilled and cored by advance piston core by D/V JOIDES Resolution at NGHP-01-19A and NGHP-01-19B to depths of 305 and 26 mbsf respectively.

Relative to deeper sections, the upper 75 m at Site 19A shows increased variability in magnetic susceptibility (Collett et al., 2008), bulk mineralogy (Phillips et al., 2014), total organic carbon (TOC) (Johnson et al., 2014), calcium carbonate ($CaCO_3$), and $\delta^{13}C$ relative to the Vienna Pee Dee Belemnite (VPDB) of organic carbon (δ^{13}TOC). Based on calcareous nannofossil biostratigraphy (Abel-Flores et al., 2014), this interval of increased and variable κ, $CaCO_3$, and

δ^{13}TOC corresponds to the past 1.96 Ma. In this study I seek to understand the source of this variation through measurement of lithogenic and biogenic components at a substantially higher resolution (every 10 cm) in the upper 11.5 m (past 110 kyrs) at NGHP-01-19B (Site 19B) by integrating elemental, isotopic and physical property data.

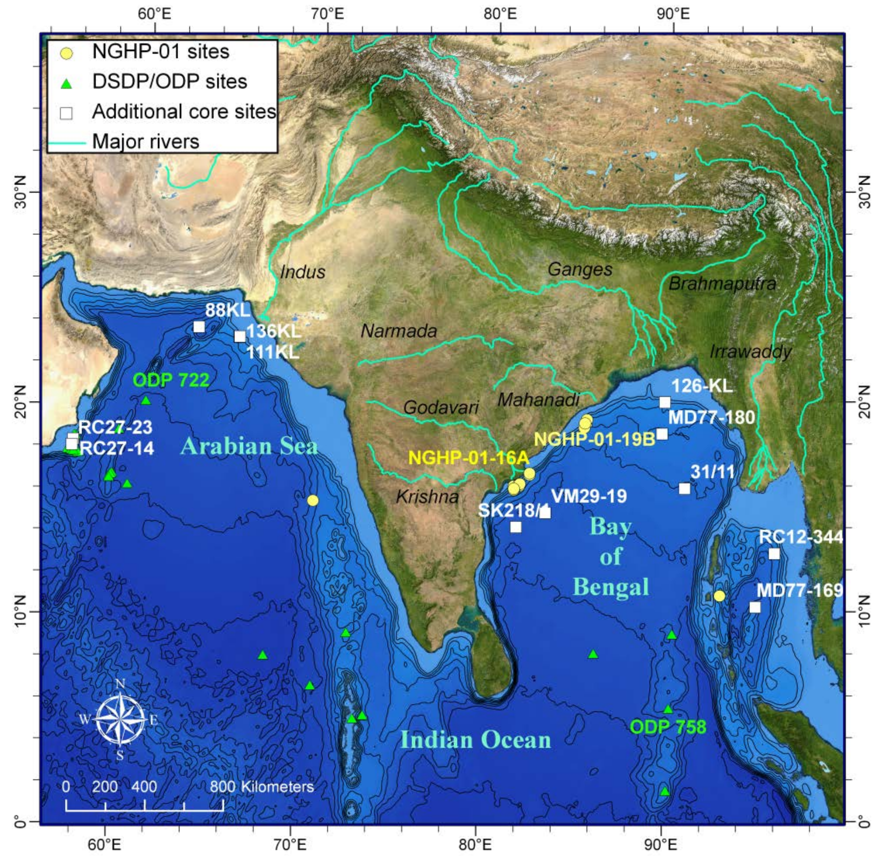

Figure 1-1. Location map showing the location of NGHP-01-19B and selected core locations where data are used or referenced in this study.

METHODS

Planktonic foraminifera of mixed species from seven samples were selected for radiocarbon analysis at the National Ocean Sciences Accelerator Mass Spectrometer (NOSAMS) laboratory at the Woods Hole Oceanographic Institution (WHOI) (McNichol et al., 1995).

Radiocarbon ages were calibrated to ages in yr BP using CALIB 6.0 (Stuvier and Reimer, 1993) and the Marine09 calibration curve (Reimer et al., 2009). Marine reservoir corrections were applied to the calibration curve using the standard marine reservoir correction of 400 years, which is close to the average of the two nearest reservoir corrections in the Bay of Bengal (Dutta et al., 2001; Southon et al., 2002).

A total of 68 samples of benthic foraminifer *Uvigerina peregrina* in the upper 27 m of Site 19B were measured for $\delta^{18}O$ and $\delta^{13}C$ using a Finnigan MAT253 mass spectrometer at the Micropaleontology Mass Spectrometer facility at WHOI. *Uvigerina peregrina* $\delta^{18}O$ measurements were used with the established orbital chronostratigraphy (Imbrie et al., 1984; Martinson et al., 1987) to extend the age model beyond the range of radiocarbon calibration.

Sedimentary carbon and nitrogen were measured on 95 samples from the upper 12 m of Site 19B using a Perkin Elmer CHN 2400 Series II CHNS/O Analyzer at the University of New Hampshire (UNH) and the methods described in Phillips et al. (2011) for carbonate-bearing marine sediments. Approximately 1 g of each sample was crushed and dried with 20 mg of sediment used for each analysis. One split was measured for total carbon (TC) and total nitrogen (TN), while the other was treated with sulfurous acid to remove inorganic carbon for total organic carbon (TOC) measurements, with the difference (TC-TOC) used to calculate inorganic carbon (IC). Calcium carbonate ($CaCO_3$) was calculated using the molecular mass ratio of $CaCO_3$ and IC as $CaCO_3 = IC \times 8.33$. C/N ratios were calculated using the atomic mass weighted ratio of TOC and TN as C/N = (TOC/12.011)/(TN/14.007). Bulk $\delta^{13}C$ and $\delta^{15}N$ of the organic carbon in samples were measured using elemental analysis-isotope ratio-mass spectrometry (EA-IR-MS) on a Delta Plus XP Mass Spectrometer interfaced with a Costech 4010 Elemental Analyzer at UNH. Samples of approximately 30 mg were prepared for isotopic analysis using the same preparation method as the TOC measurements. Duplicate samples were run every 10 samples. Uncertainty in TC, TOC, TN, C/N, and $CaCO_3$ measurements are 0.04, 0.02, <0.01, 0.63, and 0.44 wt. % respectively, represented by the average of error in duplicate samples (2 standard deviations). Reproducibility in $\delta^{13}C$ and $\delta^{15}N$ are 0.1 and 0.18 ‰ respectively.

XRF core scanning was performed using a Cox Analytical ITRAX XRF core scanner at WHOI at a resolution of 4 mm. Details of this method and analytical capabilities are described in Croudace et al. (2006).

The grain size distribution of samples from the upper 12 m of Site 19B was measured at UNH using a Malvern Mastersizer 2000 laser-diffractometer particle size analyzer with Hydro-G dispersion unit, calibrated with glass bead standards ranging from medium silt to fine sand. Approximately 0.5 mL of sediment was suspended in a solution of 20 mL of 5.4 g/L sodium hexametaphosphate, agitated, left overnight, and re-agitated before analysis (Sperazza et al., 2004). The sample was introduced to the water dispersant at an obscuration rate between 15 and 20% and subjected to 60 seconds of sonication to prevent flocculation. Bulk samples were measured to include all lithogenic, biogenic, and authigenic components of the sample. A split of each sample was treated with 15 mL of 30% H_2O_2 and 20 mL of 10% HCl at room temperature to measure the particle size distribution of the carbonate- and TOC-free fraction. I present the grain-size distribution as median grain size (d(0.5)), 90th percentile grain size (d(0.9)), 10th percentile grain size (d(0.1)), as well as the clay, silt, and sand percentages, according to the scale of Wentworth (1922). Two samples representing the range of $CaCO_3$ and BSi in this record were treated in consecutive application of 10% HCl, 30% H_2O_2, and 0.1 M

NaOH (85 °C) to observe the effects of carbonate, organic matter and biosiliceous material on the grain size distribution.

Relative to the sieve-pipette method, grain-size distributions measured by laser diffraction generally underestimate the clay-size fraction (e.g. Beuselinck et al., 1998; Eshel et al., 2004; Konert and Vadenberghe, 1997; Kowalenko and Babuin, 2013; Loizeau et al., 1994; McCave et al., 1996); however, laser diffraction methods allow for high-resolution measurements of grain-size distributions at high precision (Roberson and Weltje, 2014; Sperazza et al., 2004). Konert and Vandenberghe (1997) and Ramaswamay and Rao (2006) suggest that 8 µm or 6.2 µm respectively are more accurate boundaries between silt and clay when using laser diffraction methods. Applying this modified upper clay limit to our analyses suggests the clay fraction in our samples may be underestimated by 14 to 23% on average. In this study, the laser diffraction technique is sufficiently accurate for the purpose of identifying down core relative variation in major grain-size classes and median grain size, and the comparison of these records to other proxies. For bulk samples, average reproducibility (two standard deviations) for d(0.1), d(0.5), and d(0.9) are within 0.4, 1.1, and 180 µm respectively. Reproducibility of the clay, silt, and sand fractions in bulk samples are 3.5, 4.4, and 5.6 % respectively. For treated samples, average reproducibility (two standard deviations) for d(0.1), d(0.5), and d(0.9) are within 0.1, 0.3, and 3.6 µm respectively. Reproducibility of the clay, silt, and sand fractions in treated samples are 1.2, 2.4, and 2.4 % respectively.

Samples were measured for bulk mineralogy using powder X-ray diffraction (XRD) at a resolution of approximately every 0.5 m of the upper 12 m. Approximately 0.5 g of dried and crushed sediment was analyzed using an InXitu Terra X-ray diffractometer at the U.S. Department of Energy-National Energy Technology Laboratory in Albany, OR. The sample was exposed to Cobalt K-alpha radiation in a vertical sample holder with Mylar© windows, and the diffraction pattern was measured by a 2D Pelier-cooled CCD detector with a two theta (2θ) range from 5° to 55°. Mineral identification was performed using MDI Jade 9 software, and semi-quantitative mineral weight percent was estimated by the pattern simulation function in Jade, utilizing a matrix-flushing method (Chung, 1974). Due to overlapping peak response for minerals such as kaolinite and chlorite, and plagioclase and K-feldspar, total clay and total feldspars are reported rather than individual mineral phases. For this analysis, four bulk mineralogical components are reported as percent relative abundance of quartz, feldspar, calcite, and total clays.

Approximately 25 mg of dried sediment was subjected to leaching of BSi using a wet alkaline method (e.g. DeMaster, 1981; Mortlock and Froelich, 1989), followed by measurement of leached silica on a Spectronic 601 UV-Vis spectrophotometer (Strickland and Parsons, 1972). Leaching at 85°C over five hours with sub-samples collected at each hour, allowed for the accurate determination of biogenic silica by accounting for leaching of silicate minerals, as described in Cawthern et al. (2014). Average reproducibility of BSi (2 standard deviations of replicate samples) is 0.08 wt. %.

An age model for Site 19 was calculated using calibrated radiocarbon ages and oxygen isotope events from the benthic *Uvigerina peregrina* $\delta^{18}O$ record. Sedimentation rates (SR) were calculated by interpolation between age control points. Sediment mass accumulation rates (MAR) in g cm^{-2} kyr^{-1} were calculated by the product of the shipboard dry-bulk density data (DBD) in g cm^{-3} (Collett et al., 2008) and SR in cm kyr^{-1}. During NGHP-01, DBD was measured using moisture and density analysis (MAD) at a resolution of approximately 1 m. To ensure that MAR incorporated down core variation in DBD, the linear regression between MAD bulk density and DBD, as well as MAD bulk density and bulk density derived from gamma ray attenuation from shipboard multi-sensor core logger (MSCL) measurements were calculated. MSCL density (measured at a 2.5 cm resolution) and its two-step linear relationship to DBD, was used to estimate variation in DBD with depth at a higher resolution.

MAR for specific components (e.g., TOC, $CaCO_3$) was calculated by the product of MAR and the weight percent of each component. Terrigenous MAR was calculated by subtracting the biogenic component MAR (sum of $CaCO_3$, TOC, TN, BSi) from the bulk MAR (e.g. Gardner et al., 1997).

RESULTS

Age Constraints

Six calibrated radiocarbon measurements, with ages between 1.4 and 31.3 ka establish age control for the upper 4 m at Site 19A/B. One radiocarbon measurement from 8.15 mbsf was beyond the radiocarbon calibration scale (48,000 radiocarbon years) and not used in the age model. Table 1-1 contains radiocarbon sample and calibration data. In addition, $\delta^{18}O$ of *Uvigerina peregrina* foraminifers established a chronostratigraphy indicating a complete record extending to oxygen isotope stage (OIS) 5.4 (111 ka) at 11.5 mbsf. Below this depth, the $\delta^{18}O$ record was difficult to match to established oxygen isotope chronostratigraphies, due to possible unconformities and overprinting of the benthic foraminifers. Six isotope events were identified in the $\delta^{18}O$ pattern between and 18 and 111 ka (Table 1-2). In total, 12 age control points provided an age-depth model for the 12 m record (Fig. 1-2). An ash layer observed at 8.42 to 8.46 m is at approximately 71 ka according to our age model. The presence of this ash layer is at the same time interval 73 ± 4 ka as that determined for the Toba eruption (Chesner et al., 1991; Westgate et al., 1998).

Physical Properties, Grain Size, and Mineralogy

Volume-dependent magnetic susceptibility (κ) measured shipboard during NGHP01 is generally low (< 40 μSI) with a pronounced increase (40 to 84 μSI) between 33 and 15 ka (Fig. 1-3). κ is variable (20 and 60 μSI) between 80 and 33 ka, and is low (< 40 μSI) in the Holocene and between 100 and 80 ka, with a small increase to 50 μSI at 105 ka. Mass-dependent magnetic susceptibility was calculated from the volume-dependent κ using density and then adjusted for the carbonate-free fraction (χ_{nc}) (e.g. Lean and McCave, 1998) to account for variation in the κ record driven by dilution by $CaCO_3$. The χ_{nc} pattern did not differ considerably from κ, other than a slight increase in χ_{nc} relative to κ between 26 and 18 ka. Shipboard bulk density measurements show muted variation similar to κ and χ_{nc}, with a decrease in the Holocene and little variation 100 to 80 ka. There is an anomalous decrease in bulk density between 65 and 62 ka.

Table 1-1. Radiocarbon analyses by accelerator mass spectrometry (AMS). Calendar year calibrations were made using CALIB ver. 6.0 (Stuvier and Reimer, 1994).

Depth (mbsf)	Core-Section	Site-Hole	Interval depth (cm)	Radiocarbon age (radiocarbon kyr BP•)	Radiocarbon age error (radiocarbon kyr BP•)	Calibrated age (ka) lower 2σ	Calibrated age (ka) upper 2σ	Mean calibrated age (ka)	Source
0.01	1H-1	19-B	0-2	1.85	0.04	1.30	1.49	1.40	This study
1.945	1H-2	19-B	44-45	9.69	0.04	10.47	10.64	10.56	Schulenberg, 2011
2.585	1H-2	19-B	108-109	11.05	0.05	12.36	12.71	12.54	Schulenberg, 2011
3.248*	1H-3	19-A	23.8-25.8	16.65	0.08	19.21	19.58	19.40	This study
3.545	1H-3	19-B	54-55	22.90	0.08	26.73	27.74	27.24	Schulenberg, 2011
3.958*	1H-3	19-A	94.8-96.8	27.60	0.12	31.11	31.48	31.29	This study
6.188*	2H-1	19-A	87.8-89.8	48	0.65	out of range	out of range	out of range	This study

•Before present, where present is 1950 A.D.

*The original depth of the samples in hole A were adjusted by additon of 3.8 cm to match the record of hole B by correlation of magnetic susceptibility records.

XRD measurements of bulk sediment samples reveal a range in relative abundance among four components: total clay (34-66%), quartz (21-37%), calcite (0-29%), and feldspar (0-13%) (Fig. 1-3). Total clay increases from 27 to 10 ka, and decreases between 77 and 27 ka. Calcite follows an inverse pattern to clay, increasing from 77 to 30 ka, and then decreasing since 30 ka. Quartz increases from 20 to 35% since 18 ka, and there are small increases in quartz at 26, 56, 61, and 103 ka. Feldspar remains below 13% throughout the record. These ranges agree with the overall trends at Site 19 reported by Phillips et al. (2014). Quartz and feldspar exhibit little variation over the record compared to total clay and calcite.

Table 1-2. Oxygen isotope events from δ^{18}O of benthic foraminifers.

Depth (mbsf)	Core-Section	Site-Hole	Interval depth (cm)	Foraminifera species	Oxygen isotope event	Age (ka)
3.105	1H-3	19-B	104-106	*Uvigerina peregrina*	2.2	18
6.105	1H-5	19-B	10-11	*Uvigerina peregrina*	3.3	50.2
8.205	2H-1	19-B	90-91	*Uvigerina peregrina*	4.22	64.1
10.005	2H-2	19-B	120-121	*Uvigerina peregrina*	5.1	79
10.505	2H-3	19-B	20-21	*Uvigerina peregrina*	5.3	99.4
11.505	2H-3	19-B	120-121	*Uvigerina peregrina*	5.4	110.8

Comparison of bulk sediment, $CaCO_3$-free sediment (HCl-treated), $CaCO_3$ and TOC-free sediment (HCl and H_2O_2-treated), and $CaCO_3$, TOC and BSi-free sediment (HCl, H_2O_2, and NaOH-treated) in two samples show a strong influence of carbonate on the grain size distribution (Fig. 1-4). These samples only show minor changes to the grain size distribution with TOC and BSi removal, suggesting that the record of grain size distribution in HCl and H_2O_2-treated samples represents primarily the lithogenic fraction.

The bulk grain size distribution is predominately silt (43-71%) with a median grain size (d(0.5)) ranging from 4 to 14 μm (Fig. 1-5). The clay size fraction comprises 17 to 42% of the distribution with the 10th percentile of the grain-size distribution (d(0.1)) ranging from 0.2 to 2.7 μm. The sand-sized fraction ranges from 0.4 to 31% with the 90th percentile (d(0.9)) ranging from 17 to 915 μm. Bulk grain size exhibits a pronounced increase in sand-sized content, d(0.5), and d(0.9) between 65 and 10 ka and d(0.5) correlates closely with the XRF Zr/Rb mean grain size proxy. Grain size distribution in samples treated to remove carbonate and organic matter from the sample exhibited largely different down-core variation compared to the bulk sample (Fig. 1-6), suggesting biogenic components strongly influence the overall grain size distribution (Fig. 1-7). The bulk grain size distribution with secondary peaks at around 0.1 μm and 100-1000 μm is consistent with similar measurements of hemipelagic sediments containing nannofossils and foraminfers (Trentesaux et al., 2001). The carbonate-free, predominantly lithogenic-only grain size distribution is 56 to 86% silt with d(0.5) ranging from 5.2 to 14.1 μm (all but two samples were below 10 μm). Clay comprises 11 to 37% with d(0.1) varying from 1.8 to 2.4 μm. Lithogenic sand-sized content (0-6%) and d(0.9) (16-38 μm) are much lower than in the bulk sample. Treated lithogenic grain size shows little variation in d(0.5) or d (0.9) with a minor increase between 79 and 56 ka. Median grain size does not vary with lithogenic d(0.5) as in the bulk sample. At 12 ka, the lithogenic clay and sand-sized fraction increase abruptly and then decrease through the remainder of the Holocene.

<u>Biogenic Components</u>

TOC contents at Site 19 range from 0.89 wt. % to 1.96 wt. % with a mean of 1.39 wt. % (Fig. 1-8). TOC increases to greater 1.5 wt. % between 12-14, 29-53, and 63-65 ka. TOC is lower than 1.0 wt. % at 16, 56, 59, and 68-70 ka. There is little variation in TOC between 10 ka and present and 110-72 ka. Bromine measured by XRF is plotted with TOC as a marine organic matter proxy (McHugh et al., 2008; Ziegler et al., 2008), and there is a general agreement between TOC and Br, except since 10 ka, when there is divergence between the two records. TN co-varies with TOC with small differences apparent in the TOC/TN ratio (Fig. 1-8). TOC/TN varies primarily between 10 to 12 between 110 and 80 ka. Between 80 and 60 ka, variation in TOC/TN increases from 9 to 13, and then TOC/TN increases from 10 to 13 between 60 and 30 ka. Since 30 ka, TOC/TN decreases to 9.

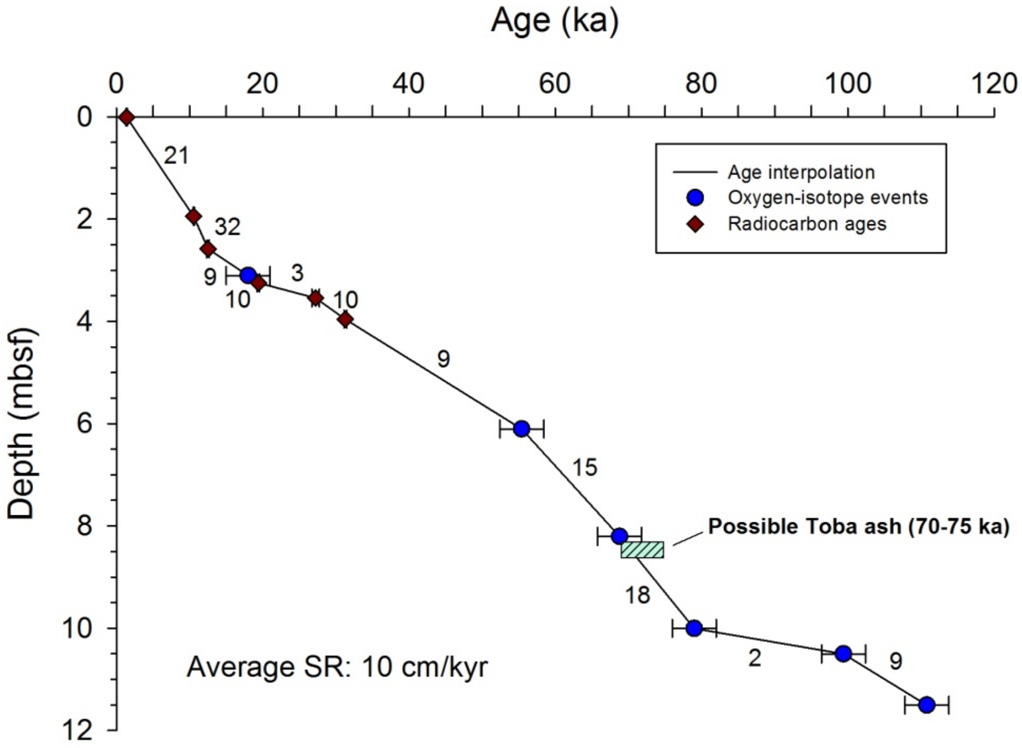

Figure 1-2. Plot of depth versus age from radiocarbon ages and oxygen isotope events. Sedimentation rates (SR) from linear interpolation are listed for each interval in cm/kyr. Error from calibrated radiocarbon ages is smaller than symbol size, and estimated method error of 3500 years (Martinson et al., 1987) is plotted for oxygen isotope events. Overall SR is 10 cm/kyr, with a notable increase in SR during the Holocene. An ash at Site 19 at 8.4 m depth is at 71 kyr, and likely originated from the Toba eruption (Chesner et al., 1991; Westgate et al., 1998).

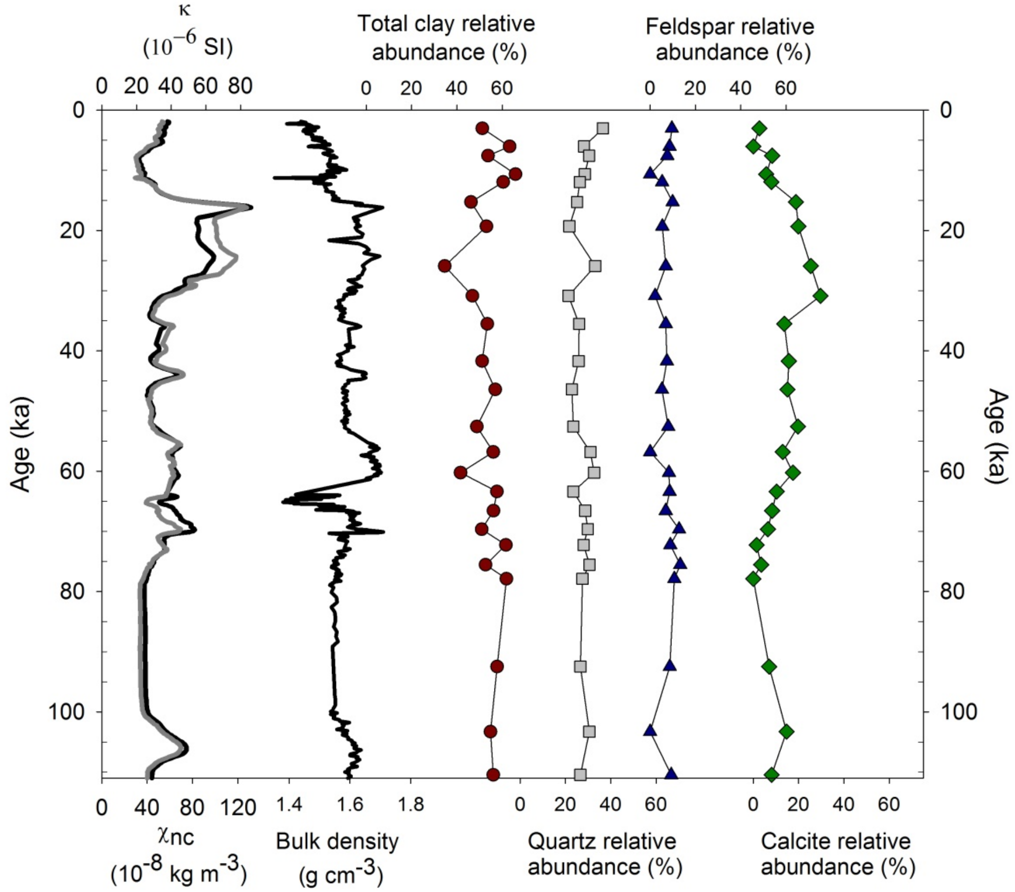

Figure 1-3. Down-core variation in volume-dependent magnetic susceptibility (κ), mass-dependent magnetic susceptibility adjusted for the carbonate-free fraction (χ_{nc}), bulk density, and the relative abundance of four mineral components (total clay, quartz, feldspar, and calcite) from X-ray diffraction (XRD). κ, χ_{nc}, and calcite increase between 10 and 70 ka, and at 105 ka.

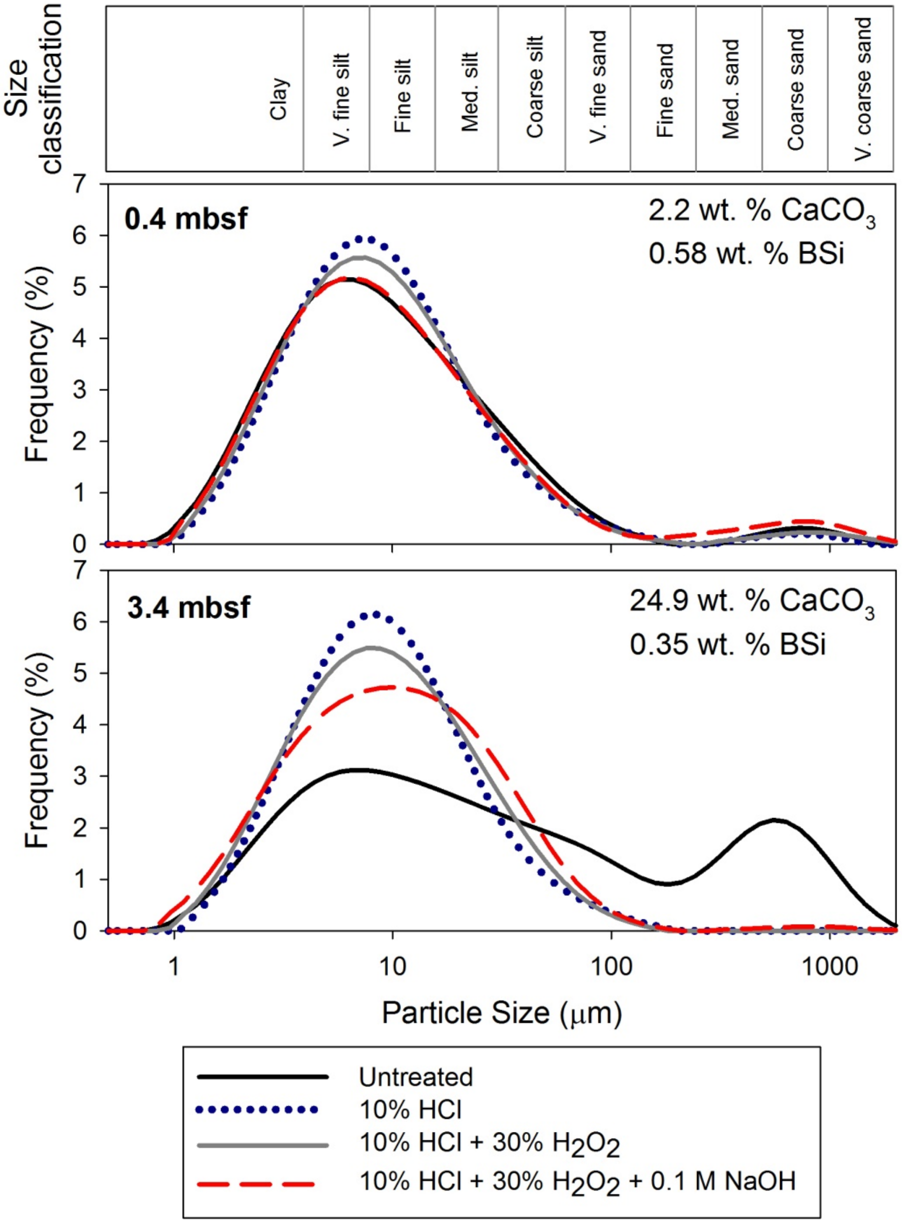

Figure 1-4. Comparison of bulk particle size distributions in bulk sediment, HCl-treated sediment ($CaCO_3$-free), HCl and H_2O_2-treated sediment ($CaCO_3$- and TOC-free), and HCl, H_2O_2, and NaOH-treated sediment (carbonate-, TOC-, and BSi-free). The upper panel represents a sample with a minimum in $CaCO_3$ and maximum in BSi, and the lower panel represents a sample with a maximum in $CaCO_3$ and minimum in BSi.

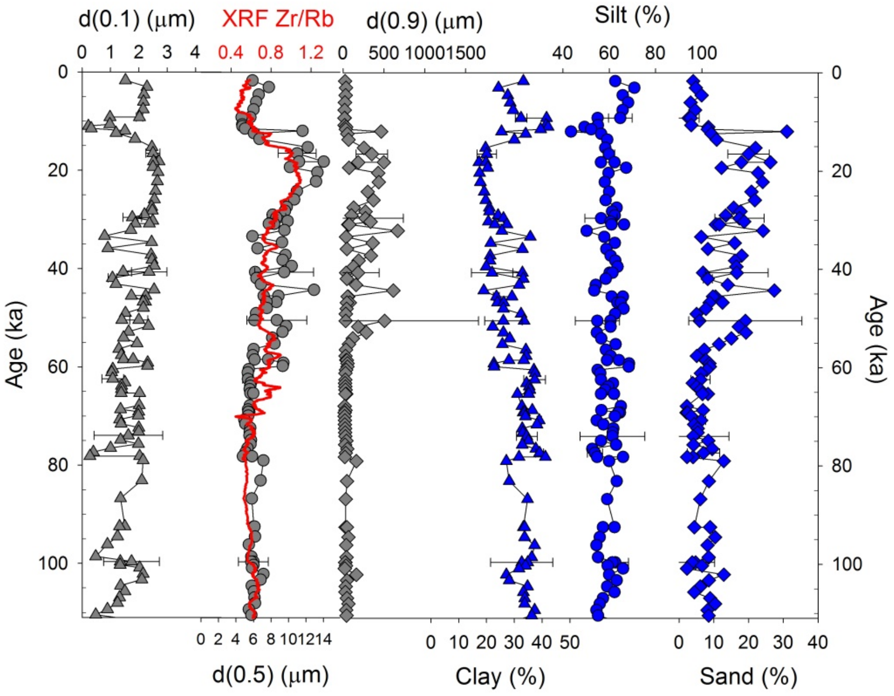

Fig. 1-5. Down-core variation in bulk untreated grain size as shown by the 10th, 50th, and 90th percentiles, d(0.1), d(0.5), and d(0.9) respectively, of the grain size distribution, and the clay, silt, and sand percentages. The Zr/Rb ratio from X-ray fluorescence (XRF) is shown with the median grain size as a high-resolution grain size proxy (Dypvik and Harris, 2001). Median grain size and sand-sized content (foraminifers) increase between 10 and 70 ka.

IC, presented as CaCO$_3$, varies little (between 2-4 wt. %) between 99 and 72 ka, after an increase to 7 wt. % at 102-103 ka (Fig. 1-8). CaCO$_3$ increases considerably between 71 and 10 ka, increasing from 4 to 24 wt.% between 71 and 24 ka, then decreasing to 3 wt. % by 10 ka. Superimposed on the long-term trend, there is short-term variation on the order of the sampling interval (~1200 yr) to 7 kyr, between 71 and 10 ka. Since 10 ka CaCO$_3$ varies between 2-4 wt. %, similar to the interval before 71 ka. Calcium from XRF is plotted with CaCO$_3$, and the two records match closely. Relative to CaCO$_3$, BSi is low (0.27 to 0.63 wt. %) (Fig. 1-8). Between 110 and 69 ka, BSi varies primarily between 0.4-0.55 wt. %, then decreases to 0.3 and 0.4 wt.% between 68 and 19 ka. BSi increases since 17 ka, reaching greater than 0.55 wt. % since 9 ka.

Isotopic Measurements

δ^{13}C of bulk organic matter (δ^{13}TOC) varies between -20 and -16 ‰ VPDB at Site 19 (Fig. 1-9). There is an increase from -18 to -16 ‰ at 104-106 ka, before a long-term increase from -19 to -17 ‰ from 92 ka to 16 ka. δ^{13}TOC decreases to -21 between 15 ka and 9 ka, and remains between -21 and -20 since 9 ka. δ^{15}TN varies between 3 and 5.7 ‰ air. Overall there is a slight increasing trend of δ^{15}TN (4-5.7 ‰ air) between 83 and 12 ka, punctuated by an interval of decreased δ^{15}TN (3.2-4.4 ‰). After 12 ka, δ^{15}TN decreases to 4-5 ‰.

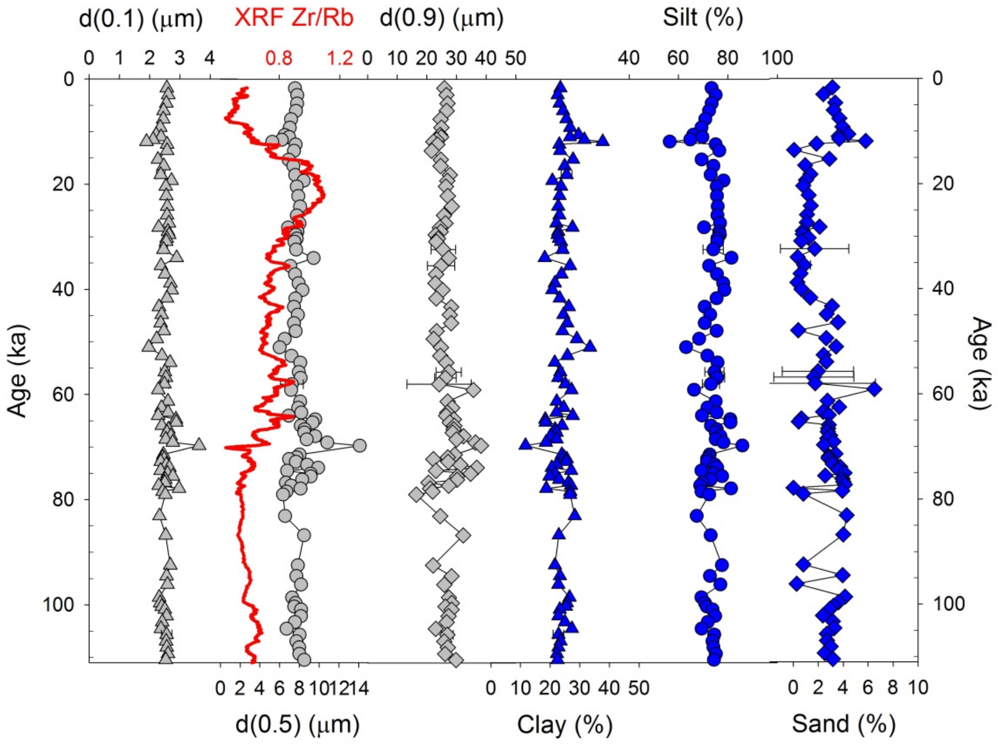

Fig. 1-6. Down-core variation in HCl- and H_2O_2- treated grain size as shown by the 10th, 50th, and 90th percentiles, d(0.1), d(0.5), and d(0.9) respectively, of the grain size distribution, and the clay, silt, and sand percentages. The Zr/Rb ratio from X-ray fluorescence (XRF) is shown with the median grain size as a high-resolution grain size proxy (Dypvik and Harris, 2001). Median grain size and sand-sized content (foraminifers) increase between 10 and 70 ka.

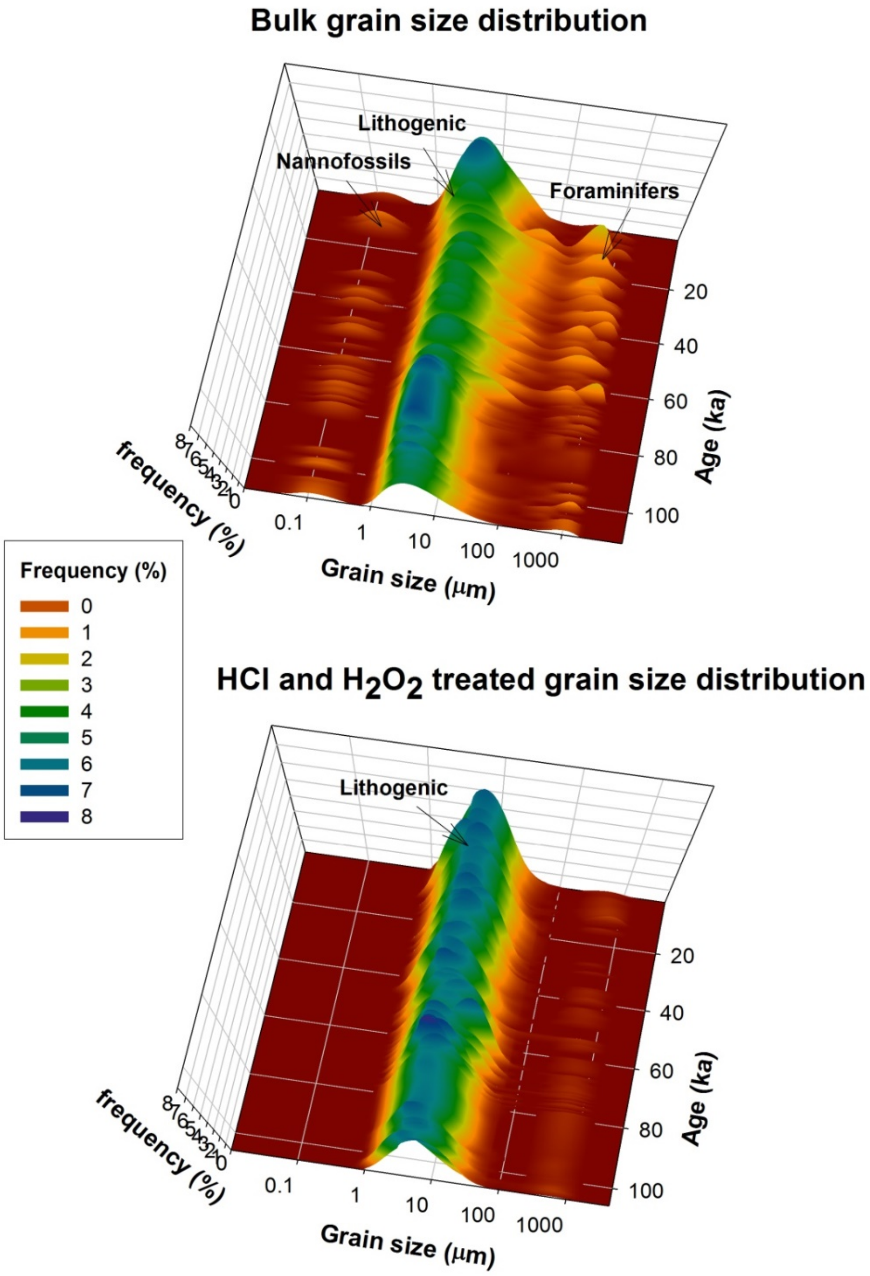

Fig. 1-7. Grain size distributions of bulk samples (top) and samples treated to remove biogenic material (bottom). Horizontal axes are grain size bins from 0.01 to 2000 µm and age in ka. Vertical axis is the percentage of the total distribution. Both bulk and treated samples show a main peak of lithogenic material spanning 1 to100 µm, primarily within the clay to fine-silt range. The bulk sample shows additional peaks at 0.1 and 50 to 1000 µm corresponding to nannofossil and foraminifers.

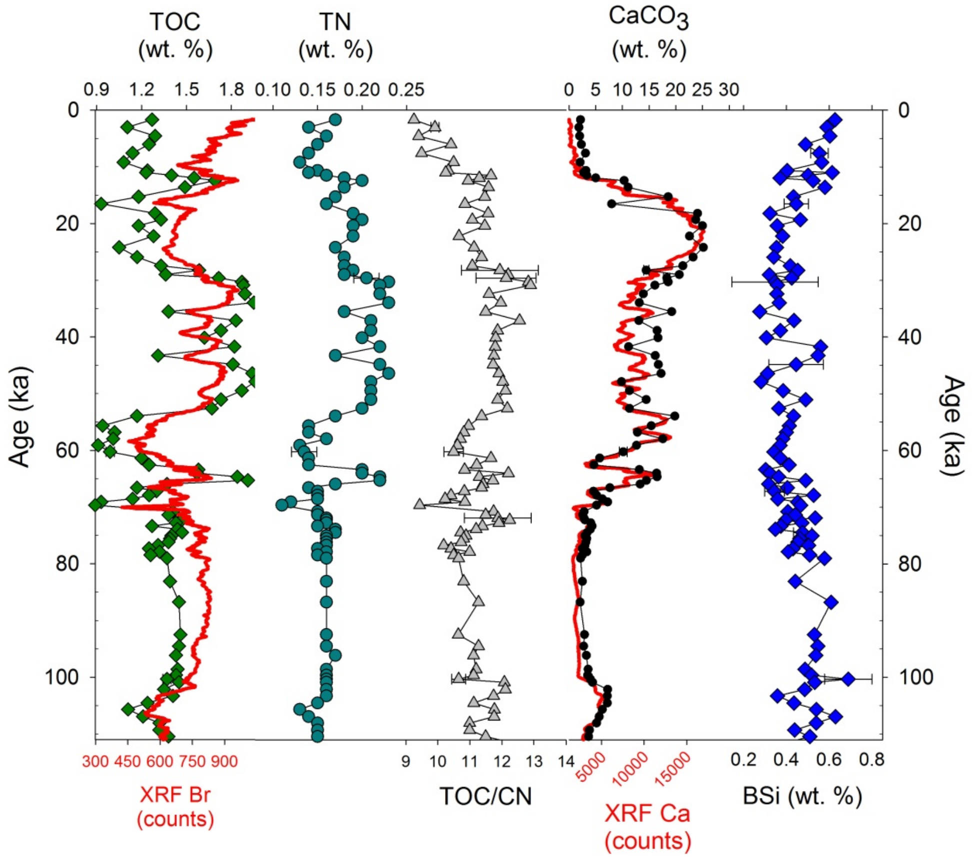

Fig. 1-8. Down-core variation in biogenic components: total organic carbon (TOC), total nitrogen (TN), TOC/TN ratios, $CaCO_3$ calculated from inorganic carbon content, and biogenic silica (BSi). Bromine is plotted with TOC as a marine organic matter proxy and calcium plotted with $CaCO_3$. $CaCO_3$ increases to 5-25 wt% between 10 and 70 ka. TOC/TN decreases since 20 ka, while BSi increases over the same period. TOC content is high (greater than 1.5 wt. %) at 18 ka, between 30 and 50 ka, and at 65 ka.

$\delta^{18}O$ of benthic foraminifer *Uvigerina peregrina* follows a pattern matching global stacked benthic oxygen isotope records (Imbrie et al., 1984; Lisiecki and Raymo, 2005; Martinson et al., 1987) and was used to develop the age model, with tie points corresponding to oxygen-isotope events from the SPECMAP record. There is some deviation in absolute variation between the globally-stacked record and Site 19; however, local maxima and minima in the record match well between records. *Uvigerina peregrina* $\delta^{13}C$ follows a pattern inverse to $\delta^{15}TN$, varying between -0.2 and -0.9 ‰ VPDB, with an increase in $\delta^{13}C$ since 12 ka.

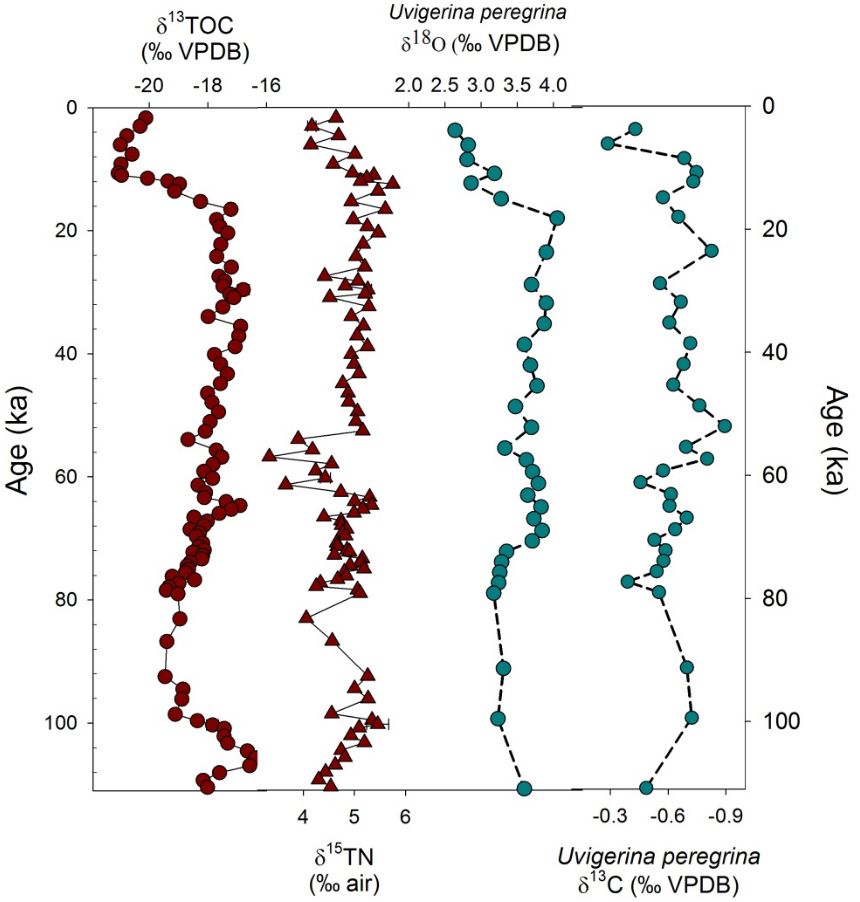

Fig. 1-9. Down-core variation in isotopic variation bulk organic matter and benthic (*Uvigerina peregrina*) foraminifers. δ^{18}O and δ^{13}TOC generally match sea level variation with an anomaly in δ^{13}TOC at 105 ka. δ^{15}TN generally matches the pattern in δ^{13}TOC with a negative anomaly at 55-60 ka.

Mass accumulation Rates

Sedimentation rate (SR), calculated by linear interpretation between twelve ages varied from 2 to 32 cm/kyr with an average of 10 cm/kyr (Fig. 1-2). Between 110 and 25 ka, SR varies between 2 and 17 cm/kyr (Fig. 1-10). Since 25 ka, there is a large increase in SR from the LGM (3-9 cm/kyr) to the early Holocene (32 cm/kyr between 11 and 12 ka), and SR remained high (21 cm/kyr) since 11 ka. Bulk MAR varies between 1 and 27 g/cm^3/kyr, with minor variation from the SR pattern due to dry bulk density variation.

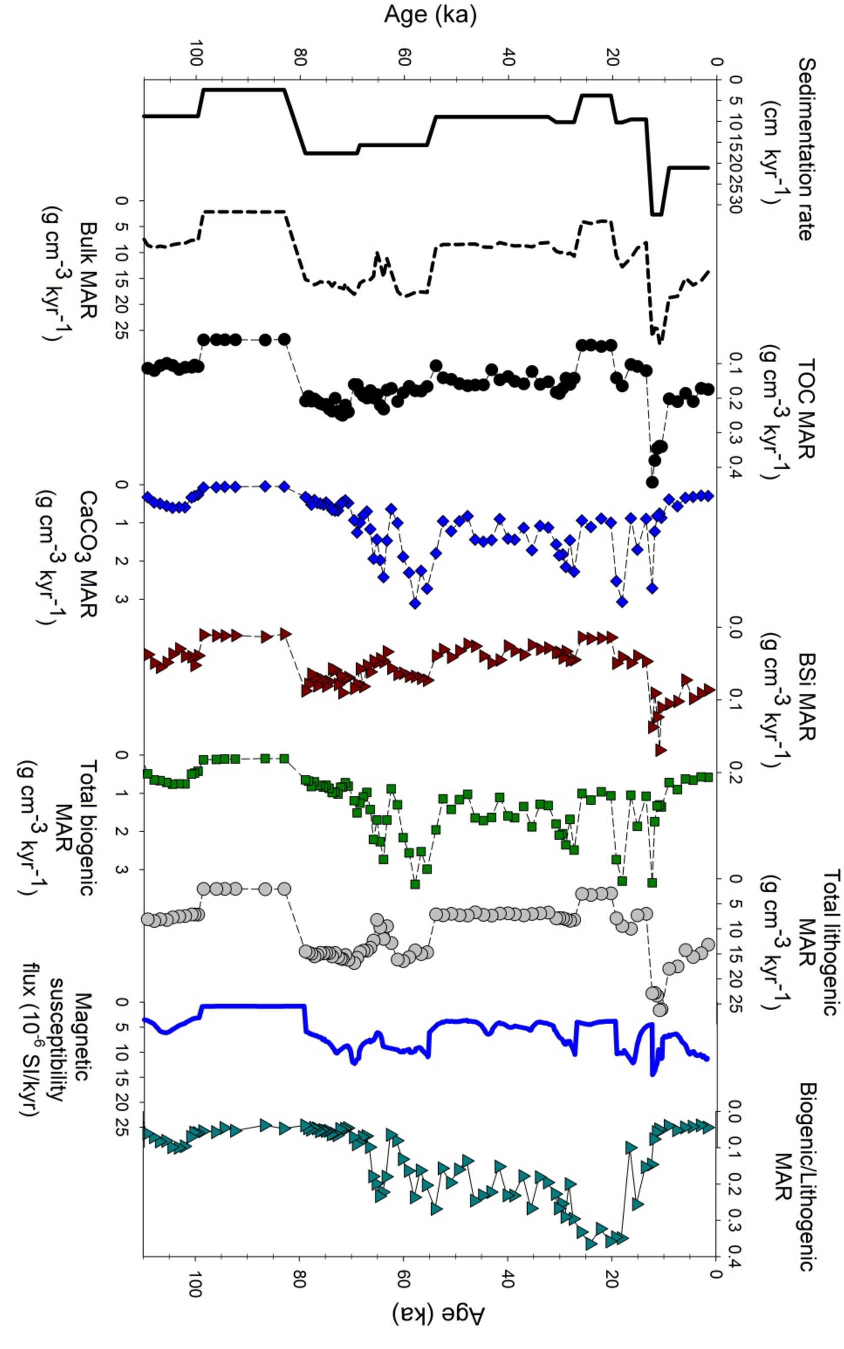

Fig. 1-10. Down-core variation in SR and mass accumulation rates (MAR) in g/cm^3/kyr. Bulk MAR is partitioned into TOC, CaCO$_3$, BSi, total lithogenic, and total biogenic MAR. χ_{nc} flux represents the flux of magnetic material per kyr. SR is the primary control on MAR, except for the biogenic components, where CaCO$_3$ shows a large increase between 10 and 70 ka, and BSi shows a small increase since 12 ka.

MAR of TOC varies from 0.03 to 0.44 g/cm^3/kyr, largely following the trend in bulk MAR, with a slight relative increase between 53 and 29 ka due to high TOC content. BSi MAR ranges from 0.01 to 0.16 g/cm^3/kyr, also mirroring bulk MAR between 110 and 10 ka, but with a relative increase since 10 ka. $CaCO_3$ MAR shows two distinct modes of variation. Between 110 and 71 ka, and after 10 ka, $CaCO_3$ MAR ranges between 0.01 and 0.6 g/cm^3/kyr with little variation (Fig. 1-10). Between 70 and 10 ka, $CaCO_3$ ranges from 0.7 to 3.1 g/cm^3/kyr with cyclic variation ranging from 3 to 7 kyr.

Biogenic MAR (sum of $CaCO_3$, TOC, TN, and BSi) is dominated by the influence of $CaCO_3$, with the same two modes of variation. Biogenic MAR ranges between 0.05 and 0.6 g/cm^3/kyr between 110 and 71 ka and after 10 ka (Fig. 1-10) Biogenic MAR is enhanced between 70 and 10 ka, with higher-frequency variation between 0.8 and 3.4 g/cm^3/kyr. Lithogenic MAR (bulk MAR – biogenic MAR) varies between 0.03 and 26 g/cm^3/kyr. The ratio of biogenic MAR to lithogenic MAR varies between 0.04 and 0.36 (Fig. 10) and closely matches the pattern in $CaCO_3$ content (Fig. 1-8), explaining $CaCO_3$ content as a balance of production of $CaCO_3$ and dilution by lithogenic components.

DISCUSSION

Increased Marine Productivity, 70-10 ka

$CaCO_3$ measured at Site 19 correlates with observations of nannofossils and foraminifers in smear slide and coarse fractions observed during NGHP-01 (Collett et al., 2008). Because authigenic carbonate content is negligible and detrital carbonates were not observed, $CaCO_3$ MAR predominantly represents biological production of calcareous marine organisms in the surface waters of the Bay of Bengal. In general, blooms of coccolithophorids and foraminifers last on the order of several weeks (e.g. Bijma et al., 1990; Holligan et al., 1993) and EICC flows at velocities at up to 20 cm/s (McCreary et al., 1996). Based on these estimates, biogenic $CaCO_3$ accumulated at the Mahanadi Basin may have originated from up to several hundred km up-current, a region spanning the Indian margin from offshore the Ganges-Brahmaputra Rivers to the Krishna-Godavari Basin, depending on season. The water depth of 1422 m at Site 19 is shallow enough to be well above the lysocline in the Indian Ocean (Banakar et al., 1998; Bassinot et al., 1994). Carbonate dissolution has been observed above the lysocline in the Indian Ocean associated with decomposition of organic matter (Peterson and Prell, 1985; Schulte and Bard, 2003); however, variation in $CaCO_3$ at Site 19 is much larger than the supralysoclinal dissolution events observed in the Indian Ocean and there is little correlation between TOC and $CaCO_3$ (Fig. 8). $CaCO_3$ MAR accounts for SR-driven dilution by lithogenic material, making $CaCO_3$ MAR a measure of $CaCO_3$ production rather than a lack of dilution by terrigenous material (e.g. Babu et al., 2010).

Enhanced $CaCO_3$ MAR (productivity) between 10 and 70 ka at Site 19 correlates to a period of elevated cation content in the GISP2 ice core on the Greenland Ice Sheet (Mayewski et al., 1997) (Fig. 1-11). Dust in Greenland ice cores has an East Asian provenance during the Late Pleistocene (Biscaye et al., 1997; Svensson et al., 2000), likely driven by changes in wind intensity in the source region (Fuhrer et al., 1999). During glacial conditions, South Asia was drier due to a weaker southwest monsoon and strengthened winter monsoon between 75 and 15 ka (Prell and Kutzbach, 1987), which is in agreement with global dust fluxes compared between glacial and interglacial conditions (e.g. Maher et al., 2010; Mahowald et al., 1999; Lambert et al., 2008; Werner et al., 2002)

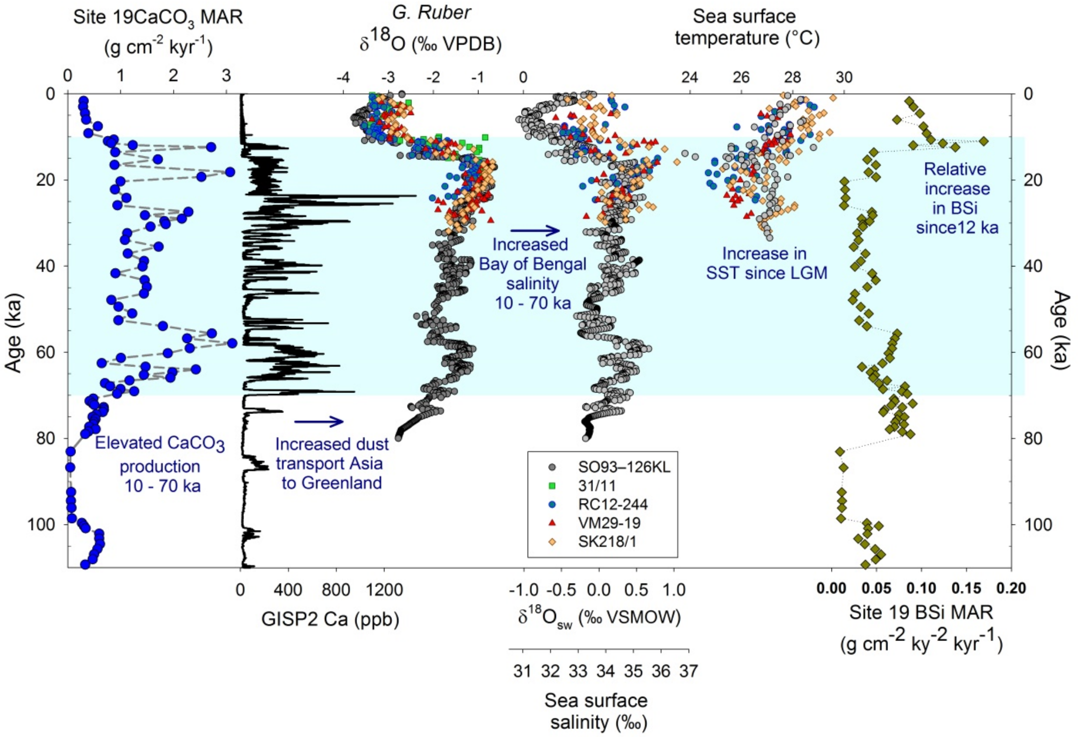

Fig. 1-11. Comparison of CaCO$_3$ MAR at Site 19 to calcium in the GISP2 ice core on the Greenland ice sheet (dust proxy, Mayewski et al., 1997 with dust shown to be Asian in origin by Biscaye et al., 1997), δ^{18}O of *Globigerinoides ruber* at 126KL, 31/11, RC12-344, SK218/1 and VM29-19 (Chauhan, 2003; Govil and Naidu, 2011; Kudrass et al., 2001; Rashid et al., 2007, 2011), sea-surface salinity (SSS) at 126KL and SK218/1 (Govil and Naidu, 2011; Kudrass et al., 2001), δ^{18}O$_{sw}$ at RC12-344 and VM29-19 (Rashid et al., 2007, 2011), sea-surface temperature (SST) at 126KL, RC12-344, SK218/1 and VM29-19 (Govil and Naidu, 2011; Kudrass et al., 2001; Rashid et al., 2007, 2011) . CaCO$_3$ production increased during a time of increased aridity in the Indian region and increased salinity in the Bay of Bengal and Andaman Sea. Bsi MAR is approximately an order of magnitude less than CaCO$_3$ and shows a relative increase during the last 12 kyr compared to the glacial low-stand.

It is unlikely that dust deposition directly stimulated productivity in the Bay of Bengal. Enhanced dust fluxes during glacial conditions, have been suggested to stimulate productivity through iron fertilization in high-nutrient, low-chlorophyll regions (Maher et al., 2010; Martínez-García et al., 2014; Wolff et al., 2006); however, the Bay of Bengal is not considered to be limited by iron (Wiggert et al., 2006). It is more plausible that changes in Asian aridity that increased dust fluxes also increased sea surface salinity (SSS) and reduced stratification in the Bay of Bengal, thus allowing for increased mixing and productivity.

A direct result of a weakened southwest monsoon is increased salinity in the surface waters of the Bay of Bengal. Multiple studies across the northeast Indian Ocean have characterized $\delta^{18}O$ of seawater ($\delta^{18}O_{sw}$) as a paleo-salinity indicator between the Last Glacial Maximum (LGM) and present, using paired measurements of *Globigerinoides ruber (white)* $\delta^{18}O$ and paleo-sea surface temperature (SST) proxies using Mg/Ca or alkenone $U^{K}{}_{37}$ (Govil and Naidu, 2011; Kudrass et al., 2001; Rashid et al., 2007, 2011). These records indicate a general freshening of the Bay of Bengal from the LGM to the Holocene as shown by a negative trend in $\delta^{18}O$ of seawater ($\delta^{18}O_{sw}$) (Fig. 1-11). Cullen et al. (1981) show a similar trend of decreasing salinity since the LGM using relative abundance of low-salinity tolerant planktonic foraminifer species. Although these records show differences in $\delta^{18}O_{sw}$ and SST trends on sub-orbital timescales such as during the Bølling-Allerød and Younger Dryas, and along latitude gradients, these records show a general agreement in $\delta^{18}O_{sw}$ and SST trends between the LGM and Holocene, indicating a regional consistency at orbital timescales. *G. ruber* $\delta^{18}O$ follows a broadly consistent pattern across sites on the eastern margin of India (Govil and Naidu, 2011; Rashid et al., 2011), offshore Ganges-Brahmaputra (Kudrass et al., 2001), Bengal Fan (Chauhan, 2003), and Andaman Sea (Rashid et al., 2007) (Fig. 1-11). Measurements of $\delta^{18}O_{sw}$ from *Globigerinoides sacculifer* at sites in the eastern Arabian Sea show a decreased input of low-salinity water from the Bay of Bengal during the LGM (Mahesh and Banakar, 2014). Unpublished analyses of *G. ruber* $\delta^{18}O$, SST, and $\delta^{18}O_{sw}$ from Site 19 (Schulenberg, 2011) are consistent with the broad LGM to present patterns across the northeast Indian Ocean. The longest Bay of Bengal $\delta^{18}O_{sw}$ salinity record (core KL-126), extending to 80 ka, shows paleo-salinities ranging from 33-35 ‰ between 20 and 80 ka, with a pronounced decrease to 10 ka, where salinity varies from 31 to 33 ‰ (Kudrass et al., 2001). Salinity and $\delta^{18}O_{sw}$ records across the Bay of Bengal correlate well to the $CaCO_3$ MAR at Site 19 and GISP2 dust/cation record, with higher $CaCO_3$ MAR occurring during periods of higher dust flux and Bay of Bengal salinity (Fig. 1-11).

Elevated primary production during this period, demonstrated by the increase in $CaCO_3$ MAR, may have been driven by regional aridification, that resulted in decreased freshwater influx to the Bay of Bengal, thus reducing stratification in the upper water column. In the Bay of Bengal, freshwater runoff restricts the mixing and upwelling of deep nutrients in the photic zone (Madhupratap et al., 2003; Prasanna Kumar et al., 2002). Freshwater runoff is not a significant source of nutrients in the Bay of Bengal (Madhupratap et al., 2003). Instead, increased precipitation and river outflow serves to increase stratification and limit biological productivity. In the modern Bay of Bengal, relatively fresh, nutrient-poor surface waters overly more saline, nutrient-rich intermediate and waters (Talley, 2013). During periods of reduced freshwater runoff and precipitation, such as the last glacial period, the higher salinity in the surface waters would serve to weaken the density gradient across the pycnocline and promote mixing and upwelling of nutrient-rich waters that could enhance biological productivity. Additionally, cooling of the surface waters during the LGM would further weakened the density gradient. $^{15}\delta$TN at Site 19 is enriched during glacial conditions, and then becomes more depleted in the Holocene, which is consistent with a decrease in productivity and denitrification (e.g. Altabet et al., 2002) with increased monsoon intensity. The shift in $^{15}\delta$TN observed in the Site 19 record may also be influenced by a decrease in terrestrial TOC inputs.

Bolton et al. (2013) show reduced stratification of the upper water column in the southernmost Bay of Bengal (ODP Site 758) during periods of increased monsoon intensity, primarily due to wind-mixing at 5 °N, far from the sources of freshwater input. Site 19 at approximately 19 °N, is located closer to freshwater sources in the northern Bay of Bengal and exhibits a strong stratification today that counteracts the effect of increased wind-mixing during the southwest monsoon. Compared to ODP Site 758, the opposite relationship between monsoon intensity and stratification likely exists in the freshened Mahanadi Basin, where periods of reduced monsoon intensity result in diminished stratification which, in spite of reduced wind-mixing, may stimulate productivity. Future work involving microfossil-based indicators of upwelling (e.g. Kroon et al., 1991) and stratification (e.g. Bolton et al., 2013) could further test the relationship of stratification and upwelling in the northern Bay of Bengal.

Globally, productivity is thought to increase during glacial periods (e.g. Sarnthein and Winn, 1990; Sarnthein et al., 1998), however there is large regional variation in the glacial-interglacial response of productivity, with some regions experiencing an increase of productivity during low stands (Pederson, 1983; Schrader, 1992), and in other regions an increase in productivity during high stands (Hermelin and Shimmield, 1995; Kumar et al., 1993), or even a varied response within a single region (Bertrand et al., 1996). The increase in productivity in the Bay of Bengal during glacial conditions shown by the elevated $CaCO_3$ MAR at Site 19, opposite that observed in the Arabian Sea (Emeis et al., 1995; Singh et al., 2011) and equatorial Indian Ocean (Bassinot et al., 2011; Bolton et al., 2013) where productivity is enhanced during interglacials and diminishes during glacials. Despite the influence of the Indian monsoon over the entire region, the response of productivity to the monsoonal winds is affected by local oceanographic conditions, in this case, surface salinity conditions. During the last glacial period a diminished southwest monsoon and enhanced northeast monsoon could have resulted in conditions more favorable to productivity than the modern ocean in a less-stratified water column, even with a decrease in wind-driven mixing.

As $CaCO_3$ MAR decreases to 0.2-0.5 g/cm/kyr throughout the Holocene, BSi MAR increases to 0.07 to 0.17 g/cm/kyr. $CaCO_3$ remains dominant relative to BSi even when $CaCO_3$ MAR is at a minimum. The range of BSi MAR between 0.01 and 0.17 g/cm/kyr is consistent with the longer term range of BSi observed at the Mahanadi Basin (Cawthern et al., 2014). The relative increase in BSi during high-stands and decreased salinity surface waters suggests a limited recovery in siliceous productivity under interglacial conditions, possibly due to enhanced fluvial SiO_4 delivery to the ocean, but overall decreased productivity ($CaCO_3$ MAR + BSi MAR) during periods of intensified southwest monsoon. The modern surface waters of the northern Bay of Bengal, while depleted in nitrate, have high silicate concentrations (Prasanna Kumar et al., 2002). Enhanced silicate flux to the Bay of Bengal may create an advantage for siliceous organisms allowing for diatoms and radiolarians to comprise a larger component of microplankton community throughout the Holocene.

Variation in marine productivity is not uniformly represented by $CaCO_3$ MAR or BSi MAR, and the sum of these is a better representation of total marine productivity, although this does not account for the contribution of non-calcareous and non-siliceous production such as from cyanobacteria and dinoflagellates. Due to the high input of terrestrial organic matter and influence of decomposition rates at the Mahanadi Basin (Krishna et al., 2013). TOC is not a good indicator of paleo-productivity at Site 19, as it is in the Arabian Sea (e.g. Ziegler et al., 2010). Plankton communities in the modern Bay of Bengal are diverse; sediment trap and plankton net studies reveal a mixture of diatoms, foraminifers, coccolithophores, copepods, cyanobacteria, dinoflagellates, and silicoflagellates (e.g. Gauns et al., 2005; Guptha et al., 1997; Jyothibabu et al., 2008; Madhu et al., 2006; Madhuprarap et al., 2003; Paul et al., 2007; Unger et al., 2003). Carbonate, opal, or organic carbon may be the dominant biogenic flux in these studies depending on location relative to mesoscale eddies and by monsoon season and this variability is not well-constrained on a regional scale. This modern diversity agrees well with the Holocene record of biogenic MAR at Site 19, in which $CaCO_3$:BSi is less than 6. Between 70 and 10 ka, $CaCO_3$:BSi increases to as high as 74, with a distinctly $CaCO_3$-dominant biogenic flux. This relationship suggests that over kyr-scale orbital timescales, analysis of one biogenic component may misrepresent paleoproductivity in the northern Bay of Bengal. During periods of a weakened southwest monsoon, BSi MAR will not capture the large $CaCO_3$ flux associated with upwelling. In contrast, during a strengthened monsoon and decreased $CaCO_3$ MAR, BSi becomes a relatively more important as an indicator of biological productivity.

Organic Carbon Sources

The δ^{13}TOC and C/N record is closely correlated with *Uvigerina peregrina* δ^{18}O (Fig. 1-12) indicating a strong influence of sea-level and/or associated regional climate changes on the source of TOC. The presence of C4 plant carbon is necessary to explain δ^{13}TOC greater than -20 ‰ that comprises most of the record at Site 19B. The C4 plant contribution to the Bay of Bengal has been significant since the Miocene, as shown by an increase in δ^{13}TOC from -24 to -27 ‰ to -15 to -24 ‰ at 7 Ma in Bengal Fan sediments (France-Lanord and Derry, 1994; Freeman and Colarusso, 2001). Based on vegetation modeling by Galy et al. (2008), the present-day Mahanadi River drains a tropical savannah to tropical seasonal biome with plant biomass with δ^{13}C between -26‰ to -14 ‰. During the LGM the Mahanadi watershed and other eastern Indian watersheds were largely semi-desert dominated by vegetation with δ^{13}C ranging from -20‰ to greater than -12‰ (Galy et al., 2008). Variation of δ^{13}TOC at Site 19 between -21‰ to -16 ‰ with more depleted δ^{13}TOC during low stands (Fig. 1-12) is consistent with the transition in terrestrial vegetation, reflecting increased δ^{13}TOC during colder, drier intervals such as the LGM. However, this variation could also indicate a decrease in marine organic matter. The increase in δ^{13}TOC through the Holocene in this record is consistent with aridification of the Indian subcontinent recorded in the Krishna-Godavari basin at NGHP-01-16A (Ponton et al., 2012). Our results compare well to the variation observed in the western Arabian Sea, eastern Bay of Bengal, and Andaman Sea (Fontugne and Duplessy, 1986), which also show an increase δ^{13}TOC during glacial intervals (OIS 2-4) compared to interglacials (Holocene and OIS 5) with a strong correlation to the benthic δ^{18}O record. Our δ^{13}TOC record is also consistent with the 84 to 18 ka record of δ^{13}C in soil organic carbon and carbonates in the Ganga Plain observed by Agrawal et al. (2012). A combination of increased terrigenous organic matter and/or drier conditions that allow for the expansion of C4 plants in India during sea-level low stands explains the shift in δ^{13}TOC observed in the Site 19B record.

C/N ratios follow a similar pattern to δ^{13}TOC, and a cross-plot of these parameters show a trend between a terrestrial end member with C/N > 12 and δ^{13}TOC > -17‰ and a marine end member with C/N of approximately 5 and δ^{13}TOC of approximately -20‰ (Fig 1-13). During the LGM, eustatic sea level was approximately 120 m lower than present (Fairbanks, 1989), and Site 19 was approximately 40 km offshore India, 30 km closer than present day, possibly allowing for shorter transport distance (and less time for decomposition) of terrigenous organic matter. In addition, decreased precipitation during a weakened southwest monsoon may decrease soil organic matter decomposition rates and increase the relative TOC content in terrigenous sediments. Rates of soil carbon decomposition, measured by soil CO_2 efflux, have been shown to decrease significantly under low soil moisture conditions (e.g. Davisdon et al., 2000; Orchard and Cook, 1983; Raich and Schlesinger, 1992; Savage and Davidson, 2001), and decreased CO_2 efflux has been observed during the NE monsoon in India (Gupta and Singh, 1981; Mohanty and Panda, 2011). In the Godavari River, less-degraded particulate organic carbon (POC) is more prevalent during the dry season than during the summer monsoon (Gupta et al., 1997). Likewise, in the Ganges-Brahmaputra and Indus Rivers, overall POC content and labile POC content in suspended material is higher during the low sediment discharge months of the NE monsoon (Ittekkot et al., 1986). Over orbital timescales, decreased SW monsoon intensity and precipitation, may result in higher terrestrial TOC content of sediments delivered to the Indian margin, despite lower sediment discharge, thus affecting C/N and δ^{13}TOC.

This C/N ratio vs. δ^{13}TOC trend approximately matches that observed across the northern Indian Ocean margins (Johnson et al., 2014) and other marine environments (Meyers, 1994). Potential caveats to using bulk C/N and δ^{13}TOC to determine organic matter sources include sorption of inorganic ammonia to clays (Müller, 1977) and potential variation in the C3 versus C4 contribution to terrestrial organic matter in the region. However, error from the sorption of inorganic N on clays would tend to decrease C/N ratios, thus the observed increases in C/N ratios are indicative of increased terrestrial TOC. Lower C/N values, however, can be interpreted both as an increase in marine organic matter and increased inorganic N fraction. δ^{13}TOC in the high range of our measurements (e.g. -16‰) strongly suggests the presence of C4 terrestrial plant organic matter. δ^{13}TOC variation towards the lower end of the our measurement range (e.g. -20‰) could be the result of either increased marine TOC or a shift in terrestrial plant biomass to C3 photosynthesis. However, using both δ^{13}TOC and C/N combined strengthens the ability to identify the presence of marine organic matter by minimizing the effect of potential errors and unaccounted factors in one measurement.

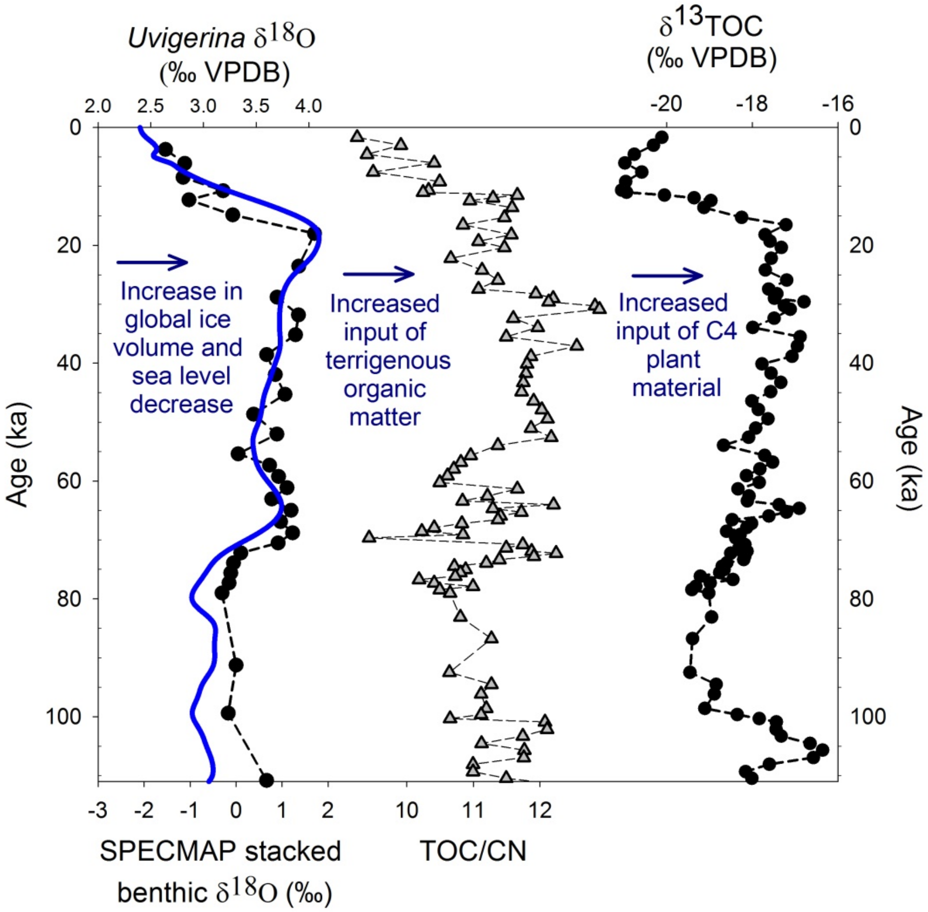

Fig. 1-12. Organic carbon sources correlated to glacial-interglacial changes in sea level and continental aridity. Low-stands correspond to increased flux of terrigenous organic matter including C4 plant material.

The range in TOC observed at Site 19 is similar to the range of TOC observed along the western Bay of Bengal margin (Krishna et al., 2013; Johnson et al., 2015), and the central and eastern Bay of Bengal (Fontugne and Duplessey, 1986). TOC content or TOC MAR at this site, however, does not exhibit a correlation with $CaCO_3$ or sea level, indicating a more complex relationship with paleoenvironmental conditions. In a continental slope environment, such as at Site 19, not only is TOC content driven by productivity (e.g Müller and Suess, 1979), it is influenced by terrestrial organic carbon fluxes (e.g. Burdige, 2005; Goñi et al., 2005; Hedges et al., 1997) and rates of decomposition (e.g. Canfield, 1994; Emerson et al., 1987; Versteegh and Zonneveld, 2002). Exposure to oxic bottom waters is a major factor in the decomposition of organic matter, with oxygen as the most efficient electron acceptor for TOC oxidation (Froelich et al., 1979). TOC content in general increases at sites with high SR due to decreased oxygen exposure (Müller and Suess, 1979; Stein, 1990). TOC MAR at Site 19 largely tracks lithogenic MAR and SR, suggesting higher SR enhances TOC preservation through burial.

Lithogenic Fluxes

Total lithogenic MAR, TOC MAR, and sand-sized content follow a similar pattern since 23 ka (Fig. 1-14). These parameters increase since the LGM with a slight decrease between 15 and 13 ka, reaching a peak at 12 to 11 ka. After the rapid increase at the glacial termination, lithogenic MAR, TOC MAR, and the sand size fraction decrease gradually throughout the Holocene. These values follow the trend in insolation values at 30° N (Berger and Loutre, 1991), varying on precessional timescales. Elevated monsoon intensity during periods of increased insolation drives a stronger southwest monsoon and precipitation over India, and subsequent weathering and transport of terrigenous materials. As the modern sediment discharge from the Mahanadi River occurs mainly during the months of peak SW monsoon precipitation (July, August, September), the amount of terrigenous discharge from peninsular India to the continental slope should increase during intensification of the monsoon. The increase in SR and lithogenic MAR at Site 19 since 12 ka (Fig. 1-14) is consistent with other studies in the Indian region that report increased erosion and sediment flux due to insolation-driven monsoon intensity during the early Holocene (Clift et al., 2008; Goodbred and Kuehl, 2000; Weber et al., 1997). This increase in lithogenic MAR is also consistent with Holocene increases in SR reported in the

Mahanadi Basin (Mazumdar et al., 2014) and Krishna-Godavari Basin (Mazumdar et al., 2009; Ponton et al., 2012). The age model by Mazumdar et al. (2012) at a nearby site in the Mahanadi Basin captures a large increase in SR (241 cm/kyr) since 1.2 ka that is not recorded at Site 19 (core top age 1.4 ka).

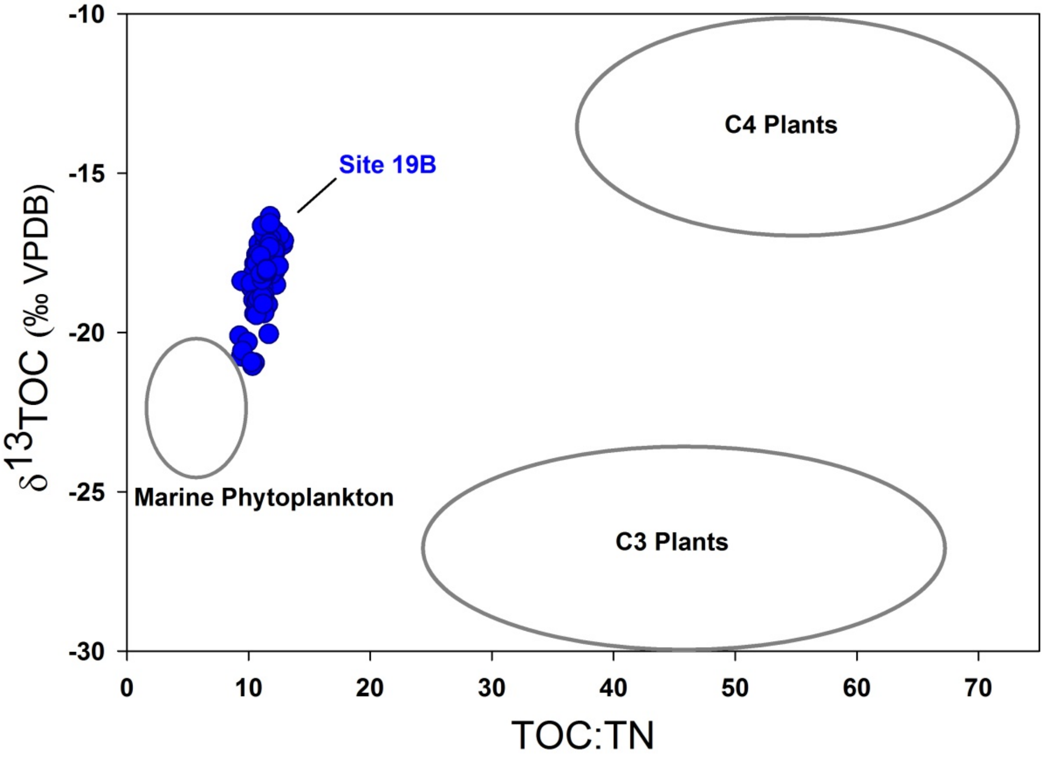

Fig. 1-13. TOC:TN versus δ^{13}TOC showing Site 19 sediments as a mixture of marine and terrestrial C4 organic matter. After Meyers, 1994.

Prior to 23 ka, the relationship between insolation and the record at Site 19 becomes unclear. Fewer age control points before 31 ka (seven since 31 ka and five between 100 and 31 ka), may limit the ability to observe changes in MAR occurring on precessional time scales, as SR changes are occurring between observed oxygen isotope events. A decrease in lithogenic MAR from 110 to 95 ka and increase from 85 to 79 ka, driven by changes in SR roughly correlates to the insolation pattern. There is a decrease in lithogenic MAR, however, that is driven by a decrease in bulk density and decreased sand-sized content between 69 and 60 ka that is close to an insolation minima at 72 ka, indicating a possible monsoon link. Change in SR on this margin may require higher sampling density for oxygen-isotope stratigraphy to reveal changes in MAR that are occurring on timescales shorter than the oxygen isotope events revealed by our sampling interval.

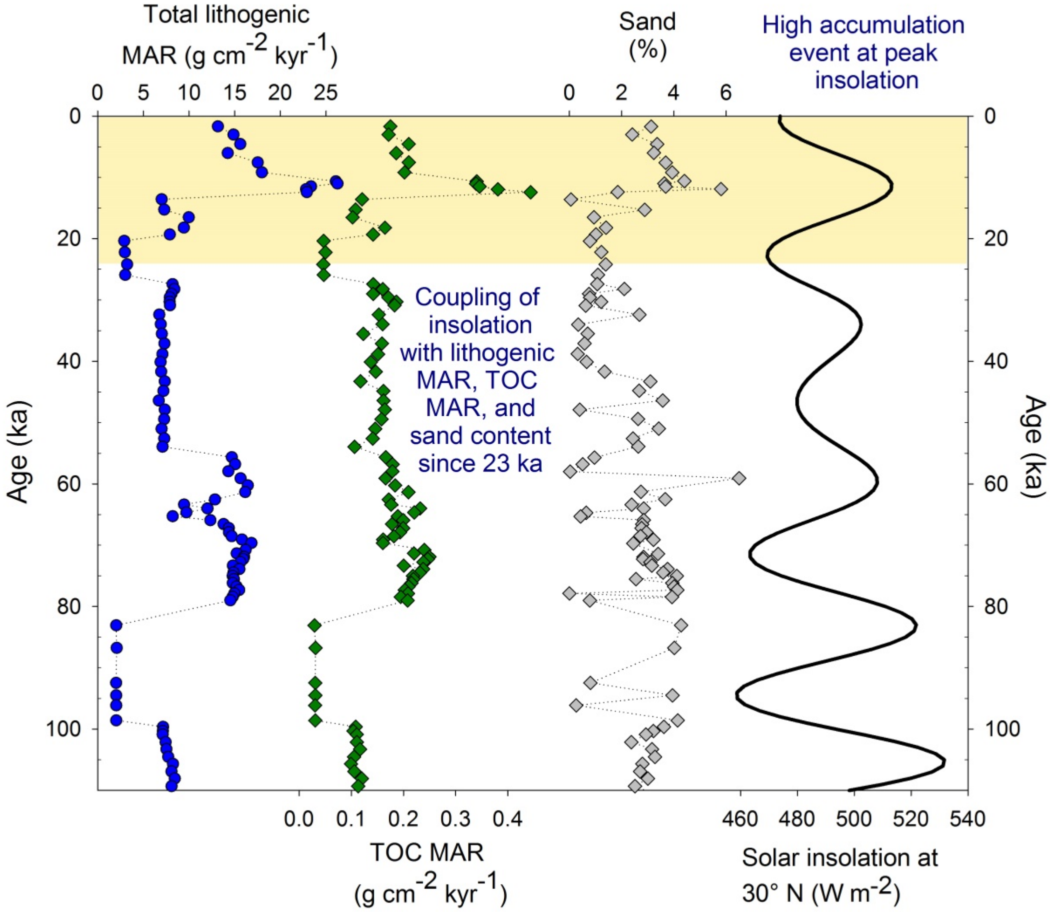

Fig. 1-14. Lithogenic MAR and TOC MAR plotted with solar insolation at 30°N (Tibetan Plateau) Since 23 ka, flux of lithogenic material and TOC increases solar insolation and Monsoon intensity. Before 23 ka, there is a weak correlation between solar insolation and MAR, possibly limited by the resolution of the age model.

The increase in MAR observed in the Holocene compared to the LGM suggests that this margin is supply-dominated and accumulation on the continental margin is controlled by sediment flux, rather than sea-level (e.g. Carvajal et al., 2009). An increase in grain size or SR would be expected at Site 19 during low-stands according to classic sequence stratigraphy (e.g. Posamentier et al., 1988; Vail et al., 1977) that is widespread in Quaternary depositional systems (Sømme et al., 2009). The increase in MAR and sand content since 12 ka at Site 19 indicates higher sediment accumulation on the continental slope occurs during high stands, as opposed to during low-stands via a shelf-edge deltas, suggesting that monsoon precipitation is a stronger control of sedimentation on the eastern Indian margin than sea-level.

Monsoon-influenced variation in MAR has implications for gas hydrates and early diagenesis in sediments of the Bay of Bengal Indian margin. SR and MAR have a direct influence on sediment overpressure (e.g Dugan and Sheahan et al., 2012), slope stability (e.g. Urlaub et al., 2012), and early diagenetic reactions dependent on diffusion of seawater (e.g. Kasten et al., 1998; Pruysers et al., 1993). Specifically, SR influences sulfate availability and consequently anaerobic oxidation of methane (e.g. Hensen et al., 2003; Riedinger et al., 2005). Along the eastern Indian margin, variation in SR between the Holocene and Late Pleistocene has been suggested to influence sulfate profiles and TOC availability for methanogeneis (Hong et al., this issue; Mazumdar et al., 2009, 2012; Solomon et al., 2014). Thus, the evolution Indian monsoon may be an important influence on the evolution of gas hydrate systems on the Indian margin.

Zr/Rb and Magnetic Susceptibility

Zr/Rb measured by XRF has been used as a grain-size proxy (Chen et al., 2006; Dypvik and Harris, 2001) due to enrichment of Zr in the coarse fraction from heavy mineral (zircon) content (e.g. Fralick and Kronberg, 1997) and enrichment of Rb in the fine fraction due to clays and/or muscovite/biotite (e.g. Heier and Billings, 1970). Zr/Rb at Site 19 does not covary with median lithogenic grain size, but rather with median bulk grain size, which includes a substantial biogenic component (Fig. 1-15). Curiously, Zr/Rb shows a strong correlation with $CaCO_3$. Zr/Rb is also highly correlated with κ and χ_{nc} suggesting that Zr/Rb is still a measure of the heavy mineral fraction that also contains ferrimagnetic minerals such as magnetite. The observation that Zr/Rb and magnetic susceptibility do not correlate to the mean lithogenic grain size, but rather $CaCO_3$ content that is driven by monsoon variability suggests that another factor other than grain size influences heavy mineral content and Zr/Rb.

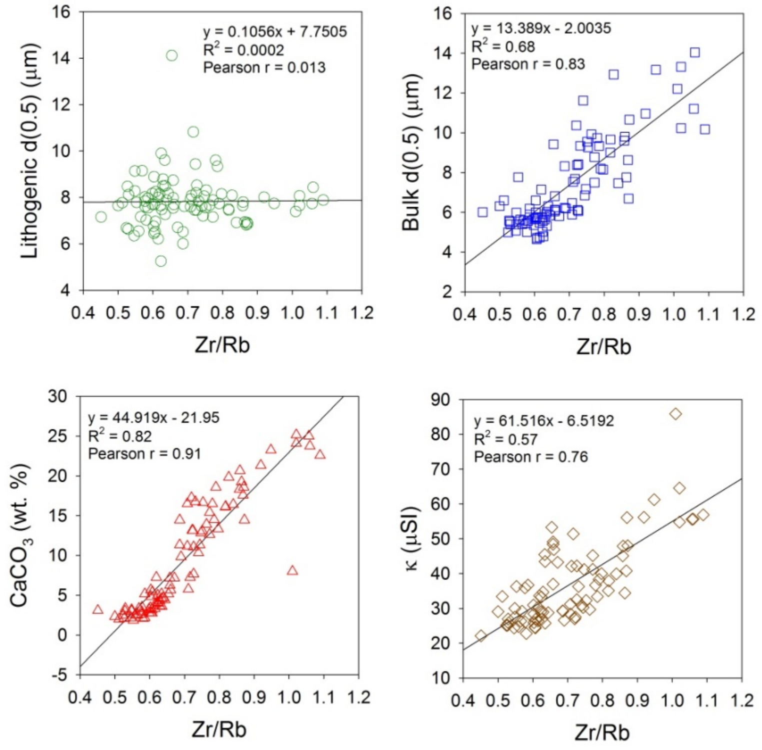

Fig. 1-15. Correlation of XRF Zr/Rb with lithogenic grain size, bulk (lithogenic +biogenic) grain size, $CaCO_3$, and magnetic susceptibility (κ). Linear regression presented with equation and goodness-of-fit (R^2). Pearson correlation coefficient (r) presented as a strength of linear correlation. There is no significant correlation between Zr/Rb and lithogenic grain size. Zr/Rb is strongly correlated with bulk grain size, $CaCO_3$, and κ.

Sediments at Site 19 are finer-grained and show little variation in grain size compared to other locations utilizing the Zr/Rb ratio (e.g. Chen et al., 2006; Dypvik and Harris, 2001), which may explain the deviation between Zr/Rb and carbonate-free grain size measurements. Median lithogenic grain size at Site 19 varies from 5 to 14 μm, and mean lithogenic grain size varies from 4.1 to 8.4 μm. Loess-paleosol sediments investigated by Chen et al. (2006) show more variation in grain size and are coarser-grained, with mean grain size ranging from 11.7 to 40.9 μm, and there is a strong correlation between Zr/Rb and grain size. The correlation between Zr/Rb and grain size is due to the increased abundance of heavy minerals in coarser sediments; the residual variation represents variation in Zr- and Rb-bearing minerals at a given grain size. In sediments where grain size variation is limited or with limited coarse mineral grains, the "noise" from variation in heavy mineral content at a given grain size may become the dominant signal over the co-variation of grain size and heavy mineral content.

If Zr/Rb and magnetic susceptibility are proxies of heavy mineral content, why do these parameters track with $CaCO_3$? In continental slope environments, increased κ during glacial periods are often driven by increases in ferrimagnetic minerals associated with higher silt and sand-sized lithogenic content (e.g. Bloemendal et al., 1992; Vanderaveroet, et al., 1999). However, κ does not correlate to carbonate-free grain size at Site 19. A strong correlation with Zr/Rb (Fig. 1-15) suggests that κ is dominantly sourced by ferrimagnetic lithogenic minerals and not by magnetotactic bacteria or authigenic magnetic minerals such as gregite. Colin et al. (1998) report increases in κ and magnetic grain size during glacial periods (MIS 2, 4, and 6) in the Bay of Bengal (Core MD77-180) on the continental slope offshore the Ganges/Brahmaputra Rivers), which they attribute to decreased chemical weathering during a weakened summer monsoon. Sangode et al. (2001) and Tripathy et al. (2011) also report increases in κ during the

LGM in the western Bengal Fan (Core SK181/PC33, and SM43 cores, northeast of the Krishna-Godavari Basin). This increase in κ is attributed to reduced input of Ganges-Brahmaputra sediment due to decreased monsoon-driven erosion (Rahaman et al., 2009) and increased glacial cover (Owen et al., 2002), leaving a relative increase in peninsular India-derived sediments which erode Deccan flood basalts high in titanomagnetite content (Courtillot et al., 1986; Sager and Hall, 1990). Elemental and isotopic sediment chemistry from the western Bay of Bengal also indicates reduced Himalayan input during the LGM (Tripathy et al., 2011; 2014).

At Site 19, magnetic susceptibility (κ, χ_{nc}) are correlated with Ti/Fe, with an increase in χ_{nc} occurring when Ti increases relative to Fe (Fig. 1-16). Total Fe, which is incorporated in ferrimagnetic iron oxides, as well as paramagnetic pyrite, pyroxene, amphibole, and clays (illite, smectite- and chlorite-group), decreases through the LGM. Total Ti increases through the LGM, representing heavy minerals such as ilmenite, rutile, sphene, and titanomagnetite. The strong negative correlation between Ti/Fe and χ_{nc} suggests the Ti-bearing heavy minerals (magnetite-titanomagnetite series) contribute to the magnetic susceptibility pattern, and the down-core Fe pattern is also influenced by paramagnetic clays and authigenic pyrite. A small amount (1-2%) of iron sulfides were observed in smear slides of the upper 12 m at Site 19 (Collett et al., 2008) and Fe-bearing clays (illite, smectite-group, and chlorite group) were also observed via XRD (Phillips et al., this issue). Based on the properties of magnetite (Blum, 1997), a small change in magnetite content on the order of 0.2 wt. % could drive the variability in χ_{nc} (30 to 130 x 10^{-8} kg m^{-3}) observed at Site 19, a variation that seems plausible in the absence of significant grain size variation.

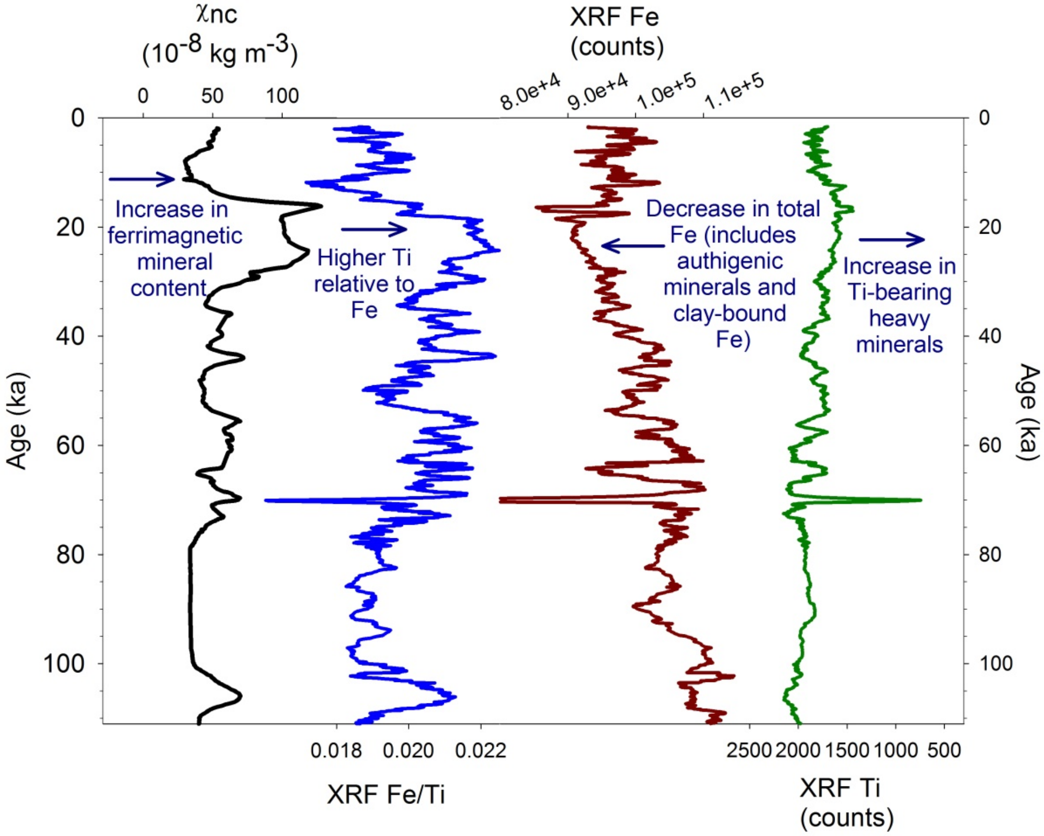

Fig. 1-16. Variation in χ_{nc}, and Fe, Ti, and Ti/Fe measured by XRF (adjusted for the carbonate-free fraction). Fe/Ti is highly correlated to χ_{nc},.

The same decrease in monsoonal precipitation during glacial periods that drives increased $CaCO_3$ production could potentially reduce chemical weathering that increases Zr/Rb and κ. The chemical index of alteration (CIA) (Nesbitt and Young, 1982) and other indicators of weathering intensity have been shown to decrease with a reduction in southwest monsoon intensity and subsequent rainfall (Colin et al., 1998, 1999, 2006; Limmer et al., 2012), increasing the ratio of primary (e.g. feldspars, pyroxene, magnetite, zircon) to secondary minerals (clays). A similar effect may be evident at Site 19 and this mechanism likely could result in an enrichment of Zr-bearing heavy minerals during glacial periods relative to Rb-bearing minerals. At Site 19, Rb decreases during colder periods and Zr increases (Fig. 1-17), consistent with an increase in zircon (primary mineralogy) and decrease in clays (secondary), even in the absence of substantial grain size variation. This variation in Rb is opposite that observed by Colin et al. (2006) in sediments influenced by the Irrawaddy River with glaciated headwaters, where mechanical weathering increased Rb content even in periods of decreased chemical weathering. This discrepancy may suggest that the weathering response in sediments derived from the Indian Shield, may be different than in those derived from the Himalayas, Tibetan Plateau and Indo-Burman ranges. Lag times between erosion of Himalayan/Tibetan sources and marine deposition may exceed 10 kyr (Blöthe and Korup, 2013; Clift and Giosan, 2015). Thus, differences in terrestrial sediment storage may exist between rivers draining the Indian Shield and those draining mountainous regions, which could potentially impact the timing of variation of marine elemental proxy records. Future work involving geochemical weathering proxies and provenance analyses could provide more direct indicators of chemical and physical weathering of peninsular India.

Implications and Conclusions

Measuring multiple lithogenic and biogenic sedimentary constituents and calculating MAR, along with isotopic analyses, allows for the partitioning of multiple monsoon- influenced terrigenous fluxes and biological productivity in a single marine sediment record from the northern Bay of Bengal. An implication of this multiple-proxy approach is that glacial-interglacial changes in monsoon rainfall variation drive a regional response in productivity, weathering, and sediment accumulation rates on the Indian continental margin (Fig. 1-18). A hemipelagic continental slope record such as that preserved at Site 19 allows for both terrestrial and marine processes to be reconstructed from the depositional record.

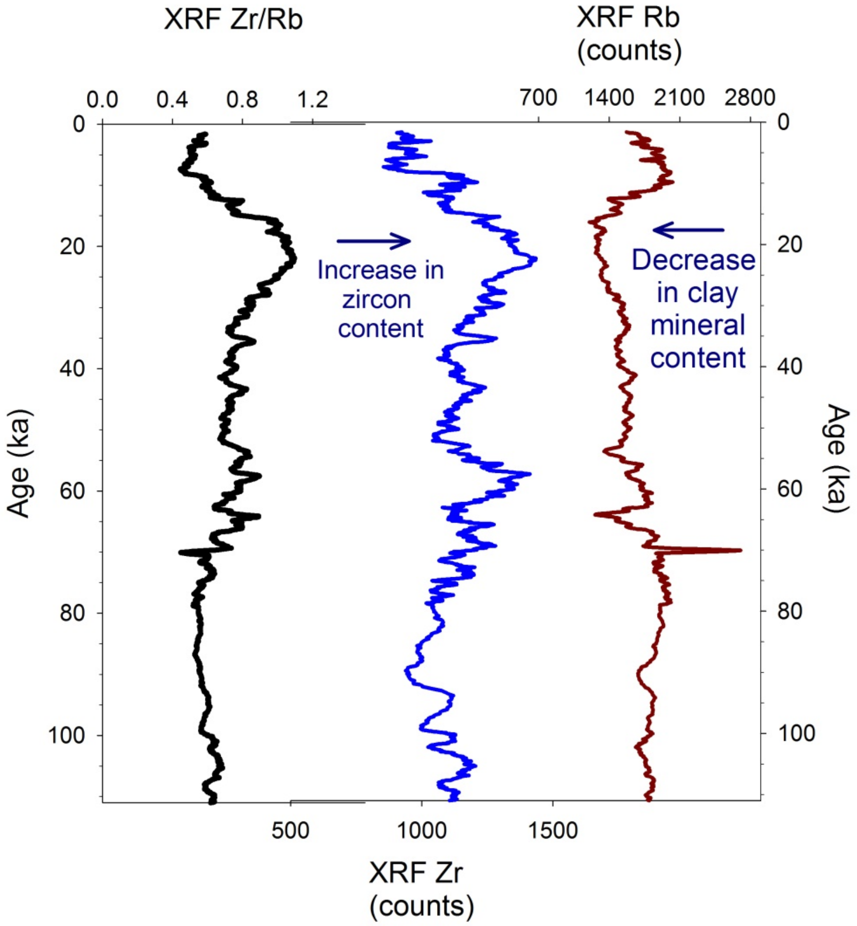

Fig. 1-17. Variation in Zr/Rb, Zr, and Rb as measured by XRF (adjusted for the carbonate-free fraction). Zr increases, and Rb decreases during glacial periods.

$CaCO_3$ MAR at Site 19 is elevated and variable between 70 and 10 ka, and is correlated with dust and cation content on the Greenland ice sheet, as well as $\delta^{18}O_{sw}$ paleo-salinity indicators from multiple locations in the Bay of Bengal. A weakened southwest monsoon under glacial conditions, resulting in decreased precipitation, increased the salinity of the surface waters in Bay of Bengal. Biological productivity in the modern Bay of Bengal is limited by stratification due to freshwater runoff, and I suggest that the increased production of $CaCO_3$

during glacial conditions was a result of decreased stratification due to increased aridity across the Indian subcontinent and Tibetan Plateau.

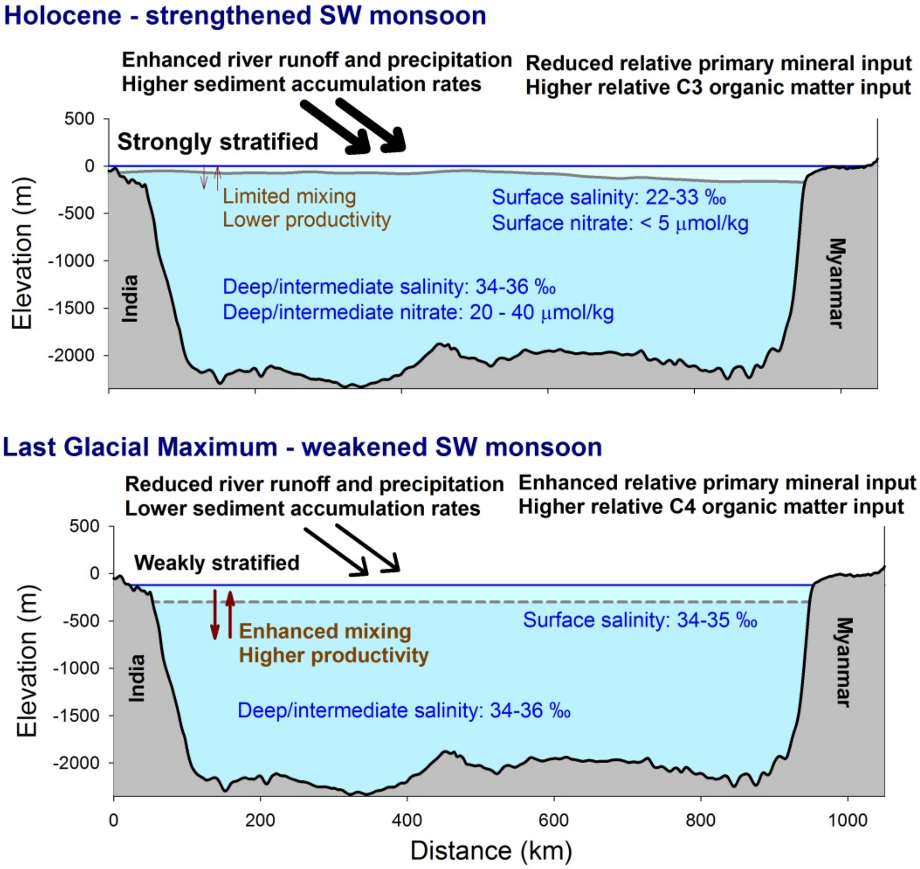

Fig. 1-18. Schematic summary of enhanced productivity, reduced weathering, lower sedimentation rates, and increase in higher terrestrial C4 organic matter delivery in the northern Bay of Bengal during glacial periods compared to interglacials. Productivity in the modern Bay of Bengal is limited by stratification from high freshwater input (Kumar et al., 2002; Madhupratap et al., 2003). Widespread aridity during the last glacial period increased surface salinity in the Bay of Bengal (Cullen, 1981; Kudrass et al., 2001; Rashid et al., 2011). Decreased surface salinity reduced stratification and promoted mixing and upwelling of nutrient-rich water, stimulating productivity and $CaCO_3$ MAR in the Bay of Bengal. Reduced precipitation and weathering increased primary mineral content, shown by elevated magnetic susceptibility and Zr/Rb. Reduced rainfall also increases the prevalence of C4 plants relative to C3 plants, and likely decreases rates of terrestrial organic matter decomposition, increasing the delivery of terrestrial TOC to the Indian margin.

TOC variation at Site 19 is influenced by a variety of factors including terrestrial organic matter flux, biological productivity, and SR. TOC MAR is correlated with lithogenic MAR, suggesting preservation of organic matter is influenced by terrigenous sediment flux. TOC/CN varies with sea-level, and higher terrestrial organic matter input occurs during low-stands which becomes more marine in source during the Holocene. δ^{13}TOC variation reveals increased C4 plant input during low-stands that either contains more C3 plant material or marine organic matter during high-stands. δ^{13}TOC and C/N are likely influenced by a combination of changes in C4 and C3 distribution, and changes in terrestrial organic carbon decomposition rates.

Lithogenic MAR, TOC MAR, and sand content track with insolation since 23 ka, suggesting monsoon-driven weathering strongly controls sediment supply. The highest lithogenic MAR occurs during the Holocene, suggesting that the monsoon influences continental slope sedimentation in the Bay of Bengal more strongly than sea level. Correlation between insolation and these measurements were not observed before 23 ka, possibly due to decreased resolution in the depth-age model.

The grain size proxy Zr/Rb from XRF tracks closely with bulk median grain size, largely influenced by sand-sized foraminifers, and $CaCO_3$, but not lithogenic median grain size. Zr/Rb correlates strongly with magnetic susceptibility indicating covariation of heavy minerals (zircon and ferrimagnetic minerals such as magnetite and titanomagnetite.) I suggest that in fine-grained marine sediments the grain-size proxy Zr/Rb from XRF may be more specifically a proxy for heavy minerals, and that in sediments of limited grain size variation this proxy is decoupled from co-variation with grain size. At Site 19, the increase in Zr/Rb under more arid glacial conditions likely represents increased primary mineral content relative to secondary minerals due to decreased chemical weathering.

Overall, I provide a new record of deposition in the eastern continental slope of India. The Bay of Bengal, especially along the peninsular Indian margins are relatively under-studied, and cores recovered during NGHP-01 have provided an opportunity to expand the record of monsoon-influenced sedimentation. The analysis of the upper 11.5 m of Site 19, an interval not significantly altered by diagenesis, extends the understanding of the Indian monsoon by providing a record of the previous 110,000 years in the Mahanadi Basin. Future work could improve the record of past monsoon variation on the Indian margin with higher resolution and back through multiple glacial-interglacial cycles to capture suborbital variation and address leads/lags with other sites influenced by the Asian monsoon system. However, the interpretation of deeper intervals at this site and other regions along the Indian margin affected by methane-related diagenesis (e.g. Collett et al., 2008; Mazumdar et al., 2009; 2014) may require consideration of the effect of diagenetic overprints on records of magnetic susceptibility and isotopic composition of foraminifers (e.g. Riedinger et al., 2005; Torres et al., 2003). The record I present here represents a 110 kyr segment of a Mahanadi Basin record that exhibits high variation in $CaCO_3$, δ^{13}TOC, and κ since 1.96 Ma. The observations from this higher resolution record will allow for better interpretation Quaternary monsoon variability in the Bay of Bengal. Our results from Site 19 suggest that measurement of multiple proxies within the same record is essential for linking terrestrial flux proxies and paleoceanographic changes resulting from variation in monsoon intensity.

2. TRACKING ORIGINS OF DIAGENETIC ALTERATION OF MAGNETIC SUSCEPTIBILITY IN METHANE-RICH MARINE SEDIMENTS OF THE CASCADIA MARGIN

ABSTRACT

Magnetic susceptibility (κ) is a mixed signal in marine sediments, representing primary depositional and secondary diagenetic processes. Production of hydrogen sulfide via anaerobic oxidation of methane (AOM) at the sulfate-methane transition (SMT), and organoclastic sulfate reduction above the SMT can result in the dissolution of iron oxides, altering κ in sediments in methane gas and gas hydrate bearing regions. I investigated records of κ on the Cascadia margin (ODP Sites 1249 and 1252; IODP Site 1325) using a Zr/Rb heavy mineral proxy from XRF core scanning to identify intervals of primary detrital MS and predict intervals affected by magnetite dissolutions. I also measured total sulfur content, grain size distributions, total organic carbon (TOC) content, and magnetic mineral assemblage. The upper 100 m of Site 1252 contains a short interval of κ driven by primary magnetite, with multiple intervals (> 90 m total) of decreased κ correlated with elevated sulfur content, consistent with dissolution of magnetite and re-precipitation of pyrite. In the upper 90 m of Site 1249, κ is almost entirely altered by diagenetic processes, with much of the low κ explained by a high degree of pyritization, and some intervals affected by precipitation of magnetic iron sulfides. At Site 1325, κ between 0-20 and 51-73 mbsf represents primary mineralogy, and in the interval 24-51 mbsf, κ may be reduced due to pyritization. This integrated approach allows for a prediction of primary κ and the amount of κ loss at each site when compared to actual κ measurements. In the case of magnetite dissolution and full pyritization, these drawdowns of κ are supported by sulfur measurements. The presence of methane and methane hydrates at these sites, as well as large variations in TOC

content, suggest that both variations in sulfate reduction rates and past migration rates of the SMT may influence κ alteration along the Cascadia margin.

INTRODUCTION

Magnetic susceptibility, measured as volume-dependent (κ) or mass-dependent (χ) magnetic susceptibility is a measure of the ratio of induced temporary magnetization to an applied field and is proportional to the quantity of ferromagnetic minerals in a material. Magnetic susceptibility is a widely-measured parameter applied to samples from sediment records, often applied with other rock magnetic techniques, to address a variety of environmental and diagenetic questions (e.g. Liu et al., 2012; Verosub and Roberts, 1995).

Magnetic susceptibility is commonly measured in marine sediments, and κ is a standard measurement using MSCL core scanning in cores recovered during Ocean Drilling Program (ODP) and Integrated Ocean Drilling Program (IODP) expeditions (Blum, 1997). Downcore variation in magnetic susceptibility can represent a variety of depositional features, including turbidites (Goldfinger et al., 2012; Karlin and Abella, 1994; Kirby et al.,1998; Sager and Hall, 1990; Taira and Niitsuma, 1986), eolian transport (Bloemendal et al., 1992; Doh et al., 1988; Lowrie and Heller, 1982; Robinson, 1986), and ice-rafted debris (Hall and King, 1989; Richter et al., 2001; Stoner et al., 1995). These detrital patterns represent the accumulation of iron oxide minerals, such as magnetite (Fe_3O_4), hematite (Fe_2O_3), and goethite ($\alpha FeOOH$) in marine sediments.

After deposition, these magnetic iron oxides are subject to reaction with hydrogen sulfide produced during early diagenesis. In marine sediments, hydrogen sulfide is produced by sulfate-reducing bacteria via organoclastic sulfate reduction (Eq. 1) (e.g. Berner et al., 1970):

$$2CH_2O + SO_4^{-2} \rightarrow H_2S + 2HCO_3^{-} \qquad (1)$$

In addition, at the sulfate-methane transition (SMT) hydrogen sulfide is produced by a consortium of sulfate-reducing bacteria and methanotrophic archea (Eq. 2) (Boetius et al., 2000; Hinrichs et al., 1999; Hoehler et al., 1994) or by methanotrophic archaea alone (Milucka et al., 2012) (Eq. 3), during anaerobic oxidation of methane (AOM) (Reeburgh, 1976):

$$CH_4 + SO_4^{2-} \rightarrow HCO_3^- + HS^- + H_2O \qquad (2)$$

$$7CH_4 + 8SO_4^{2-} + 5H^+ \rightarrow 4HS^- + 7HCO_3^- + 11H_2O \qquad (3)$$

Hydrogen sulfide reacts with dissolved iron and reactive iron minerals through multiple intermediate reaction steps to ultimately form pyrite (Berner, 1970, 1984; Rickard et al., 1995; Schoonen, 2004). Magnetite reacts readily with hydrogen sulfide to liberate iron and elemental sulfur (Eq. 4) (Pyzik and Sommer, 1981) which rapidly forms amorphous iron monosulfides, such as mackinawite (Eq. 5) (Berner, 1970; Pyzik and Sommer, 1981):

$$Fe_3O_4 + HS^- + 7H^+ \rightarrow 3Fe^{2+} + S^0 + 4H_2O \qquad (4)$$

$$Fe^{2+} + HS^- \rightarrow FeS + H^+ \qquad (5)$$

Further reaction of FeS to pyrite can occur via three possible mechanisms. These reactions include continued reaction with hydrogen sulfide (Eq. 6) (Rickard and Luther, 1997), addition of sulfur (Eq. 7) (Berner, 1970, 1984), and loss of iron (Eq. 8) (Wilkin and Barnes, 1996):

$$FeS + H_2S \rightarrow FeS_2 + H_2 \qquad (6)$$

$$FeS + S^0 \rightarrow FeS_2 \qquad (7)$$

$$2FeS + 2H^+ \rightarrow FeS_2 + Fe^{2+} + H_2 \qquad (8)$$

Of these potential reactions, Eq. 6 is thermodynamically most likely, if hydrogen sulfide is present (Rickard, 1997).

Pyrite may also be formed from FeS via steps involving intermediate magnetic iron sulfides, such as greigite, which is a product of sulfur (polysulfide) and FeS (Eq. 9) (Sweeney and Kaplan, 1973):

$$3FeS + S^0 \rightarrow Fe_3S_4 \qquad (9)$$

Similar to the reaction of FeS to FeS_2, greigite may experience further sulfidization via further reaction with hydrogen sulfide (Eq. 10) (Neretin et al., 2004), addition of sulfur (Eq. 11) (Sweeney and Kaplan, 1973), and loss of iron (Eq. 12) (Furukawa and Barnes, 1995):

$$Fe_3S_4 + 2H_2S \rightarrow 3FeS_2 + 2H_2 \qquad (10)$$

$$Fe_3S_4 + 2S^0 \rightarrow 3FeS_2 \qquad (11)$$

$$Fe_3S_4 + 2H^+ \rightarrow 2FeS_2 + Fe^{2+} + H_2 \qquad (12)$$

Given the potential for dissolution of magnetic iron oxides and formation of diagenetic iron sulfides in marine sediments, their primary magnetic mineral assemblage may be altered (e.g. Nilsson et al., 2013; Roberts and Turner, 1993). Diagenetic overprints of primary depositional κ signals in methane-bearing stratigraphy have been identified in a variety of marine sediment records (e.g. Kasten et al., 1998; Musgrave and Hiroki, 2000). Magnetite dissolution occurs relatively rapidly during exposure to H_2S with a half life (exposed to1 mM H_2S) on the order of decades to centuries (Canfield et al., 1992; Poulton et al., 2004). This reactivity allows for observable alteration in magnetic susceptibility during early diagenesis. Often magnetite content and magnetic grain size decreases with depth in the sulfate-reducing zone as sulfide solids increase (Karlin and Levi, 1985, Karlin, 1990) due to pyritization of magnetite (Canfield and Berner, 1987). A prolonged pause in upward SMT migration (Riedinger et al., 2005) or high sustained methane flux at a methane vent (Novosel et al., 2005) may produce reductions in κ via dissolution of ferromagnetic magnetite and precipitation of paramagnetic pyrite. Magnetic iron sulfides have been observed in gas hydrate settings (Housen and Musgrave, 1996; Kars and Kodama, 2013; Larrasoaña et al., 2006, 2007; Musgrave et al., 2006), maintaining or increasing κ. Thus, κ records in methane-bearing stratigraphy represent a potentially-mixed detrital and diagenetic signal (Johnson et al., 2010). Zr/Rb as measured by X-ray fluorescence (XRF) has been utilized as a grain size proxy (Dypvik and Harris, 2001). More specifically, Zr/Rb is an indicator of heavy mineral content in the absence of grain size variation, and in unaltered hemipelagic sediments can be highly correlated with κ (Phillips et al., 2014). By using Zr/Rb to predict detrital κ, I can unravel the detrital and diagenetic components in the κ signal (Johnson et al., in prep).

In this chapter, I investigate the source of magnetic susceptibility variation in the upper 100 mbsf at three sites (Fig. 2-1) along the Cascadia accretionary wedge (ODP Sites 1252 and 1249; IODP Site U1325) further applying and testing the method of (Johnson et al., in prep) to partition the κ signal into detrital and diagenetic components. I integrate the κ and XRF data with measurements of isothermal remanent magnetism (IRM), total organic carbon (TOC), and age models at each of the sites. These sites encompass a range in diagenetic environment from a methane vent site (ODP Site 1249) with high gas hydrate saturation to two slope basin sites (ODP Site 1252 and IODP Site U1325) with lower methane flux and observed gas hydrate. Each site shows intervals of very low κ that may represent diagenetic dissolution, which is now below the modern SMT (Fig. 2-2). By accounting for predicted κ, I estimate the loss of magnetite and pyrite sulfur precipitation to identify intervals of diagenetic alteration in these gas hydrate bearing records.

GEOLOGIC AND OCEANOGRAPHIC SETTING

Tectonic Setting and Terrigenous Inputs

The formation and continued evolution of the Cascadia accretionary wedge is a result of the oblique subduction of the Juan de Fuca, Gorda, and Explorer plates, where abyssal plain sediments are accreted and uplifted into a series of thrust ridges and slope basins. Abyssal plain sediments of these plates are dominated by turbidites and hemipelagic clays of the Astoria and Nitinat Fans. In the accretionary wedge, uplifted sediments on the structural highs, such as Hydrate Ridge are eroded and re-deposited in the slope basins with interspersed hemipelagic clay. Seismic reflection data across Hydrate Ridge sites (Tréhu et al., 2004) show the ridge is composed of uplifted and accreted abyssal plain fan sediments covered by various-age slope-basin sediments, which are in turn uplifted and deformed during the continued evolution of the wedge.

Primary detrital magnetic susceptibility in Cascadia margin sediments is sourced by sediment transport to abyssal plain and subsequent uplift and re-deposition of ferromagnetic minerals. Erosion of magnetite and titanomagnetite-bearing Columbia River Basalts (Long and Wood, 1986) and Cascade Arc volcanism (Jicha et al., 2009) serve as potential provenance for magnetite delivered to the continental shelf. These sediments are transported to the abyssal plain through turbidites and other mass flows, often through established submarine canyons e.g., through Astoria Canyon to the Astoria Fan, and through the Barkley and Juan de Fuca Canyons to the Nitinat Fan. Along the Cascadia margin, magnetite is commonly observed in sediments of abyssal fans and in the accretionary complex (Chamov and Murdmaa, 1995).

Physical Oceanography

Marine organic matter along this margin is sourced by primary productivity that is influenced by the dynamics associated with the splitting of the North Pacific current into the Callifornia Current and the Alaska Current. Phytoplankton production in the southern Cascadia region is primarily driven by Ekman-driven coastal upwelling associated with the California current (Lynn and Simpson, 1987), the southward flowing component of the North Pacific Gyre. In spite of the downwelling nature of the Alaska current, the northern Cascadia region remains productive, due to upwelling driven by mesoscale eddies (Peterson et al., 2005) and injection of nutrient-rich bottom water to the continental shelf during summer weakening of the Alaska current (Childers et al., 2005). Along the southern Cascadia margin, productivity and TOC accumulation are likely driven by the California Current, which influences productivity on glacial-interglacial and suborbital timescales further to the south along the California margin (Gardner et al., 1997).

TOC measured along the Cascadia margin is a mixture of marine and terrestrial organic matter (Prahl et al., 1994; Kim and Lee, 2009). The terrestrial component is highest on the continental slope (mean δ^{13}TOC=-23.9‰), and decreases to the continental slope and abyssal plain (mean δ^{13}TOC=-21.8‰ and -21.4‰ respectively) along the Washington margin (Prahl et al., 1994). TOC generally increases at the slope and abyssal plain compared to the shelf. At sites along the Northern Cascadia margin, δ^{13}TOC is generally more depleted (-24 to -26‰) and the most landward sites of the IODP Exp. 311 transect, have slightly less depleted δ^{13}TOC indicating the highest marine organic matter component (Kim and Lee, 2009). The differences between these sites suggest that TOC content and source vary along the slope depending on terrigenous flux and surface biological productivity.

Lithostratigraphy and Geochemistry: ODP Sites 1249 and 1252; IODP Site U1325

Site 1249 is located at the summit of southern Hydrate Ridge in 775 m water depth (Shipboard Scientific Party, 2003a) in a region of observed seafloor gas hydrate and methane venting (Heeschen et al., 2003, 2005; Suess et al., 1999, 2001). Unit I in the upper 51.5 m of Site

1249 is comprised of nannofossil- and diatom-bearing silty clay and diatom-rich silty clay. Unit II, between 51.5 and 90 mbsf is characterized by diatom-bearing to –rich silty clay, with intervals of nannofossil-bearing to –rich silty clay, and minor turbidite lithologies. Mousselike and soupy textures are common throughout Site 1249 representing the dissociation of disseminated and massive gas hydrate (Shipboard Scientific Party, 2003a). Iron sulfides were commonly observed throughout Site 1249 cores, and iron sulfide nodules and authigenic carbonate-rich clay were also observed.

The absence of sulfate and presence of methane at the seafloor at Site 1249 indicates direct flux of methane to the seafloor with an SMT at the sediment surface (Shipboard Scientific Party, 2003a). Observations of *Beggiatoa* microbial mats and seafloor AOM (Boetius et al., 2000) and methane-derived authigenic carbonates (Bohrmann et al., 1998; Greinert et al., 2001; Ritger et al., 1987; Suess et al., 1999) at Hydrate Ridge suggests Site 1249 is representative of widespread methane expulsion at the summit of Hydrate Ridge. Positive chloride anomalies in pore waters at Site 1249 suggest formation of gas hydrate and subsequent brine formation at rates faster than removal by diffusion or advection (Shipboard Scientific Party, 2003a). Enhanced salinity due to hydrate formation promotes a three-phase equilibrium between methane hydrate, dissolved methane, and water, and allows methane to be transported through the gas hydrate stability zone (Liu and Flemings, 2006).

Site 1252 is located in a slope basin approximately 4.5 km NE of the southern Hydrate Ridge summit in 1040 m water depth (Shipboard Scientific Party, 2003b). Unit I (upper 96.4 mbsf) is comprised of diatom-bearing to –rich silty clay. There is a regional unconformity at 96.4 mbsf and Unit II (96.4 -113.9 mbsf) is foraminifer-rich silty clay punctuated by layers of upward-fining turbidites. Unit III (113.9-259.8 mbsf) is comprised of silty clay with sandy silt turbidites. Iron sulfide mottles and nodules were commonly observed at this site. Sulfate decreases linearly to the SMT at approximately 5 mbsf (Shipboard Scientific Party, 2003b) and methane is present in headspace samples below the SMT. Distinct chloride anomalies were not observed at Site 1252, but cold anomalies were observed at 83 and 99 mbsf (Shipboard Scientific Party, 2003b).

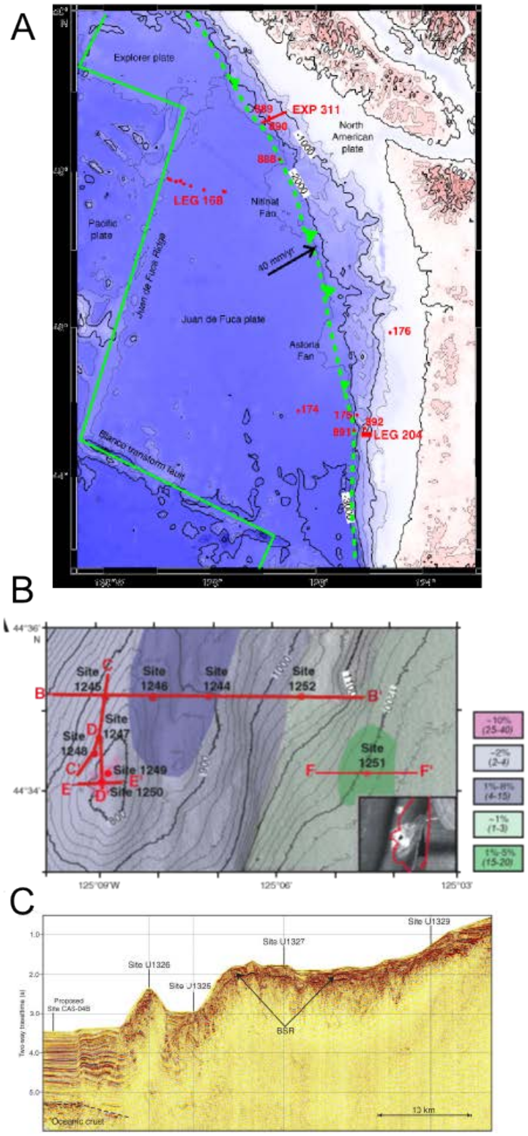

Figure 2-1. A. Location map showing the location of ODP Leg 204 and IODP 311 transects. From Tréhu et al., 2006, Fig. F1. B. Location of Hydrate Ridge sited drilled during ODP Leg 204 and estimated gas hydrate saturations (From Tréhu et al., 2006, Fig. F2) (Seismic reflections lines across each site, not shown here, are also shown in Trehu et al, 2006). C. Seismic section of Expedition 311 drilling sites. From Expedition 311 Scientists, 2006 Fig. F3.

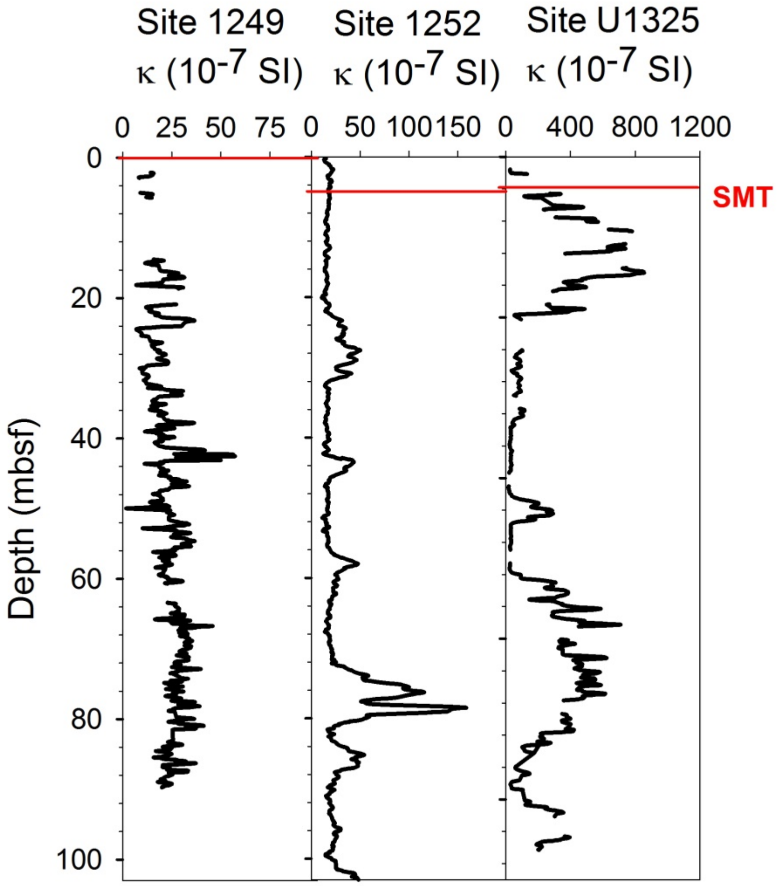

Figure 2-2. Magnetic susceptibility profiles at ODP Hole 1252A, ODP Holes 1249BCDF, and IODP Hole U1325B, shown with the depth of the modern SMT. κ and SMT depth from Shipboard Scientific Party (2003a,b) and Expedition 311 Scientists (2006).

Site U1325 is located in 2195 m water depth in the first slope basin landward of the deformation front on the primary transect drilled by IODP Expedition 311 (Expedition 311 Scientists, 2006). Unit I (0-52.2 mbsf) is comprised of silty clay containing diatoms, and sand layers ranging from mm to m in thickness. Unit II (52.2-102.3 mbsf) is comprised of silty clay and clayey silt interbedded with sand, silty sand, and sandy silt. Iron sulfide mottling and concretions are common throughout these records. The SMT is located between 4 and 5 mbsf at

Site 1325 (Expedition 311 Scientists, 2006). Freshened chloride anomalies below 70 mbsf indicate the dissociation of gas hydrate.

METHODS

Sediment core sections from Sites 1249, 1252, and U1325 were scanned at a 4 cm resolution using an Avaatech X-ray fluorescence (XRF) core scanner at Texas A&M University. The 4 cm measurement interval was adjusted in some intervals to avoid expansion cracks or moussey/soupy textures. XRF scanning was conducted at 10 kV (no filter), 25 kV, (Pd filter), and 50 kV (Cu filter) energy levels. Elements measured include Zr, Rb, S, Fe, Ti, Ba, and Br (see Table 1 for full list). Normalized ratios of XRF Fe to κ (Hepp et al., 2009) were calculated to identify intervals with abundant paramagnetic iron minerals (e.g. pyrite).

Grain size distributions of discrete sediment samples (~0.5 cm^3 of sediment approximately every 1 m) were measured for Sites 1249, 1252, and U1325 using a Malvern Mastersizer 2000 laser diffraction particle size analyzer and Hydro 2000G dispersal unit at the University of New Hampshire. Bulk samples were measured, as well as samples treated with 10 mL of 10% HCl and 15 mL of 30% H_2O_2 to remove carbonate and organic matter. The grain size distributions were used to calculate median, 10% and 90% grain size classes, and sand, silt, and clay-sized fractions.

Approximately 1 g of sediment was dried at 50 ° C, crushed and 10 mg subsamples were run using a Perkin Elmer 2400 Series CHNS/O Analyzer at the University of New Hampshire. Splits of untreated powder were used for total CHNS analysis and splits of 6% sulfurous acid-treated samples were run for TOC according to the procedures in Phillips et al. (2011). Duplicate samples were analyzed approximately every 10 samples. Inorganic carbon (IC) was calculated by the subtraction of TOC from total carbon (TC), and $CaCO_3$ was calculated by multiplying IC by 8.333. TOC/TN was calculated as TOC/TN = (TOC/12.011)/(TN.14.007).

A subset of powdered samples were analyzed for $\delta^{13}C$ of TOC ($\delta^{13}TOC$) at Washington State University using a Costech ECS 4010 elemental analyzer interfaced with a Thermo Finnegan Delta Plus XP continuous flow isotope ratio mass spectrometer. $\delta^{13}TOC$ results are presented relative to the Vienna Pee Dee belemnite (VPDB) in per mil (‰).

To complement existing rock magnetic datasets at Sites 1249 and 1252 (Larrasoaña et al., 2006, 2007), I measured mass-dependent magnetic susceptibility (χ) and isothermal remanent magnetism (IRM) in samples from Site U1325 in the Paleomagnetism Laboratory at the University of New Hampshire. Sediment samples were measured for χ using a Bartington MS2 Magnetic Suscepibility System. Samples were then cut into 1 cm^3 cubes, wrapped in foil, and subjected to stepwise acquisition of IRM with subsequent thermal demagnetization following the method of Lowrie (1990). IRM was acquired in steps from 0 to 1100 mT, with backfield magnetizations at -100 mT and -300 mT, using an ASC Scientific IM-10-30 Impulse Magnetizer. Remanent magnetizations were measured using an HSM2 SQUID-based Spinner Magnetometer. Thermal demagnetization was conducted in steps from 25 to 680 °C using an ASC Scientific TD-48 Thermal Demagnetizer.

Samples for rock magnetic analyses are typically sampled immediately after coring, sealed under nitrogen gas, and frozen until analysis. In this study, I attempted to measure magnetic properties on samples from cores stored at 4 °C and sealed under atmospheric conditions for approximately 8 years at the IODP Gulf Coast Repository since collection during IODP Expedition 311 in September 2005. Laboratory measured magnetic susceptibility was compared to shipboard measurements to confirm the lack of alteration of the magnetic mineral assemblage since core collection.

To identify intervals of altered magnetic susceptibility, I applied the method of Johnson et al. (in prep) to predict detrital κ using the relationship of a Zr/Rb magnetic mineral proxy at each site, quantified by regression analysis for best fit and 95% prediction intervals. Intervals in which there is a strong correlation between Zr/Rb and κ were used for regression analysis. At Site 1252 there is strong correlation between Zr/Rb and κ between 75 and 80 mbsf, that is assumed to represent an interval in which κ is unaltered by diagenesis. Additional XRF core scans between 0 and 13 mbsf at Site 1251 were combined in the Zr/Rb vs. κ regression analysis to strengthen the understanding of the κ-Zr/Rb relationship at Hydrate Ridge. At Site U1325 separate regressions were analyzed for the intervals 4.5-20 mbsf and 51 to 73 mbsf.

By subtraction of measured κ from predicted κ I estimate the loss of magnetic susceptibility. Based on the results of IRM analysis demonstrating magnetite as the dominant detrital remanence-carrying mineral, I used of a κ value of 1,000,000 x 10^{-6} SI for pseudo single domain (PSD) magnetite (Hunt et al., 1995) to estimate a minimum loss of magnetite content. The natural range of κ for pure magnetite is 1,000,000 to 5,700,000 x 10-6 SI (Hunt et al., 1995). This minimum value of PSD magnetite κ (0.001 mass fraction magnetite = 1,000 x 10^{6} SI) was used for calibration of ODP/IODP κ measurements (Blum 1997), including those from ODP Sites 1249 and 1252 and IODP Site U1325. Assuming dissolution of magnetite and complete reduction to pyrite, I calculate sulfur precipitation in wt. % based on a stoichiometric ratio of 1.12 mol of pyrite S produced for every 1 mol of magnetite iron reduced.

In preparation for samples to create an age model for the sediment records, 20 cm^3 of sediment were freeze dried at -48 °C and 0.006 kPa for 24 h, and dispersed in 1 L of 5 g/L sodium hexametaphosphate ($(NaPO_3)_6$) solution. The dispersed samples were shaken on a wrist-action shaker for 3 h and then sieved through 63 μm sieves. From this coarse fraction, benthic foraminifer species *Uvigerina peregrina, Uvigerina proboscidea, Bulimina mexicana,* and *Globobuliminia pacifica* were selected for $\delta^{18}O$ and $\delta^{13}C$ isotopic analysis.

Initial sampling focused on *Uvigerina peregrina* and were measured for $\delta^{18}O$ and $\delta^{13}C$ using a Finnegan MAT 252 isotope ratio mass spectrometer with Kiel III device at the Oregon State University Stable Isotope Laboratory. Due to intervals lacking *Uvigerina peregrina* or low general abundance of benthic foraminifers, additional samples of *Uvigerina spp., Bulimina mexicana, and Globobuliminia pacifica* were selected and measured using a Finnegan MAT 253 isotope ratio mass spectrometer with Kiel IV device at the University of Michigan Stable Isotope Laboratory.

Age models were developed using existing radiocarbon ages and benthic foraminifer oxygen isotopes (Johnson et al., 2010b), as well as new benthic formainifer isotopes. Ages from the oxygen isotope record were determined based on stacked benthic oxygen isotope records (Imbrie et al., 1984; Lisiecki and Raymo, 2005; Martinson et al., 1987). Sedimentation rates were determined by linear interpolation between ages. Mass accumulation rates (MAR) were calculated by the product of sedimentation rate and dry bulk density (Expedition 311 Scientists, 2006; Shipboard Scientific Party, 2003). MAR for TOC was calculation by multiplying the weight fraction TOC by the bulk MAR.

RESULTS

Grain size, Zr/Rb, Ti/Rb, and magnetic mineralogy

At Site 1249, median grain size varies between 8 and 12 μm, with coarser samples at 41.44 and 86.09 mbsf (13.5 and 18.1 μm respectively) (Fig. 2-3). Zr/Rb varies between 1.2 and

1.8, and Ti/Rb varies between 2.1 and 3.1 (Fig. 2-3). There is strong correlation between Zr/Rb and Ti/Rb, but little correlation between these proxies and median grain size. There is poor correlation between κ (Shipboard Scientific Party, 2003) and the XRF proxies. Measurements by Larrasoaña et al. (2006) demonstrate that much of the magnetic assemblage at Site 1249 is dominated by magnetite, with intervals of magnetic iron sulfide-dominant assemblages at 49.55, 69.93, and 86.01 mbsf.

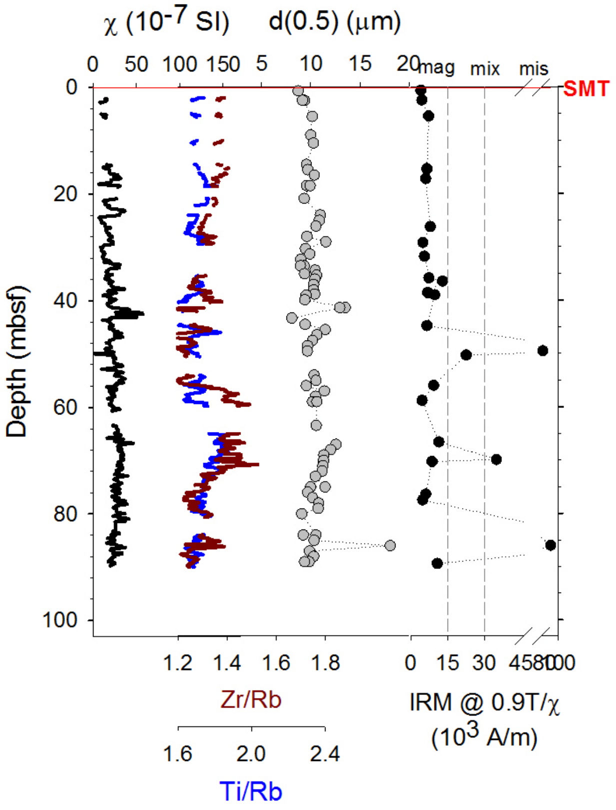

Figure 2-3. Magnetic susceptibility (κ), XRF Zr/Rb, XRF Ti/Rb, median grain size, and IRM @ 0.9/χ from ODP Holes 1249BCDF. κ from Shipboard Scientific Party (2003a) IRM from Larrasoaña et al. (2006).

At Site 1252, median grain size varies between 8 and 13 μm. Zr/Rb varies between 1.2 and 1.5, and Ti/Rb varies between 1.6 and 1.9 (Fig. 2-4). Similar to Site 1249, there is a strong correlation between Zr/Rb and Ti/Rb, but there is little correlation between these proxies and median grain size. For most of the record there is poor correlation between κ (Shipboard Scientific Party, 2003) and the XRF proxies, except between 75 and 80 mbsf. Previous work demonstrates that the magnetic assemblages at all depths at Site 1252 are dominated by magnetite (Larrasoaña et al., 2006).

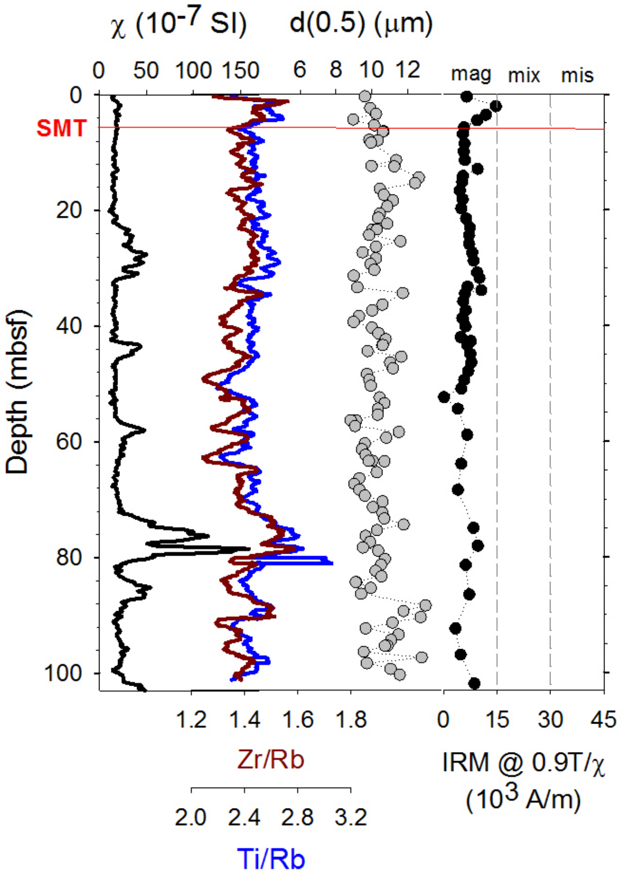

Figure 2-4. Magnetic susceptibility (κ), XRF Zr/Rb, XRF Ti/Rb, median grain size, and IRM @ 0.9/χ from ODP Hole 1252A. κ from Expedition 311 Scientists (2006).

In the upper 26 m of Site U1325, median grain size varies from 10 to 113 μm, with a consistently finer interval (9 to 17 μm median grain size) between 26 and 81 mbsf (Fig. 2-5). At

83.5 and 86.2 mbsf median grain size increases to 22.5 and 21.4 µm respectively. In the upper 20.2 mbsf at Site U1325, Zr/Rb exhibits the largest variability ranging from 1.0 to 8.6 (Fig. 2-5). Between 24 and 52.5 mbsf, Zr/Rb is less variable, ranging between 0.9 and 3.8. Zr/Rb increases in the interval between 54 and 73 mbsf, ranging between 1.1 and 5.9. Ti/Rb displays a down core pattern similar to Zr/Rb. Ti/Rb varies between 1.9 and 6.6 in the upper 20 mbsf, between 1.4 and 3.0 in the 24-52.5 mbsf interval, and 1.5 and 3.6 in the interval 54-73 mbsf. There is a strong correlation between κ and Zr/Rb and Ti/Rb proxies between 4.5 and 20 mbsf, and between 51 and 74 mbsf. IRM measurements indicate that magnetite dominates the magnetic mineral assemblage throughout most of the record at Site U1325, with samples of mixed magnetite and magnetic iron sulfides at 43.10, 66.60, and 75.32 mbsf (Fig. 2-5). Magnetic iron sulfides may have been altered via sulfide mineral oxidation during 7 years of exposure to oxygen during core storage. Sulfide mineral oxidation occurs at high rates (2-5 kg m^{-2} yr^{-1}) (Kempton and Atkins, 2009) in rock surfaces containing less than 1 wt.% S, and visual inspection of U1325 cores showed oxidation of iron sulfide nodules. Comparison of shipboard and sampled laboratory magnetic susceptibility indicates no appreciable deviation between dataset (Fig. 2-6) measurements made immediately after coring and samples collected after years of storage. Magnetic iron sulfides were likely a minimal contributor to the magnetic susceptibility pattern observed at Site U1325.

Relationship of Zr/Rb and magnetic susceptibility

Using observed intervals in Sites 1252 (with additional data from Site 1251) and Site U1325, where there is good correlation between Zr/Rb and κ, I used regression analysis to predict best fit, and 95% prediction intervals. At Sites 1252/1251, there is an overall linear relationship between Zr/Rb (ranging from 1.3 to 1.8) and κ (ranging from 15 to 211 SI x 10^{-7})

with an r^2 value of 0.76 (Fig. 2-7). At Site U1325, regression for the intervals 4.59-18.80 mbsf and 51-73 mbsf show a wider range in Zr/Rb and κ than at Site 1252, and are best fit by a logarithmic function. In the range of Zr/Rb<2, the overall fit is linear. Between 4.59 and 18.80 mbsf, Zr/Rb varies from 1.0 to 8.6 and κ varies from 46.4 to 315 SI x 10^{-7}.

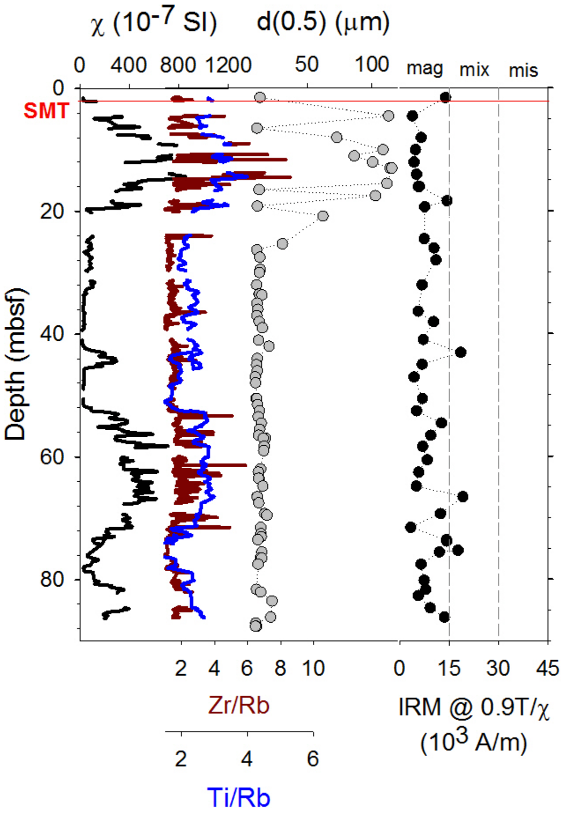

Figure 2-5. Magnetic susceptibility (κ), XRF Zr/Rb, XRF Ti/Rb, median grain size, and IRM @ 0.9/χ from ODP Hole U1325B.

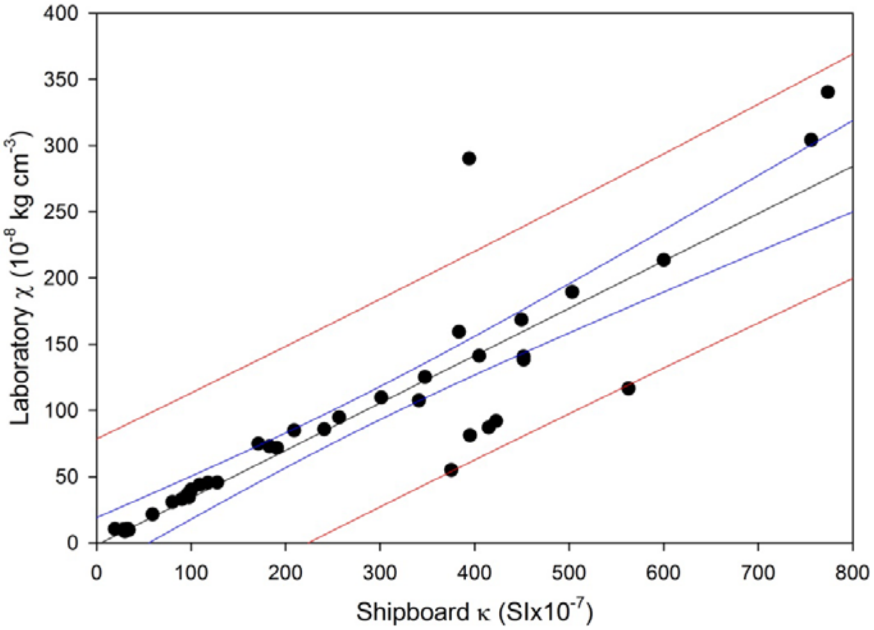

Fig. 2-6. Comparison of volume-dependent magnetic susceptibility (κ) at Site U1325 measured shipboard on the *D/V JOIDES Resolution* during 2005 and discrete samples measured for mass-dependent magnetic susceptibility (χ) at the UNH Paleomagnetism Laboratory in 2012. The overall correlation indicates relatively little alteration to the magnetic mineral assemblage during storage.

Drawdowns in magnetic susceptibility

At Site 1249, predicted detrital κ is significantly higher than measured κ for much of the record (demonstrated by 95% prediction intervals), except for the intervals 34.5-54.4 mbsf and 65.1-88.0 msbf (Fig. 2-8). Actual κ varies from 2.0 to 44.3 SI x 10^{-7} (mean: 25.0), while best-fit predicted κ varies from 5.7 to 114.5 SI x 10^{-7} (mean: 49.3). Intervals in which predicted κ is not higher than actual κ have samples that the magnetic mineral assemblage is magnetic sulfide dominant (Larrasoaña et al., 2006). The resulting loss of κ up to 63 SI x 10^{-7} is predicted in the upper 29 mbsf and up to 84 SI x 10^{-7} in the interval between 54 and 75 mbsf. This loss of κ corresponds to dissolution of up to 0.8 wt. % magnetite, and precipitation of up to 0.7 wt. % S. Measured S varies from 0.11 to 0.7 wt. %. Fe/κ is relatively consistent over the upper 49 mbsf, and below a peak at 50 mbsf, Fe/κ decreases and is more variable between 50 and 88 mbsf. TOC falls in the range of 0.80 to 1.76 wt%, and XRF-measured Br correlates to the downcore pattern in TOC. TOC/TN varies between 6.6 and 10.2 and δ^{13}TOC varies from -23.3 to -22.8 ‰ VPDB.

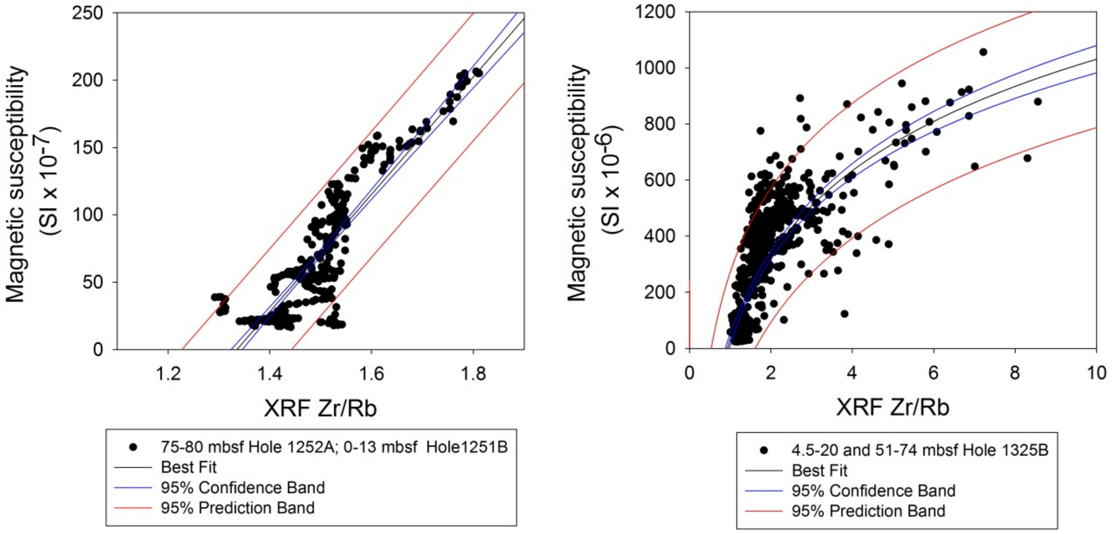

Figure 2-7. Relationship of XRF Zr/Rb and magnetic susceptibility at Sites 1252A/1251B (left panel) and U1325B (right panel). The correlation of Zr/Rb and magnetic susceptibility is best described as linear at the southern Hydrate Ridge sites, and logarithmic at Site U1325. The portion of the relationship of Zr/Rb and magnetic susceptibility is linear for the portion of U1325 where Zr/Rb is less than 2.

At Site 1252, predicted κ is higher than measured for most of the upper 100 mbsf except for the interval 75-78 mbsf (Fig. 2-9). Actual κ varies from 10.9 to 158.8 SI x 10^{-7} (mean: 26.4) while best-fit predicted κ varies from 22.3 to 141.7 SI x 10^{-7} (mean: 72.8). The intervals with the highest predicted loss of κ and magnetite are 0-28.8, 31.8-41.7, 45.3-54.4, 58.5-70.9, and 78.2-101.3 mbsf. In these intervals, average predicted κ loss and magnetite loss is 48.6 SI x 10^{-7} and 0.49 wt% respectively. Average predicted precipitated S gain in these intervals is 0.39 wt. %. Overall, measured S matches the downcore pattern in predicted S, with a notable mismatch between 45 and 52 mbsf. Mean measured S is 0.42 wt. %, varying from 0.29 to 0.72 wt. %. Normalized Fe/κ increases distinctly in the intervals of highest predicted loss of magnetite (Fig.

2-9). TOC is relatively high with a mean of 1.53 wt. % and variable, ranging from 1.05 to 2.18 wt. %. Increases in TOC occur in the intervals with highest magnetite loss and S gain. Average TOC/TN is 8.8 and increase in intervals of elevated TOC. δ^{13}TOC varies from -23.8 to -22.3 becoming less depleted in higher TOC intervals.

At Site U1325, predicted κ matches measured κ closely in the upper 20 mbsf and between 54-73 msbf (Fig. 2-10). Predicted detrital κ is significantly higher than measured κ over the intervals 24.2-43.7 and 44.1-51.4 mbsf. Likewise, there is average κ loss of 154.7 SI x10-7 and 1.5 wt. % average magnetite loss over this interval. Best fit S precipitation gain on average is 1.25 wt. % over the interval of κ loss, while average measured S is 0.39 wt. %, with the overall pattern of measured S following predicted S. Fe/κ is elevated from 1.5-2.1, 24.5- 57.2, and 69.3-76.8 mbsf. TOC is highly variable downcore, ranging from 0.07 to 1.73 wt. %. Distinct increases in TOC occur in the upper 10, 15-43, and 71-79 mbsf. Increases in TOC match decreases in TOC/TN and increases in δ^{13}TOC (Kim and Lee, 2009).

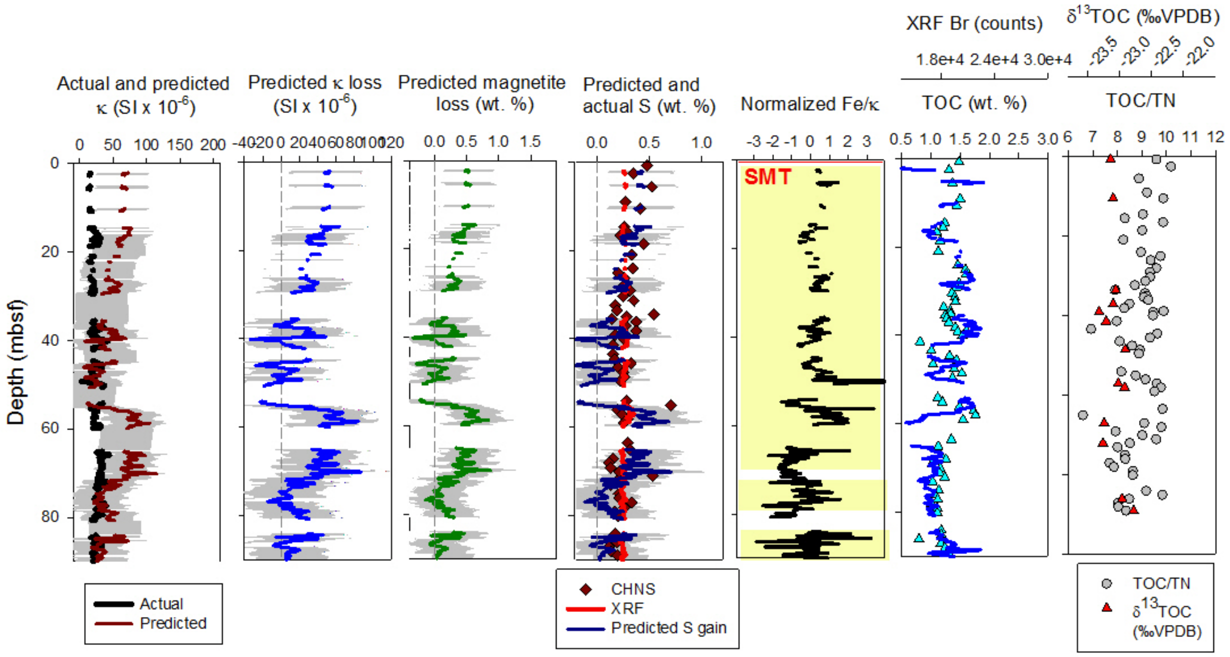

Figure 2-8. Actual and predicted κ, predicted diagenetic loss of κ, predicted magnetite loss, predicted and actual sulfur precipitation, normalized Fe/κ, TOC with XRF Br, and δ^{13}TOC with TOC/TN at ODP Site 1249.

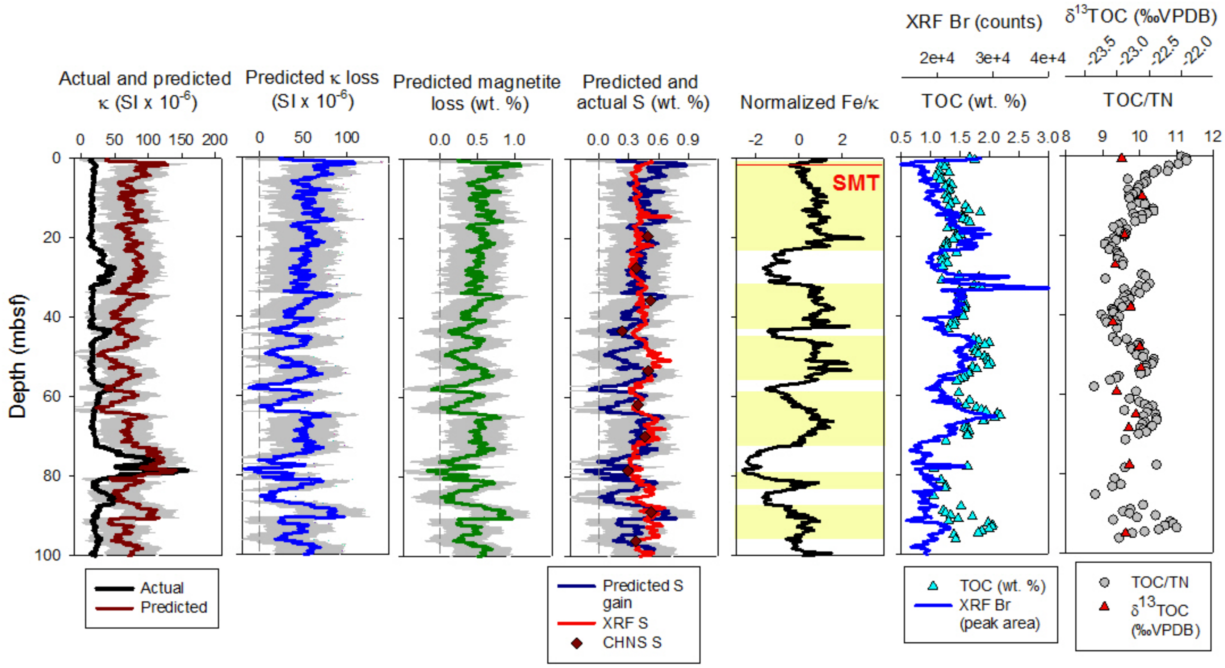

Figure 2-9. Actual and predicted κ, predicted diagenetic loss of κ, predicted magnetite loss, predicted and actual sulfur precipitation, normalized Fe/κ, TOC with XRF Br, and δ^{13}TOC with TOC/TN at ODP Site 1252.

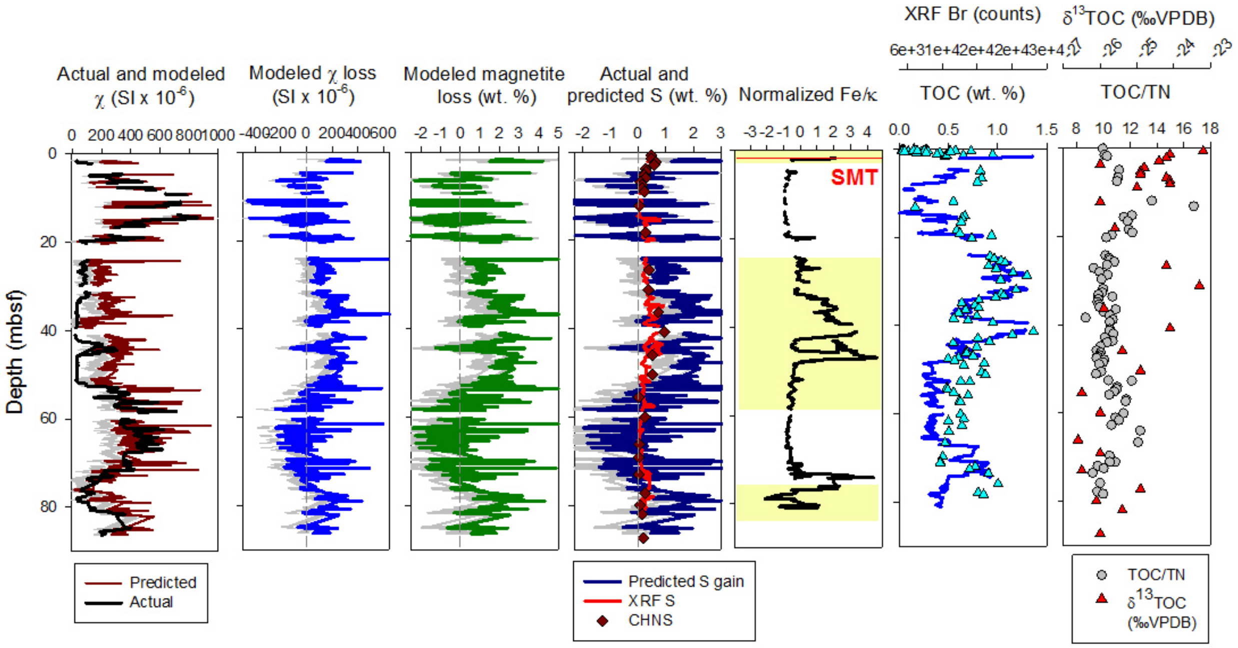

Figure 2-10. Actual and predicted κ, predicted diagenetic loss of κ, predicted magnetite loss, predicted and actual sulfur precipitation, normalized Fe/κ, TOC with XRF Br, and δ^{13}TOC with TOC/TN at ODP Site U1325.

Age Models

At Site 1249, foraminifers were not present in sufficient abundance for radiocarbon, and the age model is derived from oxygen-isotope stratigraphy only. Sediments at Site 1249 range in age from 18 ka at 10.6 mbsf to 175 ka at 79.11 mbsf, with an average sedimentation rate of 57 cm/kyr (Fig. 2-11, 2-12). Based on combined radiocarbon and oxygen isotope stratigraphy, the age of Site 1252 sediments ranges from 13.7 ka at 0.25 cm to 123 ka at 96.18 mbsf with an average sedimentation rate of 80 cm/kyr (Fig. 2-11, 2-12). At Site U1325, sediment age ranges from 10.5 ka at 1.82 mbsf to 99 ka at 76.61 mbsf, with an average sedimentation rate of 86 cm/kyr (Fig. 2-11, 2-12).

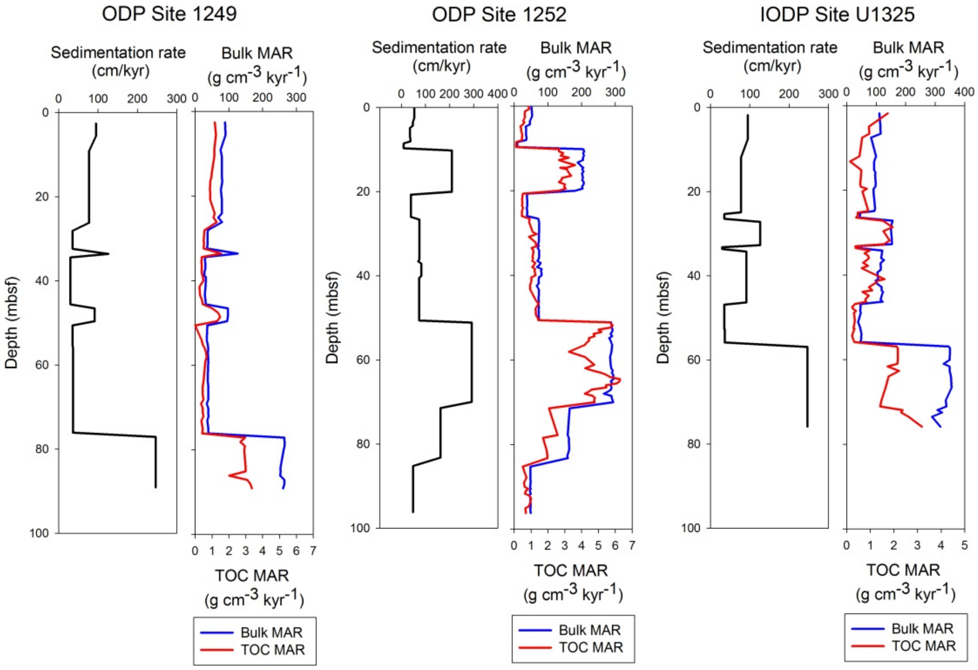

Figure 2-11. Sedimentation rates and mass accumulation rates (bulk and TOC) at ODP Sites 1249 and 1252; IODP Site U1325. Vertical depth scale.

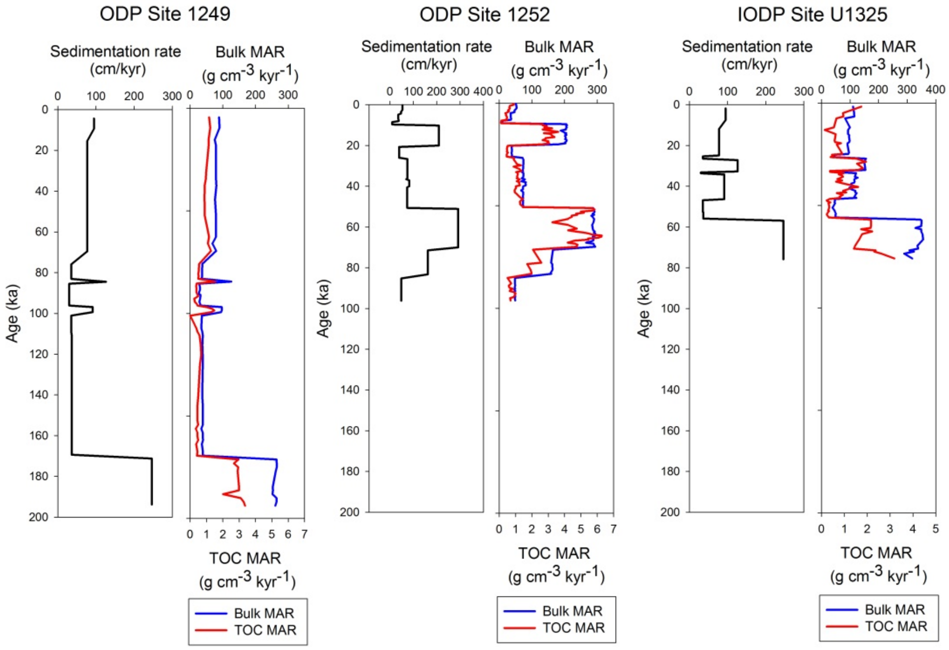

Figure 2-12. Sedimentation rates and mass accumulation rates (bulk and TOC) at ODP Sites 1249 and 1252; IODP Site U1325. Vertical age scale

Table 2-1: Radiocarbon ages and benthic oxygen isotope events for ODP Sites 1249 and 1252; IODP Site U1325. Radiocarbon data from Johnson et al., 2010a.

ODP Site 1249			ODP Site 1252			IODP Site U1325		
Depth (mbsf)	Age (ka)	OIE	Depth (mbsf)	Age (ka)	OIE	Depth (mbsf)	Age (ka)	OIE
10.6	17.85	LGM	0.25	13.694	RC	1.82	10.543	RC
29.11	79.25	5.1	2.47	17.85	LGM	7.92	16.992	RC
39.15	90.95	5.2	2.49	19.527	RC	24.91	38.978	RC
49.61	99.38	5.3	3.03	20.677	RC	26.46	43.369	RC
56.11	110.7	5.4	4.33	24.328	RC	33.18	48.693	RC
58.8	123.8	5.5	6.97	31.433	3.13	33.63	50.2	3.3
67.11	152.5	6.4	8.815	34.894	RC	46.32	64.09	4.22
79.11	175.05	6.5	9.68	43.8	RC	51.61	79.25	5.1
			20.05	48.754	RC	55.85	90.95	5.2
			26.03	64.09	4.2	76.61	99.38	5.3
			36.18	77.67	RC			
			36.57	79.25	5.1			
			40.8	84.39	RC			
			70.72	90.95	5.2			
			84.39	99.38	5.3			
			96.18	123.8	5.5			

RC: radiocarbon age

OIE: Oxygen-isotope event

LGM: Last Glacial Maximum

DISCUSSION

Approach Limitations

The prediction of primary detrital patterns in κ are necessary to be able to identify intervals of alteration. Before discussing diagenetic drawdowns in κ, the limitations of this method that were encountered during this work should be considered. The first limitation to using Zr/Rb as a heavy mineral proxy to predict magnetic susceptibility is identification of intervals of original, unaltered κ that can be measured with XRF core scanning for Zr and Rb and used to establish a relationship between Zr/Rb and κ. Unaltered intervals, or nearby reference sites, in which κ matches the record of Zr/Rb are necessary to establish the relationship used to predict the detrital κ pattern. Thus, without the lower flux Sites 1252, 1251, and U1325, I would be unable to predict κ and estimate loss of magnetite at Site 1249, in which κ appears to be entirely overprinted. The relationship between κ and Zr/Rb is consistent between the Hydrate Ridge Sites 1251/1252 and Northern Cascadia Site U1325 (Fig. 2-7); however, this relationship likely is influenced by the mineralogical composition of the heavy mineral fraction (e.g. relative content of zircon vs. magnetite) and varies between region. Fig 2-13 shows the relationship between Zr/Rb and κ at these Cascadia margin sites and previously published work from the Bay of Bengal (Phillips et al., 2014; Johnson et al., in prep).

A second limitation is the dominant mineralogy used to estimate the amount of magnetic mineral loss. At these Cascadia margin sites, detrital mineralogy is dominantly magnetite (Larrasoaña et al., 2006), allowing for a straightforward relationship between κ and magnetite content (Hunt et al., 1995). With a complete pyritization of magnetite (e.g. Canfield and Berner, 1987), a clear decrease in κ would be observed (e.g. Novosel et al., 2005; Riedinger et al., 2005). However, in the case that intermediate ferrimagnetic iron sulfide minerals, such as greigite or pyrrhotite are formed after dissolution of magnetite (e.g. Housen and Musgrave, 1996; Larrasoaña et al., 2007; Musgrave et al., 2006), κ could be increased, maintained, or otherwise only minimally decreased compared to the complete reaction to paramagnetic pyrite. At Site 1249, between 34.5-54.4 and 65.1-88.0 msbf predicted detrital κ and measured κ are not significantly different, yet there is no correlation between κ and Zr/Rb. In this case, the presence of magnetic iron sulfides in these intervals (Fig. 2-3) (Larrasoaña et al., 2006) suggests that κ is higher than predicted given an assumption of complete reaction of magnetite to pyrite. At sites where a variety of depositional processes (fluvial, eolian, ice-rafted debris, volcanogenic) result in sediment records in which κ is strongly influenced by hematite and/or goethite content in addition to magnetite (e.g. Bloemendal et al., 1992;1993), additional quantification of magnetic mineral assemblage would be necessary.

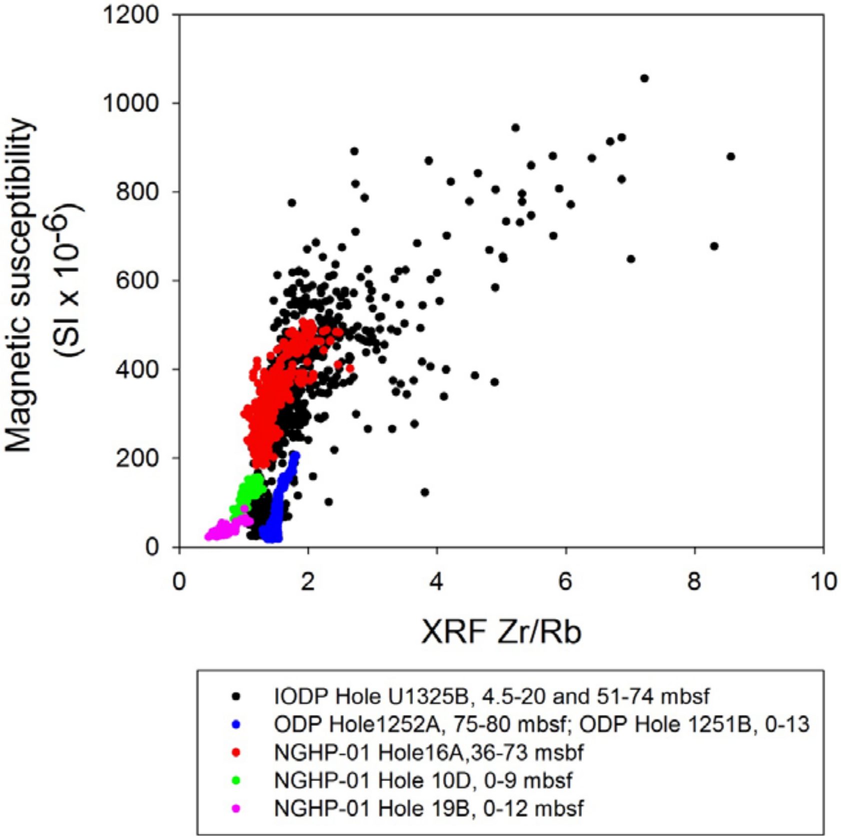

Figure 2-13: Relationship of XRF Zr/Rb and magnetic susceptibility at ODP Sites 1251/1252, IODP Site U1325, and NGHP Sites 10/16/19 (Phillips et al., 2014; Johnson et al., in prep). The overall trends are consistent across sites but slightly offset.

A third limitation demonstrated by the record in the upper 20 m of Site U1325 is the relationship of Zr/Rb and κ, and the relationship between κ and magnetite content in coarse sediments. Despite a consistent detrital magnetic mineral assemblage of magnetite, the linear relationship of Zr/Rb and κ becomes logarithmic and the correlation weakens above Zr/Rb of 2 (Fig. 2-7). In this case, Zr/Rb generally corresponds to a median grain size of greater than 20 µm (Fig. 2-14). This suggests either (1) a possible increased variability and/or decreased content of heavy mineral composition in coarse, graded sediments derived from turbidity currents, (2) the increased prevalence of multi-domain magnetite relative to single-domain or pseudo-single domain magnetite, or (3) non-linearity in the XRF response at low Rb values. In turbidites and other mass-transfer deposits, high-energy transport of sand-sized quartz and lithic grains may dilute magnetite content compared to the clay/fine silt hemipelagic mud. Additionally, variable sorting may result in an inconsistent relationship between zircon (driver of the Zr/Rb signal) and magnetite (driver of the κ signal) in these intervals. The presence of sand-sized, lithic grains may contain larger multi-domain magnetite which may have a decreased and variable κ response due to cancellation of magnetic moments in adjacent domains. In comparing the Zr/Rb versus κ relationship in samples that were measured for grain size distribution, samples in which the median grain size is greater than 50 µm contribute most strongly to the logarithmic pattern (Fig. 2-15). Another possible contributor to this variation is the sharp increase in Zr/Rb at the lowest range of Rb peak areas measured by XRF (Fig 2-16). However, a potential nonlinear decrease in the X-ray response of Rb at a low range would cause an increase in Zr/Rb and would not contribute to a logarithmic response of magnetic susceptibility. Further work to investigate the non-linear relationship at Site U1325 should include independent, fully-quantitative measurements of Rb, rock magnetic analyses indicative of magnetic grain size, and heavy mineral analyses of zircon and magnetite to better understand the relationship of Zr/Rb and κ.

Diagenetic Source of Magnetic Suscepbiliity Drawdowns

After establishing the limitations of the method, I can then interpret the source of the drawdowns of κ in these records as the diagenetic dissolution of magnetite in the presence of H_2S and precipitation of sulfides. Although some intervals are likely influenced by the presence of greigite or pyrrhotite, the magnetite-dominant assemblages suggest that magnetic susceptibility loss is mostly balanced by precipitation of pyrite. Because marine organic matter has an S/C ratio of approximately 0.02 (Suits and Arthur, 2000), the direct contribution of sulfur from organic matter is between <0.01 and 0.03 wt. % in sediment samples from these sites. Mean TS at these Sites 1249, 1252, and U1325 are 0.26, 0.42, and 0.30 respectively, suggesting that the vast majority of TS is derived from post-depositional precipitation.

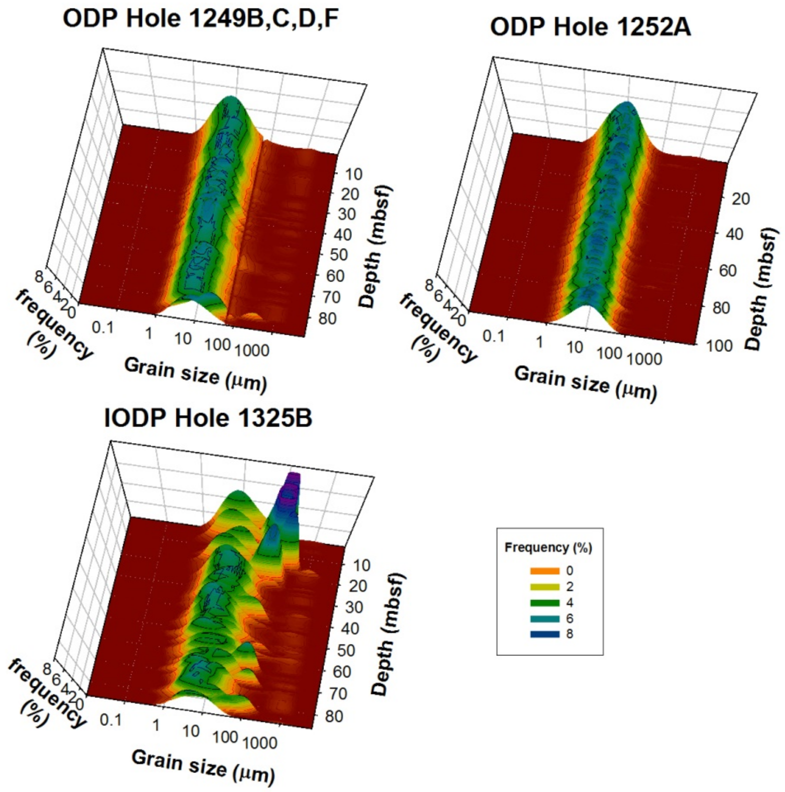

Figure 2-14. Summary of grain size distribution at ODP Sites 1249 and 1252, and IODP Site U1325. Grain size distributions are more variable and coarser at Site U1325.

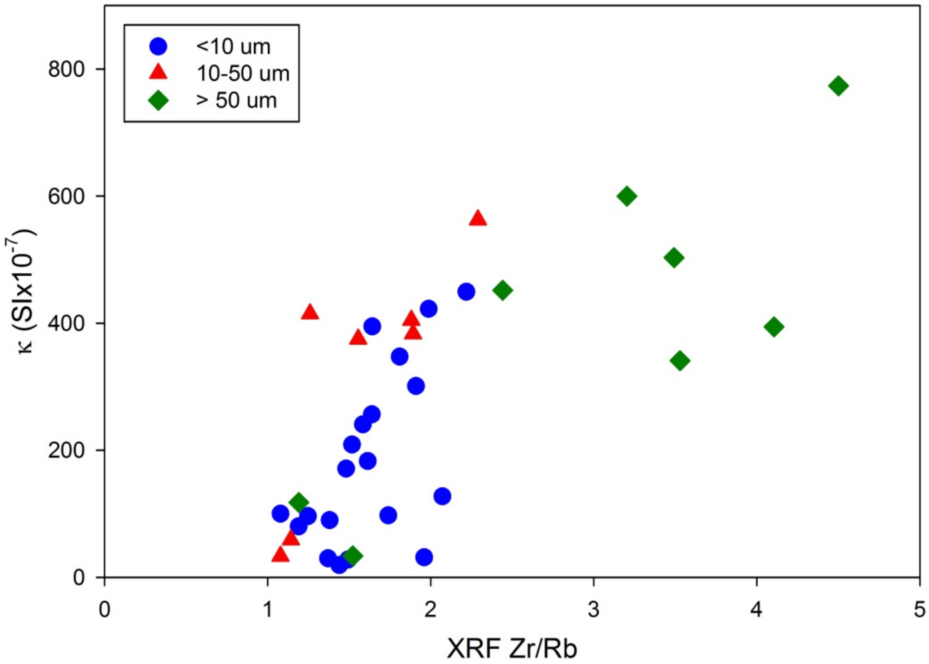

Fig. 2-15. XRF Zr/Rb versus κ segregated by median grain size (<10 µm, 10-50 µm and >50 µm) at IODP U1325. The nonlinearity in the Zr/Rb and κ is driven largely by coarse-grained samples with median grain size greater than 50 µm.

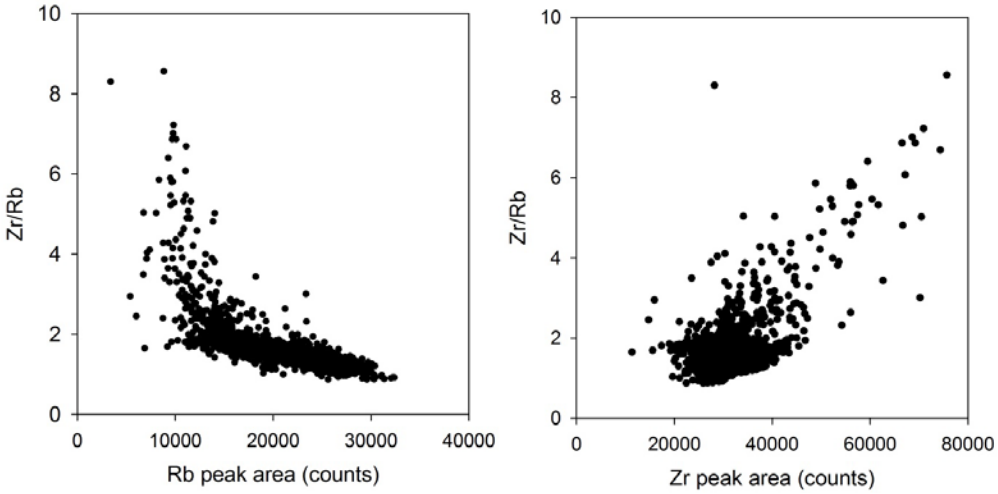

Fig. 2-16. XRF Zr/Rb versus XRF Rb peak areas (left) and XRF Zr/Rb versus Zr peak areas (left) at IODP Site U1325. A sharp increase in Zr/Rb at the low range of Rb suggests a possible nonlinear decrease in Rb response at low values.

At all three sites there are distinct intervals in which κ is less than predicted, while TS and Fe/κ is elevated (Fig. 2-8, 2-9, and 2-10). This relationship demonstrates that magnetite loss is balanced by sulfur gain that suggests precipitation by pyrite, thus replacing a ferromagnetic mineral with paramagnetic mineral. Measured TS falls within the range of pyrite S gain predicted from κ dissolution. Possible mechanisms include AOM or organoclastic sulfate reduction due to the production of H_2S that can react with iron oxides to produce iron sulfides.

At Sites 1252 and U1325 there is a strong correlation of TOC with κ loss, TS, and Fe/κ (Fig. 2-9 and 2-10), which may suggest an increased intensity of organoclastic sulfate reduction and dissolution of magnetite in these intervals. Additionally, sediments with low TOC have been observed to have enhanced methane oxidation capacity (Pohlman et al., 2013), thus records such as Sites 1252 and U1325 which experience fluctuations in TOC greater than 1 wt. % may experience variations in depths of the SMT and rates of AOM due to variable TOC availability. The intervals of κ loss may represent past prolonged positions of the SMT.

At Site 1249, there is little to no correlation between TOC and κ loss, TS, and Fe/κ. Because Site 1249 is a methane vent site located on the ridge, with observed gas hydrate (Shipboard Scientific Party, 1993) the reduced κ is likely due to sustained high methane flux and AOM (e.g. Novosel et al., 2005). This record indicates intervals of magnetic susceptibility loss and sustained or increased κ due to magnetic iron sulfides (Larrasoaña et al., 2006).

Sedimentation rate influences the exposure time of magnetite in the sulfidic zone, potentially stalling or accelerating SMT migration (e.g. Riedinger et al., 2005). Decreases in sedimentation rate may explain the reductions in κ observed in IODP Site U1325. Based on age models from radiocarbon and oxygen-isotope stratigraphy, there is a sharp decrease in sedimentation rate from ~250 cm/kyr to <100 cm/kyr. This decrease in sedimentation rate may have resulted in the increased time of exposure for magnetite during upward SMT migration, potentially causing the diagenetic loss of κ between 21 and 55 mbsf. However, the correlation between increased TOC and diagenetic drawdown of κ, may suggest the role of SR rather than prolonged position of the SMT. The decrease in sedimentation rate at IODP Site U1325 may be related to the increase in TOC by decreasing the amount of dilution by the lithogenic fraction. At ODP Site 1249 and 1252 age models show that changes in sedimentation rate are generally independent from intervals of diagenetic loss of κ, suggesting that SMT migration is not a likely driver of magnetite dissolution. Some intervals of reduced κ at Site 1252 exist during periods of high sedimentation rate, which is not consistent with a stalling SMT but possibly with periods of increased TOC burial, which can in turn drive SR and methanogenesis.

As a result of sulfate reduction, modern marine sediments exhibit an average C:S ratio of approximately 3:1 when limited by organic carbon (Berner, 1982; Berner and Raiswell, 1983), and deviation from this trend suggests either additional iron sulfide precipitation from AOM or advective loss of H_2S (Kaneko et al., 2010). I compare the TOC:TS ratio from Sites 1249, 1252, and U1325 relative to the global average trend in Fig. 2-17. At Site 1249, TOC:TS is generally higher than this trend, likely due to the sulfur-limited environment of sediments below a methane seep, in which sulfate is depleted at the sea floor, resulting in lower TS relative to TOC. Instead of reacting to form iron sulfide minerals, H_2S at seep sites can be vented to the overlying water column (Kuwubara et al., 1999). At Site 1252, TOC:TS generally matches the global trend, suggesting a substantial role of sulfate reduction in precipitation of sulfur at this site. At Site U1325, most samples follow the global trend with several high-sulfur samples with a substantially lower TOC:TS, indicating the possibility of additional sulfide precipitation from AOM.

While our method clearly shows the alteration of magnetite by decreased κ and increased TS, identifying the specific biogeochemical processes responsible for these observations can be better identified via further work involving reactive transport modeling or by tracking other SMT-related proxies. Reactive transport models incorporating the dissolution of magnetite by reaction to H_2S and sedimentation rate might illuminate the role of organoclastic sulfate reduction or AOM in influencing these κ records. Measurement of $\delta^{34}S$ of pyrite as a proxy of sulfur limitation (Peketi et al., 2012; Borowski et al., 2013) would likely indicate whether sulfide-rich, reduced κ intervals are a result of near-seafloor organoclastic sulfate reduction or AOM at the SMT.

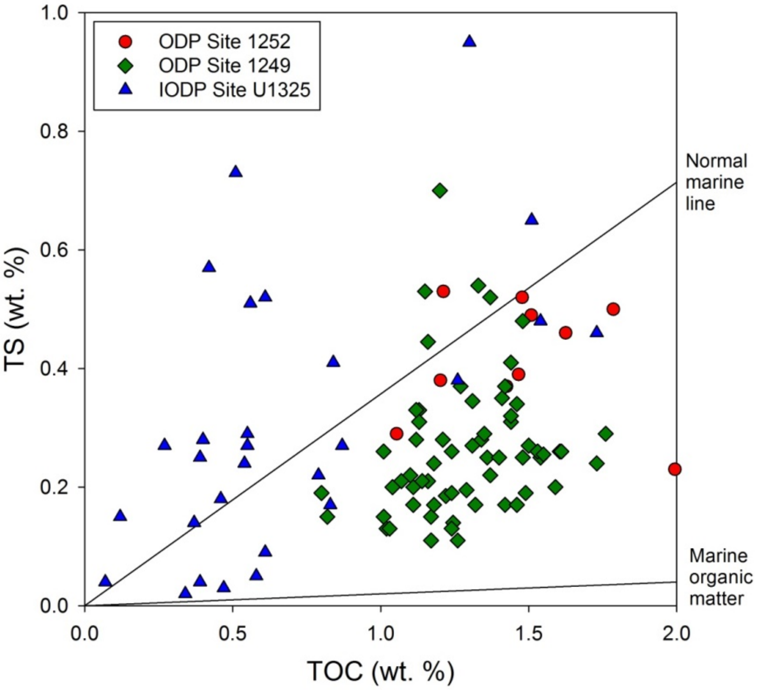

Figure 2-17. Total organic carbon versus total sulfur for ODP Sites 1249 and 1252; IODP Site U1325. Normal marine line (S derived from sulfate reduction) from Berner and Raiswell (1983) and marine TOC sulfur contribution from Suits and Arthur (2000).

CONCLUSION

I identify intervals of reduced κ using a Zr/Rb heavy mineral proxy from XRF. These intervals correspond to increases in TS and Fe/κ indicating the pyritization of magnetite due to reaction with hydrogen sulfide. I identify three limitations to guide the application of this approach: (1) the presence of unaltered intervals in which κ is dominantly of detrital origin must be present so that Zr/Rb can be calibrated with κ, (2) the magnetic mineral assemblage must be dominated by magnetite for the assumptions of pyritization to be valid, and (3) the presence of fine-grained sediments in which the magnetic signal is carried by SD or PSD magnetite, rather than multi-domain magnetite.

3. A SHIFT IN TITANOMAGNETITE COMPOSITION ASSOCIATED WITH DEEPLY BURIED COAL BEDS AS RESULT OF MICROBIAL IRON REDUCTION, OFFSHORE SHIMOKITA PENINSULA, JAPAN (IODP HOLE C0020A)

ABSTRACT

Sediments recovered at Integrated Ocean Drilling Program (IODP) Site C0020, in a forearc basin offshore Shimokita Peninsula, Japan, reveal a record of changes in the depositional environment encompassing a terrestrial-to-marine transition that includes numerous coal beds. Within a coal-bearing, nearshore sediment unit there are sharp increases in magnetic susceptibility superimposed on a background of consistently low magnetic susceptibility throughout the remainder of the recovered cores. I investigate the source of this magnetic susceptibility variability, as well as the overall changes in magnetic mineral assemblage throughout the entire record, using isothermal remanent magnetism (IRM) and demagnetization experiments. The magnetic mineral assemblage is dominated by very low-coercivity minerals with an unblocking temperature of 350-580°C, representing the titanomagnetite series. Samples with lower unblocking temperatures (350-400°C) are prevalent between 1925-1975 mbsf and 1979-1995 mbsf within sediments deposited in a nearshore depositional environment and consistent with Ti-rich titanomagnetite. I suggest that the selective dissolution of Ti-poor, Fe^{3+}-rich titanomagnetite via microbial iron reduction, has resulted in Ti-rich, Fe^{3+}-poor titanomagnetite as the remaining dominant magnetic mineral observed within these sediments. The anomalous increases in magnetic susceptibility within this nearshore unit are often associated with black sand laminations, which suggest hydraulic sorting, possibly in a placer deposit. The enrichment of titanomagnetite within this depositional environment adjacent to the

deeply buried coalbeds suggests the availability of Fe^{3+} as an electron acceptor for the deep biosphere regardless of the source.

INTRODUCTION

Rock magnetic techniques can reveal magnetic mineral properties that facilitate interpretation of depositional and/or diagenetic mineral processes in sediments and sedimentary rocks (Liu et al., 2012; Verosub and Roberts, 1995). Ferrimagnetic (magnetite-titanomagntite) and canted antiferrimagnetic (hematite, goethite) iron oxides can be transported to marine sediments via fluvial (e.g., Canfield, 1997), eolian (e.g. Robinson, 1986; Bloemendal et al., 1993; Mahowald et al., 2005; Fan et al., 2006), and ice-rafted debris transport (e.g. Hall and King, 1989; Richter et al., 2001). Titanomagnetite minerals have a composition that exists along a solid solution series between magnetite (Fe_3O_4) and ulvöspinel (Fe_2TiO_4) as end members. Magnetite can also be produced by magnetotactic bacteria in deep marine and coastal environments (e.g. Kirschvink and Chang, 1984; Karlin et al., 1987; Roberts et al., 2011). Magnetic iron oxides are subject to dissolution and precipitation of pyrite in anoxic sediments (e.g. Canfield and Berner, 1987; Karlin, 1990; Canfield et al., 1992; Poulton et al., 2004; Garming et al., 2005; Riedinger et al., 2005). In addition, Greigite (Fe_3S_4) and pyrrhotite ($Fe_{1-x}S_{0 < x < 0.13}$) are ferrimagnetic iron sulfides that form as an intermediate step of pyrite formation in anoxic environments (e.g. Sweeney and Kaplan, 1973; Furukawa and Barnes, 1995; Neretin et al., 2004), and are generally indicative of sulfur-limiting conditions, such as those present in gas hydrate-bearing settings (e.g. Housen and Musgrave, 1996; Larrasoaña et al., 2006, 2007; Musgrave et al., 2006; Fu et al., 2008; Kars et al., 2015). Often, marine sediment records reveal multiple detrital magnetic mineral sources and diagenetic processes that affect the magnetic mineral assemblage (e.g. Just et al., 2012).

Magnetic ferric iron oxides, such as hematite (1) , goethite (2), and magnetite (3), may directly serve as a source of Fe^{3+} electron acceptors for iron-reducing bacteria (e.g. Arnold et al., 1988; Lovely, 1991; Kostka and Nealson, 1995), shown below as energetically favorable reactions (Lovely, 1991):

$$12Fe_2O_3 + C_6H_{12}O_6 + 42H^+ \rightarrow 24Fe^{2+} + 6HCO_3^- + 24H_2O \qquad (1)$$

$$\Delta G° = -1276.38 \text{ kJ/mol}$$

$$24FeOOH + C_6H_{12}O_6 + 42H^+ \rightarrow 24Fe^{2+} + 6HCO_3^- + 36H_2O \qquad (2)$$

$$\Delta G° = -1308.54 \text{ kJ/mol}$$

$$12Fe_3O_4 + C_6H_{12}O_6 + 66H^+ \rightarrow 36Fe^{2+} + 6HCO_3^- + 36H_2O \qquad (3)$$

$$\Delta G° = -1872.95 \text{ kJ/mol}$$

As a result of these reactions, magnetic iron oxides are dissolved and Fe^{2+} is produced along with bicarbonate. When insufficient dissolved hydrogen sulfide is available to consume the free Fe^{2+} as iron sulfides, the Fe^{2+} is available to form siderite (Pye et al., 1990). Based on Gibbs free energy, the reduction of magnetite is the most favorable reaction.

Magnetic mineral diagenesis can be influenced by depositional setting. In marine environments, the diffusion of seawater sulfate into near-seafloor sediments serves as an electron acceptor for sulfate reduction, and increases the potential for formation of pyrite and/or greigite. In marine environments iron oxides are consumed by microbial iron reduction and reaction with hydrogen sulfide at approximately equal rates. In freshwater environments, there is reduced sulfate availability, but microbial magnetite reduction, using Fe^{3+} as an electron acceptor, is optimal at pH 5 to 6 (Kostka and Nealson, 1995), in a typical range for terrestrial freshwater.

In this study. I use rock magnetic approaches to identify ferrimagnetic mineral phases within a deeply buried (1.2 to 2.5 km) interval of sediment recovered in an ocean drilling record

(IODP Hole C0020A) in the Hidaka Trough offshore Shimokita Peninsula, Japan. Within this record, I utilize characteristic magnetic susceptibility, coercivity, and unblocking temperature properties to identify significant magnetic mineral assemblages, and discuss their relevance to the depositional environment and evaluate their potential role in iron and carbon cycling within the deep biosphere at this site (Inagaki et al., 2015) associated with the subsurface coal beds.

GEOLOGICAL SETTING

Site C0020A (Fig. 3-1) is located in a forearc basin formed as a result of the subduction of the Pacific plate beneath northeast Honshu (Von Huene, et al., 1982; Sacks and Suyehiro, 2003). Forearc subsidence offshore Shimokita has been occurring since the Cretaceous, and through time the interaction between subsidence and eustatic sea level change has modulated the depositional environment. The late Oligocene to early Miocene sediments within the basin record a broad transition in the depositional environment from a terrestrial to marginal marine dominated (Von Huene et al, 1982) and the sediments from the Neogene to present represent a marginal marine to open marine transition. Previous drilling during Deep Sea Drilling Project (DSDP) Legs 56, 57, and 58 and Ocean Drilling Program (ODP) Leg 186 along the Japan Trench offshore northern Honshu (seaward of IODP Site C0020A) revealed Cretaceous to Holocene sediments primarily composed of hemipelagic clay, turbidities containing lithic fragments, siliceous/calcareous microfossils, and volcanic ash/pumice (Arthur et al., 1980).

SITE C0020A LITHOSTRATIGRAPHY

IODP Hole C0020A (41°10.5983′N, 142°12.0328′E; 1180 m water depth) was drilled using riser drilling during IODP Expedition 337 as an extension of JAMSTEC Hole C9001D (Aoike, 2007) drilled during the 2006 *D/V Chikyu* shakedown expedition. Drilling began at 647 mbsf and continued to 2466 mbsf (Fig. 3-1) (Expedition 337 Scientists, 2013). One to three spot cores (rotary core barrel) were recovered approximately every 100 m between 1276.5 and 2466 mbsf, except for continuous coring between 1919-2002.3 mbsf.

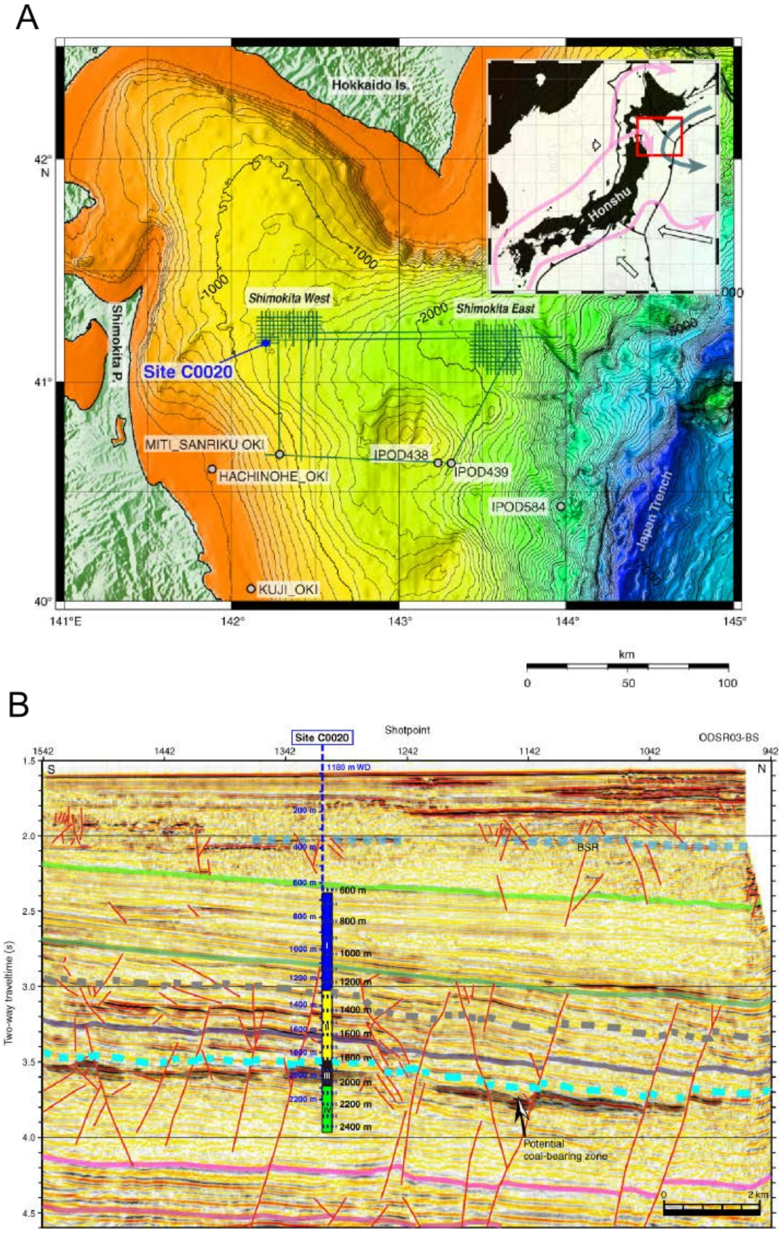

Figure 3-1. A) Location map with the location of Site C0020A. Inset shows plate tectonic configuration and plate motions. B) Drilling depths with seismic reflection profile. From Expedition 337 Scientists, 2013.

Lithostratigraphy at Site C0020A consists of a transition from a terrestrial wetland to a marine continental slope sedimentary environment (Expedition 337 Scientists, 2013). Unit I (636.5–1256.5 mbsf; late Pliocene to Miocene) consists of diatom-rich silty clay consistent with a marine hemipelagic environment. Unit II (1256.5–1826.5 mbsf; Miocene) is comprised of silty shale, siltstone, and sandstone. Observations of *Cruziana* ichnofacies and symmetric wave ripples, along with an increase in glauconite and plant material, suggest the transition to a continental shelf environment is preserved within Unit II (Expedition 337 Scientists, 2013). Lignite fragments were observed in cuttings in Unit II between 1526.5-1546.5 mbsf and downhole logging identified three coal beds, ranging from 0.3 to 0.9 m in thickness. Unit III (1826.5–2046.5 mbsf; early Miocene to late Oligocene) contains numerous coal beds interbedded with sandstones, siltstones, and coaly shale. These coal beds range from 0.3 to 7.3 m in thickness and are comprised of low maturity lignite. Flaser and lenticular bedding, cross-bedding, and extensive bioturbation present within Unit III suggest a nearshore to estuarine/intertidal environment (Expedition 337 Scientists, 2013). Unit IV (2046.5–2466 mbsf; early Miocene) is comprised of silty shale, sandstone, and siltstone. Fluctuations between fine- and coarse-grained beds suggest tidal flats and channels within a fluviodeltaic system. Unit III is mostly devoid of coal beds, except for a 0.9 m thick coal bed at 2448 mbsf, near the bottom of the hole.

There are large increases in κ between 1919-1955 mbsf in Unit III (Fig. 3-2). The sharp increase in κ, up to 975 SI x 10^{-6} occurs in sediments adjacent to, but rarely within, coal beds. These increases are generally several cm thick and often are associated with dark laminations (Fig. 3-3). Average κ within coal intervals is 13.3 SI x 10^{-6} compared to 32.2 SI x 10^{-6} in all other lithologies. There is an additional sharp increase in κ at 1599.0-1599.16 mbsf associated with a coarse-grained gravel containing rounded pebbles and cobbles of igneous rock. Just below the high κ interval, there is a spike in Fe/Al ratios from X-ray fluorescence (XRF) increase at 1969.91, 1975.42, and 1992.35 mbsf. Fe/Al identifies samples in which non-clay iron minerals are more prevalent. Fe/Al increases to 2.1 to 18.7 from an average background of 1.0 in core samples and 0.4 in cuttings, suggesting an increase in non-silicate Fe, such as iron oxides and iron sulfides.

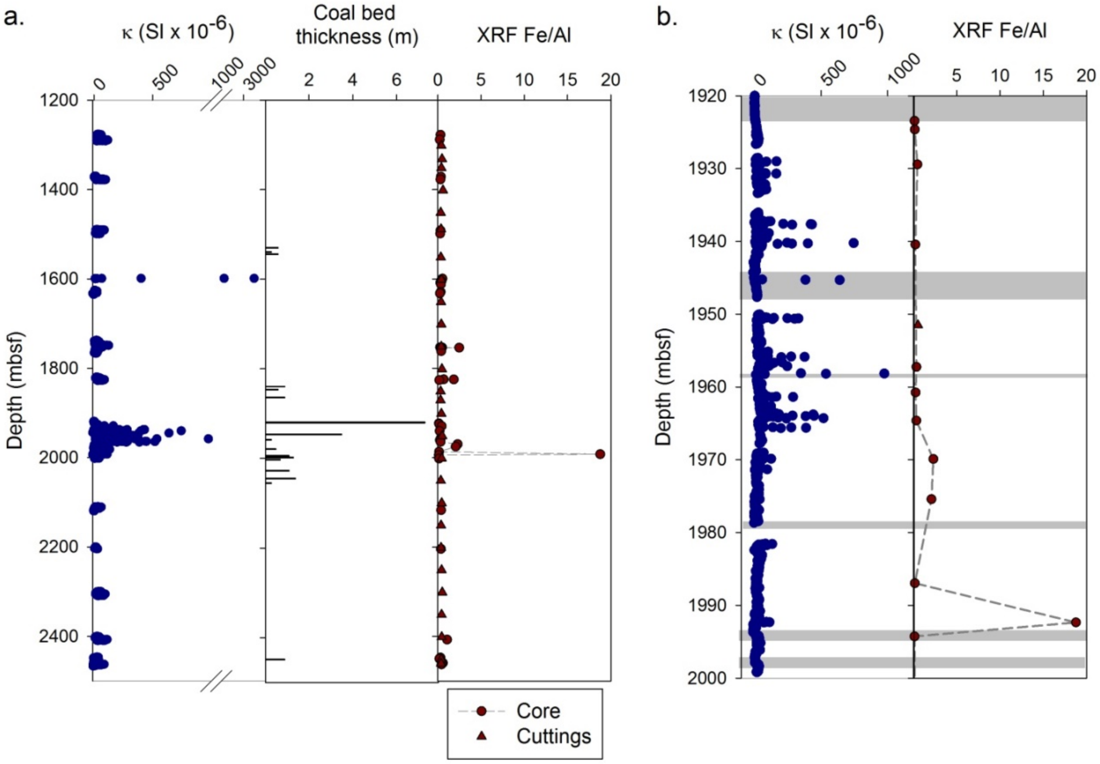

Figure 3-2. Shipboard measurements of magnetic susceptibility, XRF Fe/Al, and coal thickness. a) all of Hole C0020A b) Unit III.

METHODS

Onboard *D/V Chikyu*, samples between 10 and 20 cm^3 were selected from working half and whole round drill core sections, flushed with nitrogen and vacuum-sealed. No samples were collected from drill cuttings. These samples were chosen based on the downhole pattern in shipboard κ measurements and to be representative of recovered lithologies. Samples were stored at sea and shipped at 2 °C, and then stored in the laboratory at -20 °C. Six additional samples were sampled from archived sediment cores after Expedition 337. A 1 cm^3 sub-sample was cut from within each sample and measured for magnetic susceptibility and subjected to IRM acquisition and 3-axis thermal demagnetization analysis. Semi-consolidated samples were wrapped in aluminum foil before IRM analysis to prevent loss of material during heating. In total, 144 samples were analyzed for χ and IRM analysis at the University of New Hampshire Paleomagnetism laboratory.

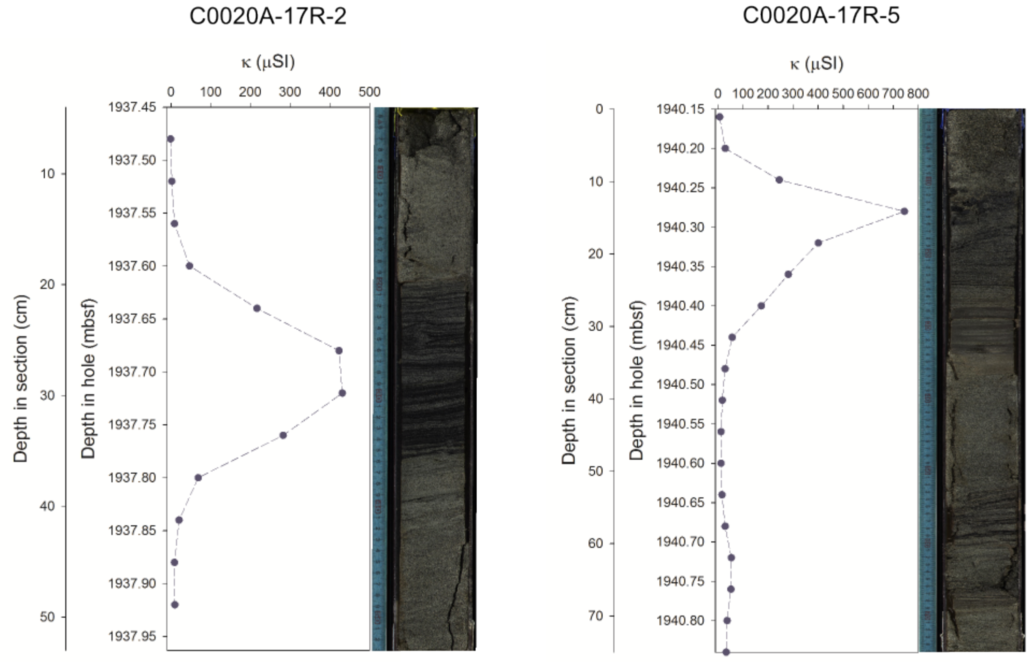

Figure 3-3. Example increases in κ with core image. Increases in κ often occur in laminated sediments with wavy laminations and flaser bedding.

Shipboard measurements of κ were measured using a Geotek whole round multisensor core logger (MSCL). Mass-normalized magnetic susceptibility (χ) was measured using a Bartington MS2 magnetic susceptibility meter. Each sample was measured three times and the average was recorded. Both low-field and high field susceptibility was measured, and then used to calculate the frequency-dependence of magnetic susceptibility (f_d %).

Remanent magnetism was measured at six orientations (three axes in two directions) using an HSM2 SQUID spinner magnetometer or a 2G 755 superconducting rock magnetometer at the UNH Paleomagnetism Laboratory. Each sample was measured for natural remanent magnetism (NRM) and then subjected to a step-wise acquisition of IRM. IRM was applied using an ASC IM-10 impulse magnetizer over sixteen steps from background to 1.1 T (Table 3-1), and measured after each step. A magnetic field of 1.1 T is sufficient to approximately reach saturation IRM (SIRM) of magnetite, titanomagnetite, greigite, and pyrrhotite, but not hematite or goethite. 1.1 T was sufficient to reach saturation in all samples from Hole C002A. Coercivity was quantified from the acquisition curves using a linear acquisition plot (Kruiver et al., 2001) to obtain $B_{1/2}$, the field that imparts one-half of SIRM. A backfield IRM of -100 mT and -300 mT, in the opposite direction of the acquisition curve, were applied for the calculation of an S ratio (e.g. Verosub and Roberts, 1995; Quinton et al., 2011):

$$S_{xmT} = \frac{IRM_{-xMT}}{SIRM}$$

This approach allows for the determination of whether a magnetic assemblage is dominated by low coercivity (e.g. titanomagnetite, greigite) or high coercivity (e.g. goethite, hematite) minerals After acquisition of IRM at 1.1 T along a primary axis, fields of 400 mT and 120 mT were imparted at right angles to the primary axis (Lowrie, 1990). I refer to IRM along the 1.1 T, 400 mT, and 120 mT axes as the hard, medium, and soft axes respectively. Samples were then heated in a stepwise thermal demagnetization using an ASC TD48-SC thermal demagnetizing oven from room temperature to 680 °C over 21 steps (Table 3-2).

Table 3-1. Acquisition steps of the applied field (in mT) used during IRM and backfield analysis

IRM acquistion steps (mT)
0
20
50
80
110
150
200
300
400
500
600
700
800
900
1000
1100
-100
1100
-300
1100

RESULTS

Mass-dependent χ measured in the laboratory closely matches the pattern observed in the shipboard volume-dependent κ measurements (Fig. 3-4), suggesting little to no alteration of the magnetic mineral assemblage after core collection/sampling. The Pearson correlation coefficient between these two data sets is 0.93. LF χ ranges from -7.7 to 265.6 10^{-8} kg/m^3 (mean: 18.3 10^{-8}

kg/m^3, median: 9.0 10^{-8} kg/m^3). HF χ ranges from -4.4 to 229.8 10^{-8} kg/m^3 (mean: 17.2 10^{-8} kg/m^3, median: 9.1 10^{-8} kg/m^3).

Table 3-2. Heating steps (in °C) used during thermal demagnetization

Thermal demagnetization steps (°C)
25
50
75
100
125
150
200
250
275
300
325
350
375
400
500
540
580
600
620
650
680

All samples showed acquisition curves typical of low-coercivity minerals reaching SIRM below 200 mT (Fig. 3-5). Likewise, the soft axis (120 mT) contains the dominant fraction of IRM after three-axis magnetization. $B_{1/2}$ ranges between 23 and 98 mT (mean: 48 mT), with the highest coercivities in Unit II at approximately 1500 mbsf and decreasing to Unit III (Fig. 3-6). S_{100} varies from -0.85 to 1.01 with a mean of 0.65. S_{100} is lowest in Unit II and in coal samples from Unit III (Fig. 3-6). Mean S_{300} is 0.89 and 138 out of 144 samples are greater than 0.75. Few samples with low S_{300} ranging from -1.17 to 0.64 are restricted to coal or coaly shale lithologies.

NRM follows trends in magnetic susceptibility ranging from 0.3 to 68,600 mA/m (median: 12 mA/m) (Fig. 3-6). Similarly, SIRM follows a pattern similar to χ and ranges from 31 to 221,100 mA/m (median: 1262 mA/m). SIRM/χ ratios are elevated in a substantial portion of samples in Unit II, and several samples in Units III and IV (Fig. 3-6).

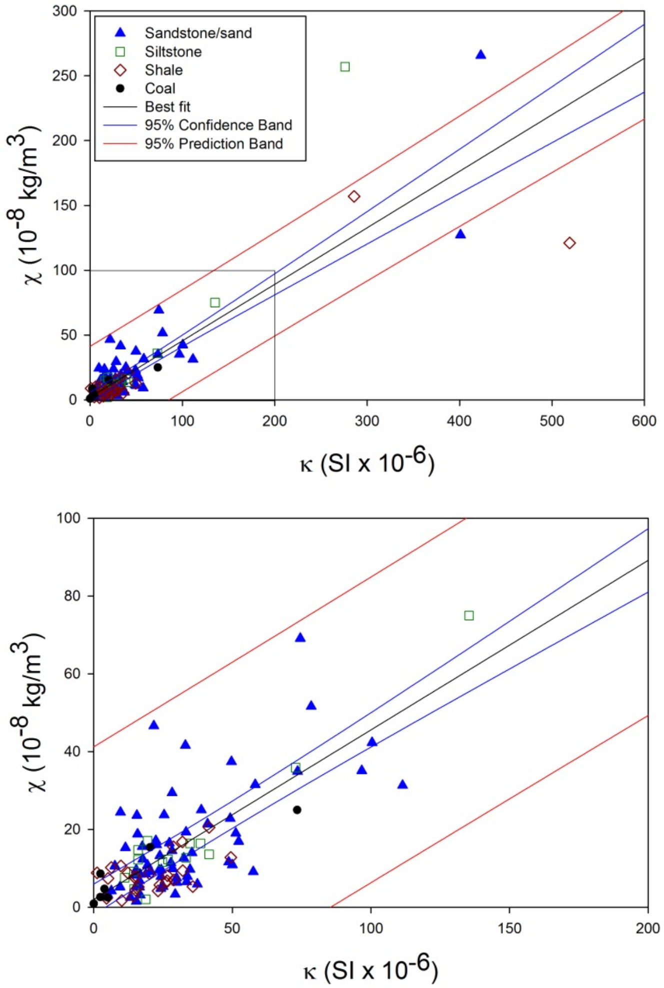

Figure 3-4. Correlation of shipboard volume-normalized magnetic susceptibility (κ) from MSCL and post-cruise mass-normalized magnetic susceptibility measurements (χ). Correlation between data indicates little to no alteration to the magnetic mineral assemblage since sample. The lower panel is a zoomed view of the lower magnetic susceptibility samples.

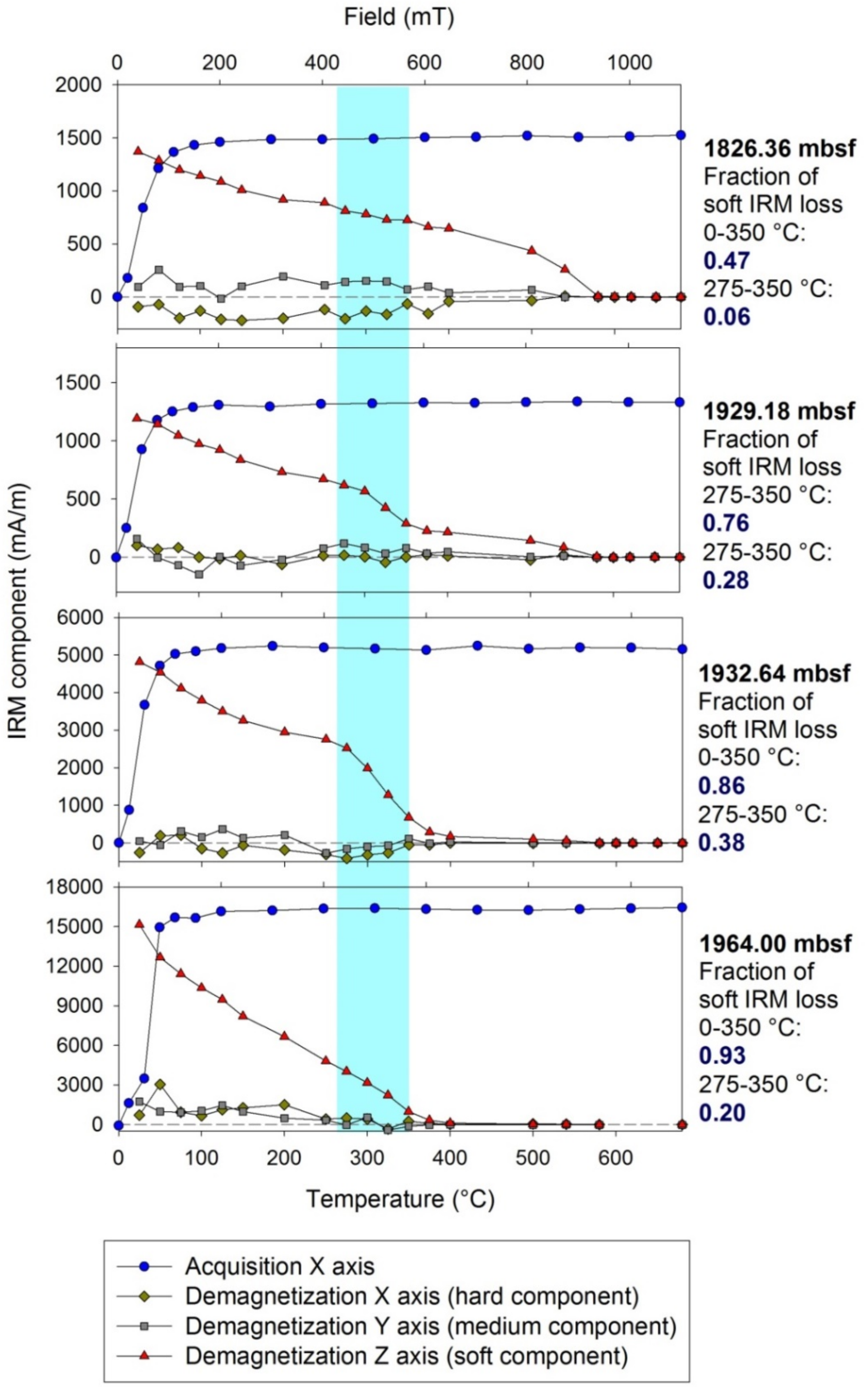

Figure 3-5. Example IRM and thermal demagnetization results showing increase in loss of IRM between 275-350°C. All samples show low-coercivity and saturation by 200 mT. Samples in Units II, IV, and the upper portion of Unit III show a relatively linear decrease in IRM to 580 ºC. Between 1930 and 1995 mbsf the fraction of IRM lost between 275 and 350 ºC increases.

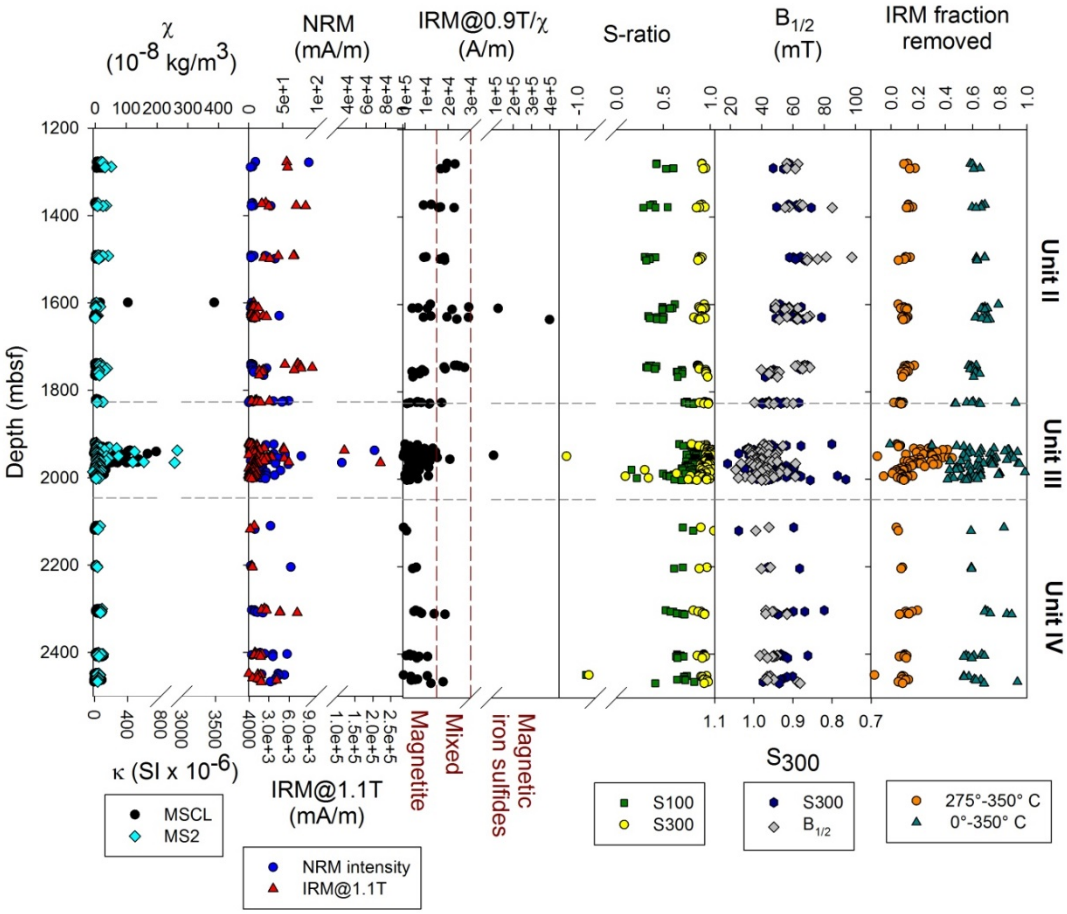

Figure 3-6. Down core rock magnetic results including laboratory-measured χ, shipboard κ, natural remanent magnetism (NRM), isothermal remanent magnetism (IRM) at 1.1T, IRM at 0.9T/ χ, -100mT and -300 mT S-ratios, coercivity (B1/2), and the IRM fraction removed between 275-350 ºC and 0-350 ºC. Range of magnetite, magnetitic iron sulfides, and mixed magnetite and magnetic iron sulfides from Larrasoaña et al. (2006).

Thermal demagnetization removed all IRM by 580 °C or below in all samples, and in all samples the primary carrier of IRM was the Z (soft) axis. Demagnetization curves in samples from Unit II, Unit III between 1920-1925 and 1995-2002 mbsf, and in Unit IV are characterized by a linear decrease to 580 °C (Fig. 3-5a). Samples between 1925-1973 mbsf have demagnetization curves in which soft IRM decreases overall to 580 °C but with a pronounced decrease between 275-350 °C (Fig. 3-5b,c). In the interval 1979-1993 mbsf, demagnetization curves decrease linearly to 350-400 °C (Fig. 3-5d). The drop in IRM below 350 °C is represented in downcore patterns by the fraction of soft IRM lost between 0-350 °C and 275-350 °C (Fig. 3-6 and 3-7). There is a pronounced increase in the fraction of soft IRM lost 0-350 °C and 275-350 °C at depths between 1925 and 1973 mbsf (Fig. 3-7). Between 1979-1993 mbsf, and at 1826, 2110, 2307, 2309, and 2463 mbsf, there is and enhanced fraction of soft IRM lost 0-350 °C, but no distinct drop at 275 °C.

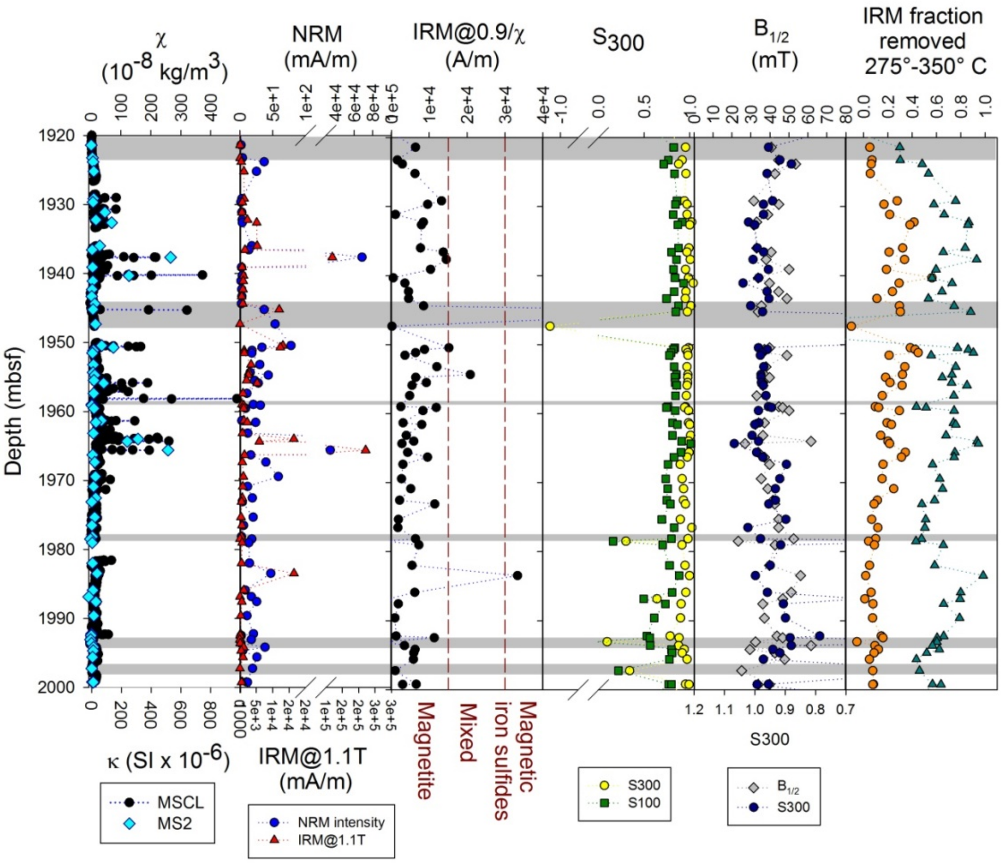

Figure 3-7. Unit III rock magnetic results results including laboratory-measured χ, shipboard κ, natural remanent magnetism (NRM), isothermal remanent magnetism (IRM) at 1.1T, IRM at 0.9T/ χ, -100mT and -300 mT S-ratios, coercivity (B1/2), and the IRM fraction removed between 275-350 ºC and 0-350 ºC.. Range of magnetite, magnetitic iron sulfides, and mixed magnetite and magnetic iron sulfides from Larrasoaña et al. (2006). Gray bars indicate coal intervals.

DISCUSSION

Magnetic Mineral Assemblage

Results of IRM acquisition (low-coercivity) and demagnetization (580 °C) suggest a magnetic mineral assemblage dominated by magnetite for samples in Unit II, Unit III (except 1925-1995 mbsf), and Unit IV. All samples saturated below 200 mT suggesting the dominant presence of low-coercivity minerals. Plots of SIRM/ χ and $B_{1/2}$ are consistent with (titano)magnetite for all except for three samples that are consistent with pyrrhotite (Peters and Dekkers, 2003) (Fig. 3-8). Two samples in Unit II and and one sample in Unit III show high SIRM/ χ ratios typical of magnetic iron sulfides (Dekkers, 1988; Roberts, 1995; Dekkers et al., 2000). However, these samples do not show a characteristic unblocking temperature of 350 °C for greigite (Roberts, 1995) or 325 °C for pyrrhotite (Lowrie, 1990). These samples possibly represent precipitates associated with diagenesis of marine sediments, but these iron sulfides oxidized early during the thermal demagnetization process.

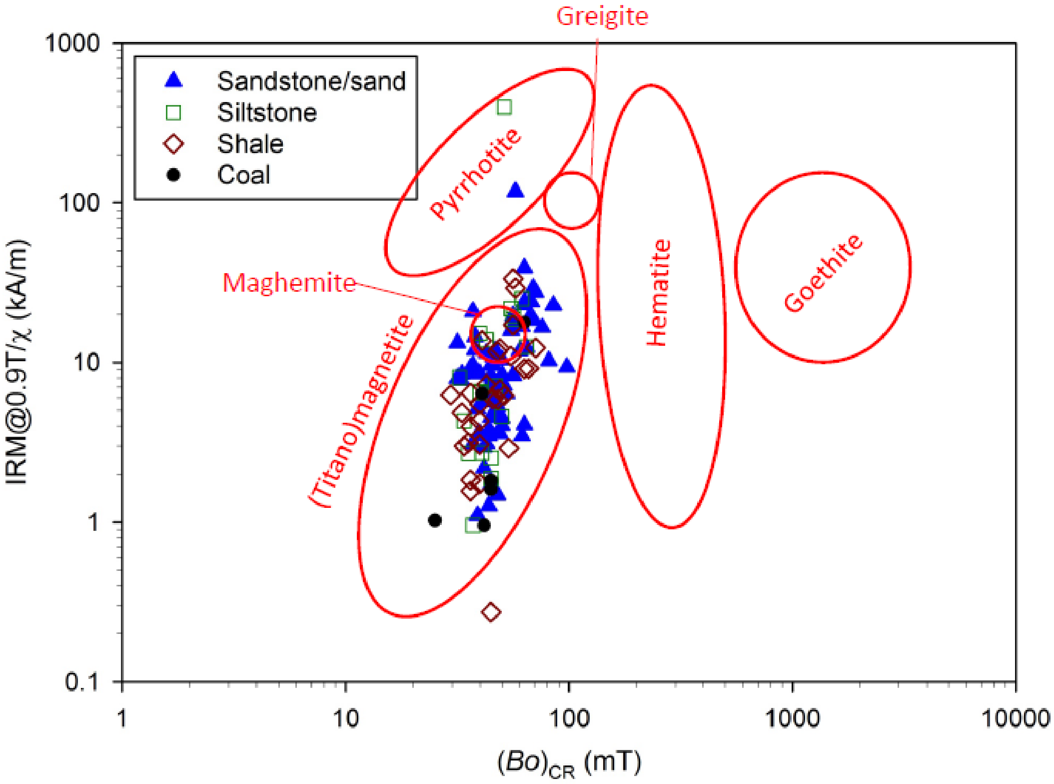

Figure 3-8. Cross plot of SIRM/χ and B1/2. Mineral ranges from Peters and Dekkers (2003).

Samples in Unit III that show a significant portion of soft IRM with an unblocking temperature at approximately 350 °C are consistent with the demagnetization of magnetic iron sulfides, maghemite, or titanomagnetite ($Fe_{3-x}Ti_xO_4$, where x= ~0.25). However, few samples have SIRM/ χ and $B_{1/2}$ that are consistent with greigite or pyrrhotite (Peters and Dekkers, 2003). Additional measurements of χ after long exposure to oxygen (approximately 2 years) do not show a decrease relative to the shipboard measurements, indicating that magnetic iron sulfides vulnerable to oxidation are not a likely significant component. A magnetic mineral assemblage with a large, metastable magnetic iron sulfide component would likely experience a loss in χ after prolonged exposure to oxygen (Hunger and Benning, 2007).

It is likely that the mineral associated with the 350 °C unblocking temperature is titanomagnetite. Along the titanomagnetite series, the Curie temperature drops as Ti content increases, and for $Fe_{3-x}Ti_xO_4$, where x=0.25 the Curie temperature is ~350 °C (Butler, 1992). IRM acquisition and χ results are consistent with the dominant presence of (titano)magnetite but cannot rule out a possible minor maghemite(γ-Fe_2O_3)/titanomaghemite(γ-$TiFeO_3$) component. Maghemetization of (titano)magnetite can occur in oxygenated sediments, but is more common component in pelagic settings where low sedimentation rates yield long exposure to oxygenated bottom waters (Smirnov and Tarduno, 2000; Xu et al., 1997). In this record, surface sediments were likely exposed to oxygenated bottom waters, but due to high sedimentation rates and TOC throughout Site C0020 (Expedition 337 Scientists, 2013) (titano)magnetite was likey buried quickly into anoxic conditions.

Depositional Environment

Overall κ and χ measurements indicate general differences between lithologies, with highest magnetic susceptibility in sandstone followed by siltstone, shale, and coal; however, there is significant overlap between individual samples of varying lithologies (Figure 3-9), implying a possible influence of grain size on magnetic susceptibility.

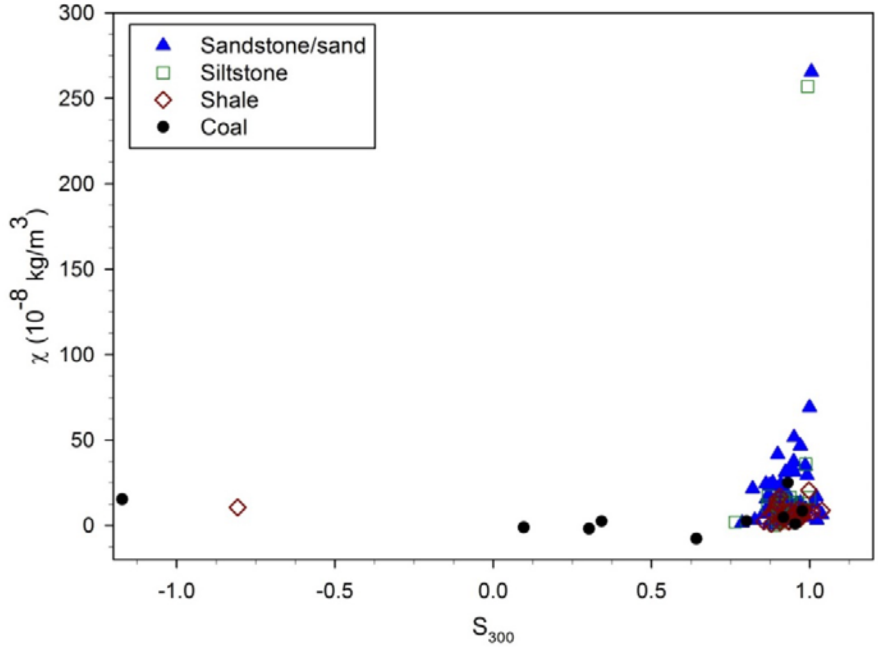

Figure 3-9. Cross plot of S300 and χ by lithology.

The ultimate source for (titano)magnetite at Site C0020A is mostly likely from weathering of rocks within northern Honshu. Angular lithic fragments were commonly observed within Unit III (Expedition 337 Scientists, 2013) indicating minimal transport from source to deposition. (Titano)magnetite is a common constituent in volcanic rocks in Japan (Akimoto and Katsura, 1959; Sakuyama and Nesbitt, 1986; Hoshi and Teranishi, 2007; Ohba et al., 2007; Suzuki, 2008), magnetite-series granitic rocks (Tagaki, 2004), and hornfels facies metamorphic rocks (Tsusue, 1962) within Honshu. Magnetite has been observed as the primary detrital magnetic mineral in the Nankai accretionary complex (Kanamatsu et al., 2012; Zhao etal., 2013; Kars et al., 2015), and Japan Sea (Razjigaeva and Naumova, 1992; Vigliotti, 1997). Paleomagnetic studies at DSDP and ODP sites in the Japan trench and forearc basin show stable remanance (Hall and Smeltzer, 1980; Niitsuma, 1986; Kanamatsu and Niitsuma, 2004), but do not directly address magnetic mineral assemblage. The (titano)magnetite-dominant magnetic mineral assemblage at C0020A is consistent with sites around the Japanese margin.

The increases in magnetic susceptibility within Unit III are likely a result of density sorting of heavy minerals in the intertidal/fluvial environment of Unit III. Magnetite has a density (5.20 g/cm^3) nearly double that of quartz (2.65 g/cm^3) (Schön, 2004), and commonly shows hydraulic sorting in beach and fluvial environments (e.g. Slingerland and Smith, 1986; Komar, 1989). The anomalous increases in χ (to ~100-400 10^{-8} kg/m^3) are similar to the range observed in modern placer deposits at an iron sands lagoon in New Zealand (~50-2000 10^{-8} kg/m^3) (Badesab et al., 2012). Placer deposits of titanomagnetite, often referred to as iron sands, magnetic sands, or black sands, are prevalent on the North Island of New Zealand (Bryan et al., 2007; Badesab et al., 2012) and the southeast and southwest Indian margins (Mallik et al., 1987; Angusamy et al., 2007). Iron sands deposits have been observed in Japan, and these deposits have been used industrially in Japan for at least a millennium (Erselcuk, 1947). Placer sorting is indicative of a partially erosive setting (Frihy, 1994) and in Unit III of Hole C0020A the presence of iron sands suggests that the sharp transitions between these sands and coal are disconformities between a high-energy nearshore or fluvial environment and a lower-energy terrestrial environment. Most intervals of increased magnetic susceptibility occur within fine-to-medium sandstones which is consistent with an upper beach swash-zone (Hughes et al., 2000), fluvial, or lagoonal (Badesab et al., 2012) environment. Ti-rich and Ti-poor titanomagnetite only vary in density by approximately 3% (Hunt et al., 1995), and sorting via transport or wave action is unlikely a direct factor in driving a transition from Ti-rich to Ti-poor titanomagnetite.

A change in provenance could potentially explain the shift from Ti-poor to Ti-rich titanomagnetite. Geochemical analysis of titanomagnetite in Japanese volcanic rocks indicates that Ti-content is higher within titanomagnetite in basalt (~15-25 mol % TiO_2) than in intermediate andesite-dacite (~10-20 mol %) or rhyolite (~0-10 mol %) (Akimoto and Katsura, 1959; Suzuki, 2008). Back-arc and intra-arc extension that led to the creation of the Sea of Japan occurred during the early to middle Miocene (Taira, 2001; Tatsumi et al., 1989, 1990; Yamaji) resulting in the widespread eruption of Miocene basalt in northern Honshu (Ujike and Tsuchiya, 1993; Yoshida, 2001), before a return to more intermediate-to-felsic eruptions in northern Honshu during the late Miocene (Sato and Amano, 1991; Yoshida, 2001). The increased Ti-content within (titano)magnetites in early Miocene sediments of C0020A may represent an increased input of basaltic provenance during the rifting phase of northern Japan. However, XRF measurements of Ti and Fe do not indicate a shift in overall sediment Ti-content within the interval of decreased Curie temperature in Unit III. In addition, in order explain the change in Ti-content by this provenance change, the eruption of mafic volcanic rocks during the early Miocene would require deposition of the eroded materials within the forearc within the same time period, and subsequent cessation of this deposition later in the Miocene, even though early Miocene mafic volcanics are still common throughout northern Honshu (Geologic Survey of Japan, 2012). It is unlikely that provenance changes explain the shift in titanomagnetite Ti-content that is associated with proximity to the Unit III coal beds.

Biogeochemical Implications

Iron may play a role in the deep biosphere as a potential source of Fe^{3+} for iron reduction, possibly coupled to methane oxidation (Riedinger et al., 2014). The presence of (titano)magnetite as the dominant magnetic mineral suggests the potential of bioavailable Fe^{3+} for past and present iron reduction in sediments offshore Shimokita since burial and presently within the deep biosphere. Pure magnetite ($Fe^{2+}Fe^{3+}_2O_4$) is a mixed Fe^{3+} ,Fe^{2+} oxide, while pure ulvöspinel ($Ti^{4+}Fe^{2+}{}_2O_4$) contains only Fe^{2+}. Thus, the range in Fe content of the magnetite-titanomagnetite series represents range in potential electron acceptor availability. The presence of any maghemite (γ-$Fe^{3+}{}_2O_3$) would be an additional source of Fe^{3+} for the deep biosphere. The increase in fraction of IRM removed between 275-350 °C and 0-350 °C in Unit III suggests a lower availability of Fe^{3+} that is likely a result of alteration of the magnetic mineral assemblage by iron reducing bacteria. Thin section observations of iron oxides under reflected light show irregular-shaped grains that may have been altered after deposition (Fig. 3-10).

Phylogenetic analysis of 16S rRNA indicates an increased presence of *Firmicutes* phylum bacteria (Inagaki et al., 2015) in Units III and IV that likely include iron-reducing bacteria. The low-sulfur terrestrial/estuarine environment of Units III and IV (Expedition 337 Scientists, 2013) and terrestrial microbial communities within these units (Inagaki et al., 2015) suggest a limited role for sulfate reduction/anaerobic oxidation of methane, thus alteration of magnetic minerals is not likely dominated by reaction with hydrogen sulfide. Iron-reducing bacteria are common in terrestrial soils (e.g. Achtnich et al., 1995; Dubinsky et al., 2010; Rakshit et al., 2009). Total sulfur (TS) decreases within Unit III relative to Units II and IV (Expedition 337 Scientists, 2013), indicating a reduction in iron sulfide precipitation caused by a limitation in sulfate availability within a brackish-to-freshwater environment compared to a fully marine environment. Typical river water contains two orders of magnitude less sulfate and one order of magnitude more iron compared to seawater (Livingstone, 1963; Pilson, 1998). The presence of indigenous terrestrial microbial communities within the sediments of Units III and IV (Inagaki et al., 2015), also indicate a change in the availability of electron acceptors to that typical of a terrestrial, freshwater environment from the overlying sulfate-rich marine environment. Although there is a lack of porewater samples within the consolidated sediments of C0020A, the original pH within the terrestrial sediments of Unit III was likely slightly acidic, which is favorable for microbial iron reduction of magnetite (Kostka and Nealson, 1995). I suggest that the apparent increase in Ti within titanomagnetite may be a result of the selective dissolution via iron reduction in which the more Fe^{3+}-rich, Ti-poor magnetite is selectively removed over time, leaving the more Fe^{3+}-poor, Ti-rich magnetite as a residual, less desirable electron source. The terrestrial environment of Unit III along with the potential presence of iron-reducing bacteria suggests the possibility that Ti-poor magnetite has been selectively removed over time.

The presence of the shift in titanomagnetite content occurs within intervals with numerous coal beds, and coal may serve as an important source of organic carbon as an electron donor to the surrounding sediments. Coal can serve a bioreactor in which complex coal macerals are degraded into simple, more labile molecules (e.g. acetate, H_2, CO_2) that become mobile as electron donors that can fuel methanogenesis (Strąpoć, 2008). Peat is a major source of dissolved organic carbon (DOC) into underlying sediments (Dalva and Moore, 1991). During burial and through early coalification, the peat/lignite intervals at Site C0020 were a likely source of DOC to the surrounding low TOC sediments. Most coal beds within Unit III have little to no ferrimagnetic fraction, thus presenting a physical separation between electron donors and electron acceptors (iron oxides), necessary to fuel a shift in titanomagnetite composition driven by dissimilatory iron reduction. These coal beds are interbedded among fine-to-medium sand/sandstones indicating adjacent proximity of high permeability sediments, containing magnetite, directly adjacent to a DOC and CH_4 source. Within Unit III, the presence of unconsolidated sands suggests that the connection of fluids between coal beds and the surrounding sediments is maintained, but increasingly constricted with depth. Porosity decreases with depth from >0.8 % at the top of overlying Hole C9001C to an average of 0.26 wt. % in Unit

III (Aoike, 2007; Expedition 337 Scientists, 2013). Within carbonate-cemented coal intervals porosity is further reduced to <0.15 %. The decrease in porosity with depth due to compaction and diagenetic cements likely limits porosity, thus impeding the connection between magnetite-sourced electron acceptors and coal-sourced electron donors. This presumed decrease in permeability, along with the decrease in cell concentration with depth (Inagaki et al., 2015), suggests that the maximum rates for iron reduction likely occurred during shallow burial and declined with further burial depth.

Although iron reduction is thermodynamically more favorable than sulfate reduction and methanogenesis (Froelich et al., 1979), Fe^{3+}-bearing iron oxides persist during burial of sediments through the sulfidic and methanic zones. The presence of Fe^{3+} in the crystalline structure of iron oxides serves as a barrier to bioavailability, and limits reaction rates due to the surface area necessary for contact to iron reducers. Humic acids comprise a significant fraction of lignite (e.g Allard, 2006; Cavani et al., 2003; Gonzales-Vila, 1992, 1994; Ibarra and Juan, 1985) and can transfer electrons to iron oxides during acetate oxidation, alleviating the neccesity of direct contact between Fe^{3+}-reducing bacteria and iron oxides (Lovely et al., 1996). The presence of peat/lignite in the subsiding environment at Site C0020A likely acted as a significant source of humic substances in DOC to the surrounding sediments, likely enhancing iron reduction within intervals in porewater contact with the peat/coal intervals. Maximum methane content occurs within the coal beds, including production by present-day methanogenesis (Inagaki et al., 2015). Methane oxidation may be coupled to iron reduction (Konhauser et al., 2005; Beal et al., 2009; Segarra et al., 2013; Riedinger et al., 2014; Thauer and Shima, 2008), suggesting methane exporterd from peat/lignite as a potential electron donor for iron reduction.

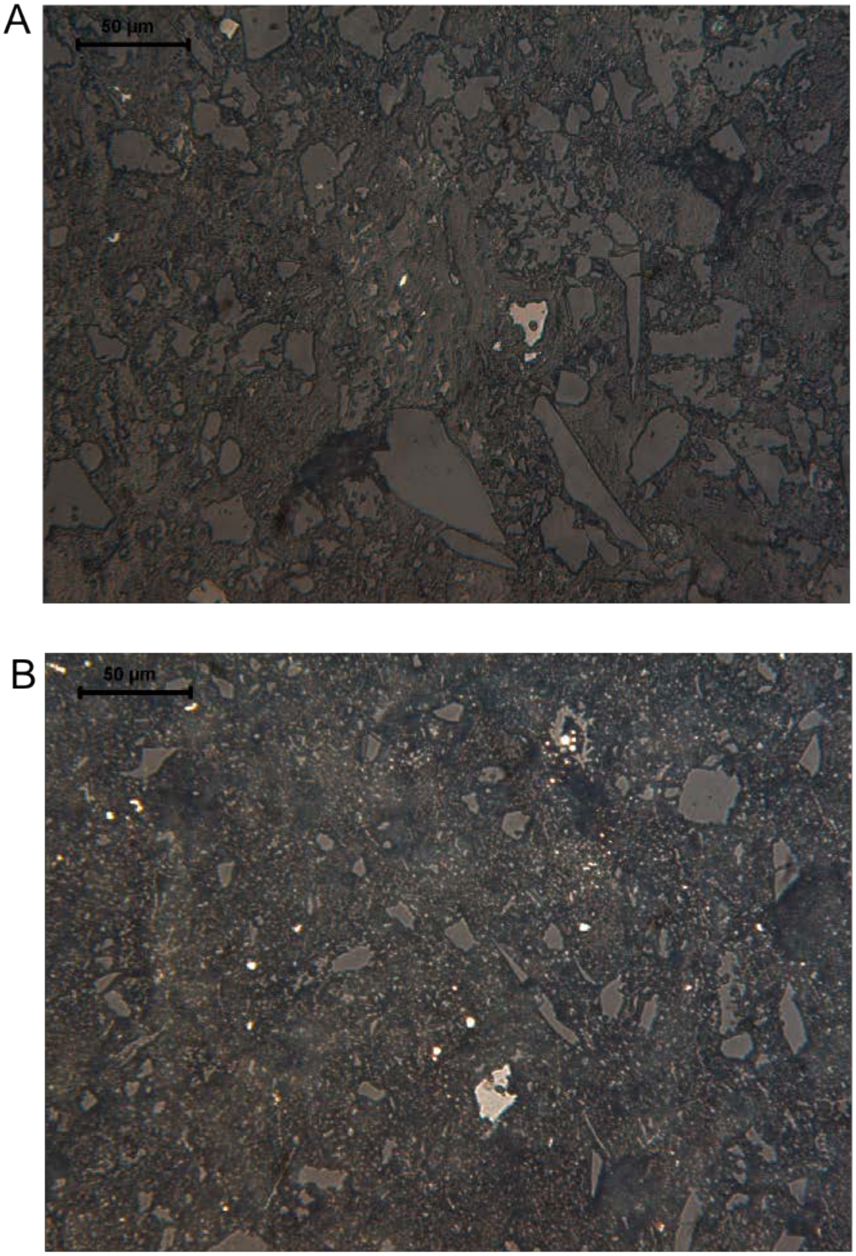

Figure 3-10. Reflected light photomicrographs of polished thin sections from samples within Unit III showing iron oxides (light gray) with irregular edges and holes within minerals suggestive of post-depostional degradation. A. C0020A-19R-6 22 cm, 1955.90 mbsf, sandy siltstone. B. C0020A-20R-5 22 cm, 1964.00 mbsf, silty shale.

The common occurrence of authigenic siderite nodules throughout Unit III also indicates a diagenetic environment consistent with microbial iron reduction. Fe^{2+} produced via iron reduction is available to react with bicarbonate within the methanic zone when H_2S is not present (Berner, 1981; Maynard, 1982) or in an environment in which rates of iron reduction are greater than sulfate reduction (Pye et al., 1990). Fe^{3+}-reducing bacteria can produce microbially-derived siderite as a direct by-product of dissimilatory iron reduction (Lovely and Phillips, 1986; Mortimer and Coleman, 1997). The decrease in TS within Unit III (Expedition 337 Scientists, 2013) indicates sulfur limitation and an environment in which the sink for Fe^{2+} liberated from magnetite via iron reduction is siderite rather than pyrite.

Based on the relative increase in TiO_2, we estimate that the average loss of magnetite due to dissimilatory iron reduction in Unit III is 0.1 wt. %, with samples with as much as 1.1 wt. % loss. This loss corresponds to an estimated rate of magnetite loss since burial in the Early Miocene (maximum 23 Myr) that occurs at a Miocene-to-present averaged rate of 0.33 μmol cm^{-3} Myr^{-1} and a maximum rate of 5.1 μmol cm^{-3} Myr^{-1}. Magnetite loss occurs at rate on the order of 10^{-9} to 10^{-7} μmol h^{-1} $cell^{-1}$ in modern cultures of iron reducing bacteria (Nealson and Saffarini, 1994; Kostka and Nealson, 1995). The observed loss within Unit III would require rates on the order of 10^{-11} μmol h^{-1} cm^{-3} for the average magnetite loss, and 10^{-10} μmol h^{-1} cm^{-3} for the a maximum estimated loss.The estimated observed loss in Unit III is reasonable even below the lowest known rate of microbial magnetite dissolution, even for a single cell per cm^3. Although magnetite loss has not been observed via iron-dependent AOM, rates of AOM with ferrihydrite as an electron acceptor can occur at 6 μmol yr^{-1} cm^{-3} (Beal et al., 2009). If AOM coupled to magnetite reduction can occur at a rate even several orders of magnitude slower than ferrihydrite reduction, AOM could explain the observed loss of magnetite.

Overall, the combined influence of a sulfate-depleted, methane-rich, and likely humic acid-rich sediment could drive microbial loss of magnetite via dissimilatory iron reduction.

Further work involving cultures of the microbial communities at this depth, and experiments involving these microbes and titanomagnetites may provide additional insight to evaluate the role of dissimilatory iron reduction involving crystalling iron oxides at Site C0020A.

CONCLUSIONS

I investigated the overall magnetic mineral assemblage, as well as the source of the anomalous increases in magnetic susceptibility at IODP Hole C0020A. The magnetic assemblage is dominated by low-coercivity magnetite-titanomagnetite series minerals. In Units II and IV, the linear loss of low-coercivity IRM during thermal demagnetization to 580 °C suggests the presence of Ti-poor magnetite. Within the intervals 1925-1975 mbsf and 1979-1993 mbsf partial or complete loss of low coercivity IRM to 350-400 °C suggests an increased Ti content in the (titano)magnetite. The most likely cause of the shift in titanomagnetite composition is the selective dissolution, via microbial iron reduction, of Fe^{3+}-rich, Ti-poor magnetite, which would preferentially leave Fe^{3+}-poor, Ti-rich magnetite in the geologic record. Anomalous increases in magnetic susceptibility are not simply explained by changes in lithology, but can occur within multiple lithlogies deposited within a nearshore-to-intertidal depositional environment. In this record, magnetic susceptibility increases often occur in fine-to-medium sandstones associated with dark laminations. The depostional environment, coupled with the observed range in magnetic susceptibility suggests these anomalous intervals of high magnetic susceptibility are thin placer deposits, formed by wave action and/or longshore transport. Early after deposition of this nearshore environment, microbial iron reduction most likely resulted in the alteration of (titano)magnetite in these sediments and served as a source of Fe^{3+} as a potential electron acceptor to drive potential humic acid or methane oxidation.

CONCLUSIONS

The chapters of this dissertation are linked through the use, integration, and interpretation of magnetic susceptibility in continental margin sediments. These chapters document the key aspects to consider in the interpretation of down-hole magnetic susceptibility records along marine continental margins, both from a detrital and diagenetic perspective. In Chapter 1, detrital variation in magnetic susceptibility at Hole NGHP-01-19B occurs due to changes in the strength of the Indian summer monsoon, which drives weathering on the Indian subcontinent. Decreased monsoon rainfall and chemical weathering allows for an increased presence of detrital magnetite and decreased dilution by clay minerals. In Chapter 2, an increase in magnetic susceptibility tracks with grain size in the upper 25 mbsf of IODP Hole U1325B, representing detrital transport of sands into an accretionary wedge slope basin. In Chapter 3, nearshore sediments in Unit III of IODP Hole C0020A may reflect a change in titanomagnetite source, from Ti-poor titanomagnetite in intermediate-to-felsic volcanic rocks to Ti-rich titanomagnetite in mafic volcanic rocks.

Diagenetic overprints on magnetic susceptibility, especially when recorded as a stable transformation of magnetite to pyrite, can result in a long-lasting signature that reflects past porewater biogeochemical conditions. Modern porewater profiles represent a detailed snapshot of present day biogeochemical conditions; however, with continued sedimentation and evolution of continental margin systems, porewater conditions change and redox boundaries migrate. One approach to try to identify past diagenetic processes is to look for alteration of detrital magnetic mineralogy. In Chapter 2, predicting original detrital magnetic susceptibility allows for identification of intervals of diagenetic reduction of magnetic susceptibility due to pyritization of magnetite. This approach can be used as a tool to identify intervals in which organoclastic sulfate reduction and/or anaerobic oxidation of methane were occurring at high rates or for prolonged periods of time. In Chapter 3, the shift from Ti-poor to Ti-rich titanomagnetite in coal-bearing Unit III of Site C0020A also suggests the possibility of selective dissolution of Ti-poor magnetite by iron(III)-reducting bacteria, leaving Ti-rich titanomagnetite.

Overall, these results highlight the importance of understanding magnetic susceptibility records in methane-bearing marine sediments as a mixed signal of detrital and diagenetic processes. Decoupling these signals through the integration of other types of data, may illuminate tectonic and climatic processes influencing the transport of ferrimagnetic minerals to marine sediments and the reductive diagenetic processes that alter these minerals.

LIST OF REFERENCES

Abel-Flores, J., Johnson, J., Mejía-Molina, A.E., Álvarez, M.C., Sierro, F.J., Singh, S.D., Mahanti, S., and Giosan, L., this issue. Sedimentation rates from calcareous nannofossil and planktonic foraminifera biostratigraphy in the Andaman Sea, northern Bay of Bengal, and Eastern Arabian Sea. Journal of Marine and Petroleum Geology

Achtnich, C., Bak, F., and Conrad, R., 1995. Competition for electron donors among nitrate reducers, ferric iron reducers, sulfate reducers, and methanogens in anoxic paddy soil. Biology and Fertility of Soils 19, 65-72.

Agrawal, S., Sanyal, P.,Sarkar, A., Jaiswal, M. K., and Dutta, K., 2012. Variability of Indian monsoon rainfall over the past 100 ka and its implication for C_3-C_4 vegetational change. Quaternary Research 77, 159-170.

Akimoto, S., and Katsura, T., 1959. Magneto-Chemical study of generalized titanomagnetite in volcanic rocks. Journal of Geomagnetism and Geoelectricity 10, 69-90.

Allard, B., 2006. A comparative study on the chemical composition of humic acids from forest soil, agricultural soil, and lignite deposit bound lipid, carbohydrate, and amino acid distributions. Geoderma 130, 77-96.

Altabet, M.A., Higginson, M.J., and Murray, D.W., 2002. The effect of millennial-scale changes in Arabian Sea denitrification. Nature 425, 159-162.

An, Z., Kukla, G.J., Porter, S.C., and Xiao, J., 1991. Magnetic susceptibility of monsoon variation on the Loess Plateau of Central China during the last 130,000 years. Quaternary Research 36, 29-36.

An, Z., Kutzback, J.E., Prell, W.L., and Porter, S.C., 2001. Evolution of Asian monsoons and phased uplift of the Himalaya-Tibetan plateau since Late Miocene times. Nature 2001, 62-66.

An, Z., Clemens, S.C., Shen, J., Qiang, X., Jin, Z., Sun, Y., Prell, W.L., Luo, J., Wang, S., Xu, H., Cai, Y., Zhou, W., Liu, X., Liu, W., Shi, Z., Yan, L., Xiao, X., Chang, H., Wu, F., Ai, L., and Lu, F., 2011. Glacial-interglacial Indian summer monsoon dynamics. Science 333, 719-723.

Anand, P., Kroon, D., Singh, A.D., Ganeshram, R.S., Ganssen, G., and Elderfield, 2008. Coupled sea surface temperature-seawater δ^{18}O reconstructions in the Arabian Sea at the millennial scale for the last 35 ka. Paleoceanography 23, PA4207, doi:10.1029/2007PA001564.

Angusamy, N., Dajkumar Sahayam, J., Suresh Gandhi, M., and Victor Rajamanickam, G., 2005. Coastal Placer Deposits of Central Tamil Nadu, India. Marine Georesources and Geotechnology 23, 137-174.

Antonov, J. I., D. Seidov, T. P. Boyer, R. A. Locarnini, A. V. Mishonov, H. E. Garcia, O. K. Baranova, M. M. Zweng, and D. R. Johnson, 2010. World Ocean Atlas 2009 Volume 2: Salinity. In: S. Levitus (Ed.) NOAA Atlas NESDIS 69, U.S. Government Printing Office, Washington, D.C., 184 pp.

Aoike, K. (Ed.), 2007. CDEX Laboratory Operation Report: CK06-06 D/V Chikyu shakedown cruise offshore Shimokita: Yokohama (CDEX-JAMSTEC). http://sio7.jamstec.go.jp/JAMSTEC-exp-report/902/CK06-06_CR.pdf

Arnold, R.G., DiChristina, T.J., and Hoffman, M.R., 1988. Reductive dissolution of Fe(III) oxides by *Pseudomonas* sp. 2000. Biotechnology Bioengineering 32 1081-1096.

Arthur, M.A., Von Huene, R., Adelseck, C.G., 1980. Sedimentary evolution of the Japan fore-arc region off northern Honshu, Legs 56 and 57, Deep Sea Drilling Project. Initial Reports of the Deep Sea Drilling Project, 56/57: 521-568.

Babu, C.P., Pattan, J.N., Dutta, K., Basavaiah, N., Ravi Prasad, G.V., Ray, D.K., and Govil, P., 2010. Shift in detrital sedimentation in the eastern Bay of Bengal during the late Quaternary. Journal of Earth Systems Science 119, 285-295.

Badesab, F., von Dobeneck, T., Bryan, K., Müller, H., Briggs, R.M., Frederichs, T., and Kwoll, E., 2012. Formation of magnetite-enriched zones in and offshore of a mesotidal estuarine lagoon: An environmental magnetic study of Tauranga Harbor and Bay of Plenty, New Zealand. Geochemistry, Geophysics, Geosystems 13, Q06012, doi:10.1029/2012GC004125.

Banakar, V.K., Parthiban, G., Pattan, J.N., and Jauhari, P., 1998. Chemistry of surface sediment along a north-south transect across the equator in the Central Indian Basin: an assessment of biogenic and detrital influences on elemental burial on the seafloor. Chemical Geology 147, 217-232.

Bassinot, F. C., L. Beaufort, E. Vincent, L. D. Labeyrie, F. Rostek, P. J. Müller, X. Quidelleur, and Y. Lancelot, 1994. Coarse fraction fluctuations in pelagic carbonate sediments from the tropical Indian Ocean: A 1500-kyr record of carbonate dissolution. Paleoceanography 9, 579–600.

Bassinot, F.C., Marzin, C., Braconnot, P., Marti, O., Mathien-Blard, E., Lombard, F., Bopp, L., 2011. Holocene evolution of summer winds and marine productivity in the tropical Indian Ocean in response to insolation forcing: data-model comparison. Climate of the Past 7, 815-829.

Beal E.J., House C.H., Orphan V.J., 2009. Manganese- and iron dependent marine methane oxidation. Science 325, 184–187.

Berger, A., and Loutre, M.F., 1991. Insolation values for the climate of the last 10 million years. Quaternary Science Reviews, 10, 297-317.

Berner, R.A., Scott, M.R., and Thomlinson, C., 1970a. Carbonate alkalinity in the pore waters of anoxic marine sediments. Limnology and Oceanography 15, 544-549.

Berner, R.A., 1970b. Sedimentary pyrite formation. American Journal of Science 268, 1-23.

Berner, R.A., 1982. Burial of organic carbon and pyrite sulfur in the modern ocean: Its geochemical and environmental significance. American Journal of Science 282, 451-473.

Berner, R.A. and Raiswell, R., 1983. Burial of organic carbon and pyrite sulfur in sediments over Phanerozoic time: a new theory. Geochimica et Cosmochimica Acta 47, 855-862.

Berner, R.A., 1984. Sedimentary pyrite formation: an update. Geochimica et Cosmochimica Acta, 48:605-615.

Bertrand, P., Shimmield, G., Martinez, P., Grousset, F., Jorissen, F., Paterne, M., Pujol, C., Bouloubassi, I., Buat Menard, P., Peypouquet, J.-P., Beaufort, L.,Sicre, M.-A., Lallier-Verges, E., Foster, J.M., Ternois, Y., and the Other Participants of the Sedorqua Program, 1996. The glacial ocean productivity hypothesis: the importance of regional temporal and spatial studies. Marine Geology 130, 1-9.

Beuselinck, L., Govers, G., Poesen, J., Degraer, G., and Froyen, L., 1998. Grain-size analysis by laser diffractometry: comparison with the sieve-pipette method. Catena 32, 193-208.

Bijma, J., Erez, J., and Hemleben, C., 1990. Lunar and semi-lunar reproductive cycles in some spinose planktonic foraminifers. Journal of Foraminiferal Research 20, 117-127.

Biscaye, P.E., Grousset, F.E., Revel, M., Van der Gaast, S., Zielinski, G.A., Vaars, A., and Kukla, G., 1997. Asian provenance of glacial dust (stage 2) in the Greenland Ice Sheet Project 2 Ice Core, Summit, Greenland. Journal of Geophysical Research 102, 26765-26781.

Bloemendal, J., King, J.W., Hall, F.R., and Doh, S.-J., 1992. Rock magnetism of Late Neogene and Pleistocene deep-sea sediments: Relationship to sediment source, diagenetic processes, and sediment lithology. Journal of Geophysical Research 97, 4361-4375.

Bloemendal, J., King, J.W., Hunt, A., Demenocal, P.B., and Hayashida, A., 1993. Origin of the sedimentary magnetic record at Ocean Drilling Program sites on the Owen Ridge, Western Arabian Sea. Journal of Geophysical Research 98, 4199-4219.

Blöthe, J.H. and Korup, O., 2013. Millennial lag times in the Himalayan routing system. Earth and Planetary Science Letters 382, 38-46.

Blum, P., 1997. Physical properties handbook. ODP Technical Note 26. doi:10.2973/odp.tn.26.1997

Boetius, A., Ravenschlag, K., Schubert C.J., Rickert D., Widdel, F., Gieseke A., Amann R., Jorgensen, B.B., Witte U., Pfannkuche, O., 2000. A marine microbial consortium apparently mediating anaerobic oxidation of methane. Nature 407, 623-626.

Bohrmann, G., Greinert, J., Suess, E., and Torres, M., 1998. Authigenic carbonates from the Cascadia subduction zone and their relation to gas hydrate stability. Geology 26, 647-650.

Bolton, C.T., Chang, L., Clemens, S.C., Kodama, K., Ikehara, M., Medina-Elizalde, M., Paterson, G.A., Roberts, A.P., Rohling, E.J., Yamamoto, Y., and Zhao, X., 2013. A 500,000 year record of Indian summer monsoon dynamics recorded by eastern equatorial Indian Ocean upper water-column structure. Quaternary Science Reviews 77, 167-180.

Borowski, W.S., 2006. Data report: Dissolved sulfide concentration and sulfur isotopic composition of sulfide and sulfate in pore waters, ODP Leg 204, Hydrate Ridge and vicinity, Cascadia Margin, offshore Oregon. In Tréhu, A.M., Bohrmann, G., Torres, M.E., and Colwell, F.S. (Eds.), Proceedings of the Ocean Drilling Program Results 204, 1–13.

Borowski, W.S., Rodriguez, N.M., Paull, C.K., and Ussler III, 2013. Are ^{34}S-enriched authigenic sulfide minerals a proxy for elevated methane flux and gas hydrates in the geologic record? Marine and Petroleum Geology 43, 381-395.

Brink, K., Arnone, R., Coble, P., Flagg, C., Jones, B., Kindle, J., Lee, C., Phinney, D., Wood, M., Yentsch, C., and Young, D., 1998. Monsoons boost biological productivity in Arabian Sea. Eos Transactions AGU 79, 165-169.

Brock, J.C., McClain, C.R., Luther, M.E., and Hay, W.W., 1991. The phytoplankton bloom in the northwestern Arabian Sea during the southwest monsoon of 1979. Journal of Geophysical Research 96, 20623-20642.

Bryan, K.R., Robinson, A., and Briggs, R.M., 2007. Spatial and temporal variability of titanomagnetite placer deposits on a predominately black sand beach. Marine Geology 236, 45-59.

Broecker, W.S., Toggweiler, J.R., and Takahaski, T., 1980. The Bay of Bengal – A major nutrient source for the deep Indian Ocean. Earth and Planetary Science Letters 49, 506-512.

Burdige, D.J., 2005. Burial of terrestrial organic matter in marine sediments: A re-assessment. Global Biogeochemical Cycles 19, doi:10.1029/2004GB002368.

Burns, S.J., Fleitman, D., Mudelsee, M., Neff, U., Matter, A., and Mangini, A., 2002. A 780-year annually resolved record of Indian Ocean monsoon precipitation from a speleothem from south Oman. Journal of Geophysical Research 107, 4434, doi:10.1029/2001JD001281.

Burton, K.W., and Vance, D., 2000. Glacial-interglacial variations in the neodymium isotope composition of seawater in the Bay of Bengal recorded by planktonic foraminifera. Earth and Planetary Science Letters 176, 425-441.

Butler, R.F., 1992. Paleomagnetism: magnetic domains to geologic terranes. Blackwell Scientific. Oxford. 238 p.

Caley, T., Malaizé, B., Zaragosi, S., Rossignol, L., Bourget, J., Eynaud, F., Martinez, P., Giradeau, J., Charlier, K., Ellouz-Zimmerman, N., 2011. New Arabian Sea records help decipher orbital timing of Indo-Asian monsoon. Earth and Planetary Science Letters 308, 433-444.

Canfield, D.E., and Berner, R.A, 1987. Dissolution and pyritization of magnetite in anoxic marine sediments. Geochimica et Cosmochimica Acta 51, 645-659.

Canfield,D.E., Raiswell, R., and Bottrell, S., 1992. The reactivity of sedimentary iron minerals toward sulfide. American Journal of Science 292, 659-683.

Canfield, D.E., 1994. Factors influencing organic carbon preservation in marine sediments. Chemical Geology 114, 315-329.

Canfield, D.E., 1997. The geochemistry of river particulates from the continental USA: major elements. Geochimica et Cosmochimica Acta 61, 3349-3365.

Carvajal, C., Steel, R., and Petter, A., 2009. Sediment supply: The main driver of shelf-margin growth. Earth-Science Reviews 96, 221-248.

Cavani, L., Ciavatta, C., Gessa, C., 2003. Identification of organic matter from peat, leonardite, and lignite fertilisers using humification parameters and electrofocusing. Bioresource Technology 86, 45-52.

Cawthern, T., Johnson, J., Giosan, L., Flores, J.A., and Rose, K., this issue. A Mid-Late Pliocene Biogenic Silica Crash in the Andaman Sea: Potential Teleconnections to the Pacific and Atlantic Oceans. Journal of Marine and Petroleum Geology

Chakrapani, G.J., and Subramanian, V., 1990a. Preliminary studies on the geochemistry of the Mahanadi River basin, India. Chemical Geology 81, 541-253.

Chakrapani, G.J., and Subramanian, V., 1990b. Factors controlling sediment discharge in the Mahanadi River basin, India. Journal of Hydrology 117, 169-185.

Chamov, N.P., and Murdmaa, I.O., 1995. Coarse fraction minerals of sands in the Cascadia margin sediments. In Carson, B., Westbrook, G.K., Musgrave, R.J., and Suess, E. (Eds.), Proceedings of the Ocean Drilling Program, Scientific Results 146, 33-43.

Chao, W.C., 2000. Multiple Quasi Equilibria of the ITCZ and the origin of monsoon onset. Journal of the Atmospheric Sciences 57, 641-651.

Chao, W.C., and Chen, B., 2001. The origin of monsoons. Journal of the Atmospheric Sciences 58, 3497-3507.

Chauhan, O.S., 2003. Past 20,000-year history of Himalayan aridity: Evidence from oxygen isotope records in the Bay of Bengal, Current Science 84, 90-93.

Charles, C.D., Cobb, K., Moore, M.D., Fairbanks, R.G., 2003. Monsoon/tropical ocean interaction in a network of coral records spanning the 20th century. Marine Geology 201, 207–222.

Chesner, C.A., Rose, W.I., Deino, A., Drake, R., and Westgate, J.A., 1991. Eruptive history of Earth's largest Quaternary caldera (Toba, Indonesia) clarified. Geology 19, 200-203.

Chen, J., Chen, Y., Liu, L., Ji, J., Balsam, W., Sun, Y., and Lu, H., 2006. Zr/Rb ratio in the Chinese loess sequences and its implication for changes in the East Asian winter monsoon strength. Geochimica et Cosmochimica Acta 70, 1471-1482.

Childers, A.R., Whitledge, T.E., and Stockwell, D.A., 2005. Seasonal and interannual variability in the distribution of nutrients and chlorophyll a across the Gulf of Alaska shelf: 1998-2000. Deep-Sea Research II 52, 193-216.

Chung, F.H., 1974. Quantitative interpretation of X-ray diffraction patterns of mixtures. I. Matrix-flushing method for quantitative multicomponent analysis. Journal of Applied Crystallography 7, 519-525.

Clemens, S.C., and Prell, W.L., 1990. Late Pleistocene variability of Arabian Sea Summer monsoon winds and continental aridity: Eolian records from the lithogenic component of deep-sea sediments. Paleoceanography 5, 109-145.

Clemens, S.C., and Prell, W.L., 1991. One million year record of summer monsoon winds and continental aridity from the Owen Ridge (Site 722), northwest Arabian Sea. In: Prell, W.L., Niitsuma, N., et al., 1991. Proceedings of the Ocean Drilling Program, Scientific Results 117, 365-388.

Clemens, S.C., and Oglesby, R.J., 1992. Interhemispheric moisture transport in the Indian Ocean summer monsoon: Data-model and model-model comparisons. Paleoceanography 5, 633-643.

Clemens, S.C., and Prell, W.L., 2007. The timing of orbital-scale Indian monsoon changes. Quaternary Science Reviews 26, 275-278.

Clemens, S. C., Prell, W.L., Sun, Y., Liu, Z. and Chen, G., 2008. Southern Hemisphere forcing of Pliocene δ^{18}O and the evolution of Indo-Asian monsoons. Paleoceanography 23, PA4210, doi:10.1029/2008PA001638.

Clemens, S. C., Prell, W.L., and Sun, Y., 2010. Orbital-scale timing and mechanisms driving Late Pleistocene Indo-Asian summer monsoons: Reinterpreting cave speleothem δ^{18}O. Paleoceanography. 25, PA4207, doi:10.1029/2010PA001926.

Clift, P.D., and Gaedicke, C., 2002. Accelerated mass flux to the Arabian Sea during the middle to late Miocene. Geology 30, 207-210.

Clift, P.D., Layne, G.D., Blusztajn, J., 2004. The erosional record of Tibetan uplift in the East Asian marginal seas. In P.D. Clift, P. Wang, D. Hayes, W. Kuhnt (Eds.) Continent–Ocean Interactions in the East Asian Marginal Seas, American Geophysical Union Monograph Series 149, pp. 255-282.

Clift, P.D., 2006. Controls on the erosion of Cenozoic Asia and the flux of clastic sediment to the ocean. Earth and Planetary Science Letters 241, 571-580.

Clift, P.D., Giosan, L., Blisztajn, Campbell, I.H., Allen, C., Pringle, M., Tabrez, A.R., Danish, M., Rabbani, M.M., Alizai, A., Carter, A., and Lückge, A., 2008. Holocene erosion of the Lesser Himalaya triggered by intensified summer monsoon. Geology 36, 79-82.

Clift, P.D., and Giosan, L., in press. Sediment fluxes and buffering in the post-glacial Indus Basin. Basin Research doi:10.1111/bre.12038

Colin, C., Kissel, C., Blamart, D., and Turpin, L., 1998. Magnetic properties of sediments in the Bay of Bengal and the Andaman Sea: impact of rapid North Atlantic Ocean climate events on the strength of the Indian monsoon. Earth and Planetary Science Letters 160, 623-635.

Colin, C., Turpin, L., Bertaux, J., Desprairies, A., and Kissel, C., 1999. Erosional history of the Himalayan and Burman ranges during the last two glacial-interglacial cycles. Earth and Planetary Science Letters 171, 647-660.

Colin, C., Turpin, L., Blamart, D., Frank, N., Kissel, C., and Duchamp, S., 2006. Evolution of weathering patterns in the Indo-Burman Ranges over the last 280 kyr: Effects of sediment provenance on $^{87}Sr/^{86}Sr$ ratios tracer. Geochemistry Geophysics Geosystems 7, Q03007, doi:10.1029/2005GC000962.

Collett T.S., Riedel M., Cochran J.R., Boswell R., Presley J., Kumar P., Sathe A., Sethi A., Lall M., Sibal V., NGHP Expedition 01 Scientists, 2008. National Gas Hydrate Program Expedition 01 initial reports. Directorate General of Hydrocarbons, New Delhi.

Courtillot, V., Besse, J., Vandamme, D., Montigny, R., Jaeger, J.-J., and Capetta, H., 1986. Deccan flood basalts at the Cretaceous/Tertiary boundary? Earth and Planetary Science Letters 80, 361-374.

Croudace, I.W., Rindby, A., and Rothwell, R.G., 2006. ITRAX: description and evaluation of a new mult-function X-ray core scanner. In Rothwell, R.G., New Techniques in Sediment Core Analysis. Geological Society of London Special Publications. 267, 51-63.

Cullen, J.L., 1981. Microfossil evidence for changing salinity patterns in the Bay of Bengal over the last 20,000 years. Palaeogeography, Palaeoclimatology, Palaeoecology 35, 315-356.

Curray, J.R., Emmel, F.J., and Moore, D.G., 2003. The Bengal Fan: morphology, geometry, stratigraphy, history, and processes. Marine and Petroleum Geology, 19, 1191-1223.

Curry, W.B., Ostermann, D.R., Guptha, M.V.S. and Ittekkot, V., 1992. Foraminiferal production and monsoonal upwelling in the Arabian Sea: evidence from sediment traps. Geological Society, London, Special Publications 64, 93-106

Davidson, E.A. Verchot, L.V., Cattânio, J.H., Ackerman, I.L., and Carvalho, J.E.M., 2000. Effects of soil water content on soil respiration in forests and cattle pastures of eastern Amazonia. Biogeochemistry 48, 53-69.

DeMaster, D.J., 1981. The supply and accumulation of silica in marine sediments. Geochimica et Cosmochimica Acta 45, 1715-1732.

Dekkers, M.J., Passier, H.F., and Schoonen, M.A.A., 2000. Magnetic properties of hydrothermally synthesized greigite (Fe_3S_4). II. High- and low-temperature characteristics. Geophysics Journal International 141, 809–819.

deMenocal, P., Bloemendal, J., and King, J., 1991. A rock-magnetic record of monsoonal dust deposition to the Arabian Sea: Evidence for a shift in the mode of deposition at 2.4 Ma. In: Prell, W.L., Niitsuma, N., et al., 1991. Proceedings of the Ocean Drilling Program, Scientific Results 117, 389-407.

Ding, Z.L., Yang, S.L., Sun, J.M., Liu, T.S., 2001. Iron geochemistry of loess and red clay deposits in the Chinese Loess Plateau and implications for long-term Asian monsoon evolution in the last 7.0 Ma. Earth and Planetary Science Letters 185, 99–109.

Doh, S.-J., King, J.W., and Leinen, M.,1988. A rock-magnetic study of Giant Piston Core LL44-GPC from the Central North Pacific and its paleoceanographic significance. Paleoceanography, 3, 89-111.

Dubinsky, E.A., Silver, W.L., and Firestone, M.K., 2010. Tropical forest soil microbial communities couple iron and carbon biogeochemistry. Ecology 91, 2604-2612

Dugan, B., and Sheahan, T.C., 2012. Offshore sediment overpressures of passive margins: Mechanisms, measurement, and models. Reviews of Geophysics RG3001, doi:10.1029/2011RG000379.

Dutta, K., Bhushan, R., and Somayajulu, B.L.K., 2001. ΔR correction values for the Northern Indian Ocean. Radiocarbon 43, 483-488.

Dykoski, C.A., Edwards, R.L., Cheng, H., Yuan, D., Cai, Y., Zhang, M., Lin, Y., Qing, J., An, Z., and Revenaugh, J., 2005. A high-resolution, absolute-dated Holocene and deglacial Asian monsoon record from Dongge Cave, China. Earth and Planetary Science Letters 233, 71-86.

Dypvik, H., and Harris, N.B., 2001. Geochemical facies analysis of fine-grained siliciclastics using Th/U, Zr/Rb, and (Zr+Rb)/Sr ratios. Chemical Geology 181, 131-146.

Emeis, K.-C., Anderson, D.M., Doose, H., Kroon, D., and Schulz-Bull, D., 1995. Sea-surface temperatures and the history of monsoon upwelling in the northwest Arabian Sea during the last 500,000 years. Quaternary Research 43, 355-361.

Emerson, S., Stump, C., Grootes, P.M., Stuvier, M., Farwell, G.W., and Schmidt, F., 1987. Estimates of degradable organic carbon in deep-sea surface sediments from ^{14}C concentrations. Nature 329, 51-53.

Enzel, Y., Ely, L.L., Mishra, S., Ramesh, R., Amit, R., Lazar, B., Rajaguru, S.N., Baker, V.R., and Sandler, A., 1999. High-resolution Holocene environmental changes in the Thar Desert, northwestern India. Science 284, 125-128.

Erselcuk, M., 1947. Iron and steel industry in Japan. Economic Geography 23, 105-129.

Eshel, G., Levy, G.J., Mingelgrin, U., and Singer, M.J., 2004. Critical evaluation of the use of laser diffraction for particle-size distribution analysis. Soil Science Society of America Journal 68, 736-743.

Expedition 311 Scientists, 2006. Site U1325. In Riedel, M., Collett, T.S., Malone, M.J., and the Expedition 311 Scientists. Proc. IODP, 311: Washington, DC (Integrated Ocean Drilling Program Management International, Inc.). doi:10.2204/iodp.proc.311.103.2006

Expedition 337 Scientists, 2013. Site C0020. In Inagaki, F., Hinrichs, K.-U., Kubo, Y., and the Expedition 337 Scientists, Proc. IODP, 337: Tokyo (Integrated Ocean Drilling Program Management International, Inc.). doi:10.2204/iodp.proc.337.103.2013

Fairbanks, R.G., 1989. A 17,000-year glacio-eustatic sea level record: influence of glacial melting rates on the Younger Dryas event and deep-ocean circulation. Nature 342, 637-641.

Fan, S.-M., Moxim, W.J., and Levy II, H., 2006. Aeolian input of bioavailable iron to the ocean. Geophysical Research Letters 33, L07602, doi:10.1029/2005GL024852.

Feng, X., Cui, H., Tang, H., and Conkey, L.E., 1999. Tree-ring δD as an indicator of Asian Monsoon intensity. Quaternary Research 51, 262-266.

Fleitmann, D., Burns, S.J., Mangini, A., Mudelsee, M., Kramers, J., Villa, I., Neff, U., Al-Subbary, A.A., Buettner, A., Hippler, D., and Matter, A., 2007. Holocene ITCZ and Indian monsoon dynamics recorded in stalagmites from Oman and Yemen (Socotra). Quaternary Science Reviews 26, 170-188.

Fontugne, M.R., and Duplessy, J.-C., 1986. Variations of the monsoon regime during the quaternary: Evidence from carbon isotopic record of organic matter in north Indian Ocean sediment cores. Palaeogeography, Palaeoclimatology, Paleoecology 56, 69-88.

France-Lanord, C., and Derry, L.A., 1994. δ^{13}C of organic carbon in the Bengal Fan: Source evolution and transport of C3 and C4 plant carbon to marine sediments. Geochimica et Cosmochimica Acta. 58, 4809-4814.

Fralick, P.W., and Kronberg, B.I., 1997. Geochemical discrimination of clastic sedimentary rock sources. Sedimentary Geology 113, 111–124.

Freeman, K.H., and Colarusso, L.A., 2001. Molecular and isotopic records of C4 grassland expansion in the Late Miocene. Geochimica et Cosmochimica Acta. 65, 1439-1454.

Frihy, O.E., 1994. Discrimination of accreted and eroded coasts using heavy mineral compositions of the Nile Delta beach sands, Egypt. Sedimentology 41, 905–912.

Froelich,P.N., Klinkhammer, G.P., Bender, M.L., Luetke, N.A., Heath, G.R., Cullen, D., Dauphin, P., Hammond, D., Hartman, B., and Maynard, V., 1979. Early oxidation of organic matter in pelagic sediments of the eastern equatorial Atlantic: suboxic diagenesis. Geochimica et Cosmochimica Acta 43, 1075-1090.

Fu, Y., von Dobeneck, T., Franke, C., Heslop, D., and Kasten, S., 2008. Rock magnetic identification and geochemical process models of greigite formation in Quaternary marine sediments from the Gulf of Mexico (IODP Hole U1319A). Earth and Planetary Science Letters 275, 233-245.

Fuhrer, K., Wolff, E.W., and Johnsen, S.J., 1999. Timescales for dust variability in the Greenland Ice Core Project (GRIP) ice core in the last 100,000 years. Journal of Geophysical Research 104, 31043-31052.

Fuloria, R.C., 1993. Geology and hydrocarbon prospects of Mahanadi Basin, India. In: Biswas, S.K., et al. (Eds.), Proceedings of Second Seminar on Petroliferous Basins of India, vol. 1. Indian Petroleum Publishers, Dehra Dun, India, pp. 355–369.

Furukawa, Y., Barnes, H.L., 1995. Reactions forming pyrite from precipitated amorphous ferrous sulfide. In: Vairavamurthy, M.A., Schoonen, M.A.A. (Eds.), Geochemical Transformation of Sedimentary Sulfur. ACS Symposium Series 612, 194–205

Gadgil, S., 2003. The Indian monsoon and its variability. Annual Review of Earth and Planetary Sciences 31, 429-467.

Galy, V., Francois, L., France-Lanord, C., Faure, P., Kudrass, H., Palhol, F., and Singh, S.K., 2008. C4 plants decline in the Himalyan Basin since the Last Glacial Maximum. Quaternary Science Reviews. 27, 1396-1409.

Gardner, J.V., and Dartnell, P., 1995. Centennial-scale Late Quaternary stratigraphies of carbonate and organic carbon from the Santa Barbara Basin, Hole 893A, and their paleoceanographic significance. In Kennett, J.P., Baldauf, J.G, and Lyle, M. (Eds.) Proceedings of the Ocean Drilling Program Scientific Results. 146 (Pt. 2), 103-124.

Gardner, J.V., Dean, W.E., and Dartnell, P., 1997. Biogenic sedimentation beneath the California Current system for the past 30 kyr and its paleoceanographic significance. Paleoceanography 12, 207-225.

Garming, J.F.L., Bleil, U., and Riedinger, N., 2005. Alteration of magnetic mineralogy at the sulfate-methane transition: Analysis of sediments from the Argentine continental slope. Physics of the Earth and Planetary Interiors 151, 290-308

Gauns, M., Madhupratap, M., Ramaiah, N., Jyothibabu, R., Fernandes, V., Paul, J.T., and Kumar, S.P., 2005. Comparative accounts of biological productivity characteristics and estimates of carbon fluxes in the Arabian Sea and the Bay of Bengal. Deep Sea Research Part II 52, 2003-2017.

Geological Survey of Japan, AIST (ed.). 2012. Seamless digital geological map of Japan 1: 200,000. Jul 3, 2012 version. Research Information Database DB084, Geological Survey of Japan, National Institute of Advanced Industrial Science and Technology.

Goldfinger, C., Nelson, C.H., Morey, A.E., Johnson, J.E., Patton, J., Karabanov, E., Gutierrez-Pastor, J., Eriksson, A.T., Gracia, E., Dunhill, G., Enkin, R.J., Dallimore, A., and Vallier, T., 2012, Turbidite event history—Methods and implications for Holocene paleoseismicity of the Cascadia subduction zone: U.S. Geological Survey Professional Paper 1661–F, 170 p, 64 figures, available at http://pubs.usgs.gov/pp/pp1661/f

Gomes, H.R., Goes, J.I., and Saino, T., 2000. Influence of physical processes and freshwater discharge on the seasonality of phytoplankton regime in the Bay of Bengal. Continental Shelf Research 20, 313-330.

Gonzalez-Vila, F.J., Martin, F., Del Rio, J.C., and Fründ, R., 1992. Structural characteristics and geochemical significance of humic acids isolated from three Spanish lignite deposits. The Science of the Total Environment 117/118, 335-343.

Gonzalez-Vila, F.J., del Rio, J.C., Almendros, G., and Martin F., 1994. Structural relationship between humic fractions from peat and lignites from the Miocene Granada basin. Fuel 73, 215-221.

Goñi, M.A., Ruttenberg, K.C., and Eglinton, T.I., 1998. A reassessment of the sources and importance of land-derived organic matter in surface sediments from the Gulf of Mexico. Geochimica Cosmochimica Acta 62, 3055-3075.

Goodbred, Jr., S.L., and Kuehl, S.L., 2000. Enormous Ganges-Brahmaputra sediment discharge during strengthened early Holocene monsoon. Geology 28, 1083-1086.

Govil, P., and Naidu, P.D., 2010. Evaporation-precipitation changes in the eastern Arabian Sea for the last 68 ka: Implications on monsoon variability. Paleoceanography 25, PA1210, doi:10.1029/2008PA001687.

Govil, P., and Naidu, P.D., 2011. Variations of Indian monsoon precipitation during the last 32 kyr reflected in the surface hydrography of the Western Bay of Bengal. Quaternary Science Reviews 30, 3871-3879.

Greinert, J., Bohrmann, G., Suess, E., 2001. Gas hydrate-associated carbonates and methane-venting at Hydrate Ridge: Classi¢cation, distribution, and origin of authigenic lithologies. In: Paull, C.K., Dillon, W.P. (Eds.), Natural Gas Hydrates: Occurrence, Distribution, and Detection. AGU Geophysical Monograph 124, 99-113.

Guo, Z., Peng, S., Hao, Q., Biscaye, P.E., An, Z., and Liu, T., 2004. Late Miocene-Pliocene development of Asian aridification recorded in the Red-Earth Formation in northern China. Global and Planetary Change 41, 135-145.

Gupta, A.K., Anderson, D.M., and Overpeck. J.T., 2003. Abrupt changes in the Asian southwest monsoon during the Holocene and their links to the North Atlantic Ocean. Nature 421, 354-357.

Gupta, A.K., Mohan, K., Sarkar, S., Clemens, S.C., Ravindra, R., and Uttam, R.K., 2011. East-West similarities and differences in the surface and deep northern Arabian Sea records during the past 21 kyr. Palaeogeography, Palaeoclimatology, Palaeoecology 301, 75-85.

Gupta, S.R., and Singh, J.S., 1981. Soil respiration in a tropical grassland. Soil Biology and Biochemistry 13, 261-268.

Gupta, L.P., Subramanian, V., and Ittekkot, V., 1997. Biogeochemistry of particulate organic matter transported by the Godavari River, India. Biogeochemistry 38, 103-128.

Guptha, M.V.S., Curry, W.B., Ittekkot, V., and Muralinath, A.S., 1997. Seasonal variation in the flux of planktic foraminifera: Sediment trap results from the Bay of Bengal, Northern Indian Ocean. Journal of Foraminiferal Research 27, 5-19.

Hall, F.R., and King, J.W., 1989. Rock-magnetic stratigraphy of Site 645 (Baffin Bay) from ODP Leg 105. In, Srivastava, S.P., Arthur, M., Clement, B., et al., Proceedings of the Ocean Drilling Program, Scientific Results 105, 843-859.

Hall, J.M., and Smeltzer, D., 1980. Paleomagnetism of sediments, Sites 438 and 440, Deep Sea Drilling Project. Initial Reports of the Deep Sea Drilling Project 57, 1159-1166.

Hall, F.R., and King, J.W., 1989. Rock-magnetic stratigraphy of Site 645 (Baffin Bay) from ODP Leg 105. In, Srivastava, S.P., Arthur, M., Clement, B., et al., Proceedings of the Ocean Drilling Program, Scientific Results 105:843-859.

Hedges, J.I., Keil, R.G., and Benner, R., 1997. What happens to terrestrial organic matter in the ocean? Organic Geochemistry 27, 195-212.

Heeschen, K. U., A. M. Tréhu, R. W. Collier, E. Suess, and G. Rehder, 2003. Distribution and height of methane bubble plumes on the Cascadia margin characterized by acoustic imaging. Geophysical Research Letters 30(12), 1643, doi:10.1029/2003GL016974.

Heeschen, K. U., R. W. Collier, M. A. de Angelis, E. Suess, G. Rehder, P. Linke, and G. P. Klinkhammer, 2005. Methane sources, distributions, and fluxes from cold vent sites at Hydrate Ridge, Cascadia Margin, Global Biogeochemical Cycles 19, GB2016, doi:10.1029/2004GB002266.

Heier, K.S., and Billings, G.K., 1970. Rubidium. In: Wedepohle, K.H. (Ed.), Handbook of Geochemistry, Vol. 2. Springer-Verlag, Berlin/Heidelberg, pp. 37B1–37K3.

Hensen, C., Zabel, M., Pfeifer, K., Schwenk, T., Kasten, S., Riedinger, N., Schulz, H.D., and Boetius, A., 2003. Control of sulfate pore-water profiles by sedimentary events and the significance of anaerobic oxidation of methane for the burial of sulfur in marine sediments. Geochimica et Cosmochimica Acta 67, 2631-2647.

Hepp, D.A., Mörz, T., Hensen, C., Frederichs, T., Kasten, S., Riedinger, N., and Hay, W.F., 2009. A late Miocene-early Pliocene Antarctic deepwater record of repeated iron reduction events. Marine Geology 266, 198-211.

Hermelin, J.O.R., and Shimmield, G.B., 1995. Impact of productivity events on the benthic fauna in the Arabian Sea over the last 150,000 years. Paleoceanography 10, 85-116.

Hinrichs, K.-U., Hayes, J.M., Sylva, S.P., Brewer, P.G., and Delong, E.F., 1999. Methane-consuming archeabacteria in marine sediments. Nature 398, 802-805.

Hoehler, T.M., Alperin, M.J., Albert, D.B., and Martens, C.S., 1994. Field and laboratory studies of methane oxidation in an anoxic marine sediment – evidence for a methanogen-sulfate reducer consortium. Global Biogeochemical Cycles 8, 451-463.

Holligan, P.M., Fernández, E., Aiken, J., Balch, W.M., Boyd, P., Burkill, P.H., Finch, M., Groom, S.B., Malin, G., Muller, K., Purdie, D.A., Robinson, C., Trees, C.C., Turner, S.M., and van der Wal, P., 1993. A biogeochemical study of the coccolithophore Emiliania huxleyi, in the North Atlantic. Global Biogeochemical Cycles 7, 879-900.

Hong, W.-L., Solomon, E.A., and Torres, M., this issue. A kinetic-model approach to quantify the effect of mass transport deposits on pore water profiles in the Krishna-Godavari Basin, Bay of Bengal. Marine and Petroleum Geology

Hoshi, H., and Teranishi, Y., 2007. Paleomagnetism of the Ishikoshi Andesite: a middle Miocene paleomagnetic pole for northeastern Japan and tectonic implications. Earth Planets Space 59, 871-878.

Housen, B.A., and Musgrave, R. J., 1996. Rock-magnetic signature of gas hydrates in accretionary prism sediments. Earth and Planetary Science Letters 139, 509-519.

Hughes, M.K., Wu, X.D., Shao, X.M., Garfin, G.M., 1994. A preliminary reconstruction of rainfall in North-Central China since AD 1600 from tree-ring density and width. Quaternary Research 42, 88–99.

Hughes, M.G., Keene, J.B., and Joseph, R.G., 2000. Hydraulic sorting of heavy-mineral grains by swash on a medium-sand beach. Journal of Sedimentary Research 70, 994-1004.

Hunger, S., and Benning, L.G., 2007. Greigite: a true intermediate on the polysulfide pathway to pyrite. Geochemical Transactions 8,1 doi:10.1186/1467-4866-8-1.

Hunt, C. P., Moskowitz, B. M. and Banerjee, S. K., 1995. Magnetic Properties of Rocks and Minerals. In Ahrens, T.J. (Ed.) Rock Physics & Phase Relations: A Handbook of Physical Constants. American Geophysical Union, Washington, D. C.. doi: 10.1029/RF003p0189

Ibarra, J.V., and Juan, R., 1985. Structural changes in humic acids during the coalification process. Fuel 64, 650-656.

Imbrie, J., Hays, J.D., Martinson, D.G., McIntyre, Mix, A.C., Morely, J.J., Pisias, N.G., Prell, W.L., and Shackleton, N.J., 1984. The orbital theory of Pleistocene climate: Support from a revised chronology of the marine δ^{18}O record. *In* Milankovitch and Climate Part I, (Berger, A.L., et al., Eds.) pp. 269-305.

Inagaki, F., Hinrichs, K.-U., Kubo, K., Bowles, M.W., Heuer, V.B., Hong, W.-L., Hoshino, T., Ijiri, A., Imachi, H., Ito, M., Kaneko, M., Lever, M.A., Lin, Y.-S., Methé, B.A., Morita, S., Morono, Y., Tanikawa, W., Bihan, M., Bowden, S., Elvert, M., Glombitza, C., Gross, D., Harrington, G., Hori, T., Li, K., Limmer, D., Liu, C., Murayama, M., Ohkouchi, N., Park, Y-S., Phillips, S.C., Prieto-Mollar, X., Purkey, M., Riedinger, N., Sanada, Y., Sauvage, J., Snyder, G., Susilawati, R., Takano, Y., Tasumi, E., Terada, T., Tomaru, H., Trembath-Reichert, E., and Yamada, Y., in press. Exploring the bottom of the deep biosphere ~2.5 km below the seafloor. Science 349, 420-424.

Ittekkot, V., Safiullah. S.,and Arain, R., 1986. Nature of organic matter in rivers with deep sea connections: The Ganges-Brahmaputra and Indus. The Science of the Total Environment 58, 93-107.

Jicha, B.R., Hart, G.L., Johnson, C.M., Hildreth, W., Beard, B.K., Shirley, S.B., and Valley, J.W., 2009. Isotopic and trace element constraints on the petrogenesis of lavas from Mount Adams volcanic field, Washington. Contributions to Mineralogy and Petrology 157, 189-207.

Johnson, J.E., Solway, D., Disenhof, C., Torres, M.E., Hong, W-L., Rose, K., 2010a. Identifying slope failure deposits from a potentially mixed magnetic susceptibility signal in gas hydrate bearing regions. Fire in the Ice, National Energy Technology Laboratory Methane Hydrate Newsletter. http://www.netl.doe.gov/technologies/oil-gas/publications/Hydrates/Newsletter/MHNews_2011_01.pdf

Johnson, J.E., Torres, M.E., Hong, W.-L., Disenhof, C., Miranda, E., Rose, K., 2010b. Slope Failure Records in Gas Hydrate Bearing Regions of the Cascadia Margin. Abstract OS53A-1370 presented at 2010 Fall Meeting, AGU, San Francisco, Calif., 13-17 Dec

Johnson J.E., Phillips, S.C., Giosan, L., and Clyde, W.C., in prep. Decoupling detrital and diagenetic components in gas hydrate bearing sediments.

Johnson, J.E., Phillips, S.C., Torres, M.E., Pinero, E., Rose, K.K., and Giosan, L, this issue. Influence of total organic carbon deposition on the inventory of gas hydrate in the Indian continental margins. Journal of Marine and Petroleum Geology

Just, J., M. J. Dekkers, T. vonDobeneck, A. vanHoesel, and T. Bickert, 2012. Signatures and significance of aeolian, fluvial, bacterial and diagenetic magnetic mineral fractions in Late Quaternary marine sediments off Gambia, NW Africa. Geochemistry Geophysics Geosystems, 13, Q0AO02, doi:10.1029/2012GC004146.

Jyothibabu, R., Madhu, N.V., Maheswaran, P.A., Jayalakshmy, K.V., Nair, K.K.C., and Achuthankutty, C.T., 2008. Seasonal variation of microzooplankton (20-200 μm) and its possible implication on the vertical carbon flux in the western Bay of Bengal. Continental Shelf Research 28, 737-755.

Kanamatsu, T., and Niitsuma, N., 2004. Rock magnetism and paleomagnetic stratigraphy of forearc sediments of the Japan Trench, ODP Sites 1150 and 1151. The Island Arc 13, 180-190.

Kanamatsu, T., Parés, J.M. and Kitamura, Y., 2012. Pliocene shortening direction in Nankai Trough off Kumano, southwest Japan, Sites IODP C0001 and C0002, Expedition 315: Anisotropy of magnetic susceptibility analysis for paleostress. Geochemistry Geophysics Geosystems 13, Q0AD22, doi:10.1029/2011GC003782

Kaneko, M., Shingai, H., Pohlman, J.W., and Narakoa, H., 2010. Chemical and isotopic signature of bulk organic matter and hydrocarbon biomarkers within mid-slope accretionary sediments of the northern Cascadia margin gas hydrate system. Marine Geology 275, 166-177.

Karlin, R., and Levi, S., 1985. Geochemical and sedimentological control of magnetic properties of hemipelagic sediments. Journal of Geophysical Research 90, 10373-10392.

Karlin, R., Lyle, M., and Heath, G.R., 1987. Authigenic magnetite formation in suboxic marine sediments. Nature 326, 490-493.

Karlin, R., 1990. Magnetite diagenesis in marine sediments from the Oregon continental margin. Journal of Geophysical Research 95, 4405-4419

Karlin, R.E., and Abella, S.E.B., 1996. A history of Pacific Northwest earthquakes recorded in Holocene sediments from Lake Washington. Journal of Geophysical Research 101, 6137-6150.

Kars, M., and K. Kodama, 2015. Authigenesis of magnetic minerals in gas hydrate-bearing sediments in the Nankai Trough, offshore Japan. Geochemistry Geophysics Geosystems 16, 947–961, doi:10.1002/2014GC005614.

Kasten, S., Freudenthal, T., Gingele, F.X., and Schulz, H.D., 1998. Simultaneous formation of iron-rich layers at different redox boundaries in sediments of the Amazon deep-sea fan. Geochimica et Cosmochimica Acta 62, 2253-2264.

Kempton, H., and Atkins, D., 2009. Direct measurement of sulfide mineral oxidation rates and acid rock drainage in wall rock of open pit mines. 8th International Conference on Acid Rock Drainage, Skellefteå, Sweden, June 23-26, 2009.

Kim, J.-H., and Lee, Y.-J., 2009. Data report: elemental, Rock-Eval, and isotopic compositions of bulk sediments, IODP Expedition 311. In Riedel, M., Collett, T.S., Malone, M.J., and the Expedition 311 Scientists, Proc. IODP, 311:doi:10.2204/iodp.proc.311.207.2009

Kirby, M.E., Domack, E.W., and McClennen, C.E., 1998. Magnetic stratigraphy and sedimentology of Holocene glacial marine deposits in the Palmer Deep, Bellingshausen Sea, Antarctica: implications for climate change? Marine Geology 152, 247-259.

Kirschvink, J.L., and Chang, S.-B.R., 1984. Ultrafine magnetite in deep-sea sediments: Possible bacterial magnetofossils. Geology 12, 559-562.

Komar, P.D., 1989, Physical processes of waves and currents and the formation of marine placers: Reviews in Aquatic Sciences 1, 393–423.

Konert, M., and Vandenberghe, J., 1997. Comparison of laser grain size analysis with pipette and sieve analysis: a solution for the underestimation of the clay fraction. Sedimentology 44, 523-535.

Konhauser K.O., Newman D.K., Kappler A. (2005) The potential significance of microbial Fe(III) reduction during deposition of Precambrian banded iron formations. Geobiology 3, 167–177.

Kostka, J.E., and Nealson, K.H., 1995. Dissolution and reduction of magnetite by bacteria. Environmental Science and Technology 29, 2535-2540.

Kowalenko, C.G., and Babuin, D., 2013. Inherent factors limiting the use of laser diffraction for determining particle size distributions of soil and related samples. Geoderma 193-194, 22-28.

Krishna, M.S., Naidu, S.A., Subbaiah, Ch.V., Sarma, V.V.S.S., and Reddy, N.P.C., 2013. Distribution and sources of organic matter in surface sediments of the eastern continental margin of India. Journal of Geophysical Research 118, 1484-1494.

Krishnamurthy, V., and Goswami, B.N., 2000. Indian monsoon-ENSO relationship on interdecadal timescale. Journal of Climate 13, 579-595.

Kroon, D., Steens, T., and Troelstra, S.R., 1991. Onset of monsoonal related upwelling in the Western Arabian Sea as revealed by planktonic foraminifers. In Prell, W.L., Niitsuma, N. et. al. (Eds.) Proceedings of the Ocean Drilling Program, Scientific Results 117, 257-263.

Kruiver, P.P., Dekkers, M.J., and Heslop, D., 2001. Quantification of magnetic coercivity components by analysis of acquisition curves of isothermal remanent magnetization. Earth and Planetary Science Letters 189, 269-276.

Kukla, G., Heller, F., Liu, X.-M., Chun, X.-T., Liu, T.-S., An, Z.-S., 1988. Pleistocene climates in China dated by magnetic susceptibility. Geology 16, 811–814.

Kudrass, H.R., Hofmann, A., Doose, H., Emeis, K., and Erlenkeuser, H., 2001. Modulation and amplification of climatic changes in the Northern Hemisphere by the Indian summer monsoon during the past 80 k.y. Geology 29, 63-66.

Kumar, N., Gwiazda, N., Anderson, R.F., and Froelich, P.N., 1993. ^{231}Pa/^{230}Th ratios in sediments as a proxy for past changes in southern Ocean productivity. Nature 362, 45-47.

Kumar, K.K., Rajagopalan, B., and Cane, M.A., 1999. On the weakening relationship between the Indian Monsoon and ENSO. Science 284, 2156-2159.

Kumar, A.A., Rao, V.P., Patil, S.K., Kessarkar, P.M., and Thamban, M., 2005. Rock magnetic records of the sediments of the eastern Arabian Sea: Evidence for late Quaternary climatic change. Marine Geology 220, 59-82.

Kutzbach, J.E., 1981. Monsoon climate of the early Holocene: Climate experiment with the earth's orbital parameters for 9000 years ago. Science 214, 59-61.

Lambert, F., Delmonte, B., Petit, J.R., Bigler, M., Kaufmann, P.R., Hutterli, M.A., Stocker, T.F., Ruth, U., Steffensen, and Maggi, V., 2008. Dust-climate couplings over the past 800,000 years from the EPICA Dome C ice core. Nature 452, 616-619.

Larrasoaña, J.C., Gràcia, E., Garcés, M., Musgrave, R.J., Piñero, E., Martínez-Ruiz, F., and Vega, M.E., 2006. Rock magnetic identification of magnetic iron sulfides and its bearing on the occurrence of gas hydrates, ODP Leg 204 (Hydrate Ridge). In Tréhu, A.M., Bohrmann, G., Torres, M.E., and Colwell, F.S. (Eds.), Proceedings of the Ocean Drilling Program, Scientific Results, 204: College Station, TX (Ocean Drilling Program), 1–33. doi:10.2973/odp.proc.sr.204.111.2006

Larrasoaña, J.C., Roberts, A.P., Musgrave, R.J., Gràcia, E., Piñero, E., Vega, M., and Martínez-Ruiz, F., 2007. Diagenetic formation of greigite and pyrrhotite in gas hydrate marine sedimentary systems. Earth and Planetary Science Letters, v. 261, p. 350-366.

Lean, C.M.B., and McCave, I.N., 1998. Glacial to interglacial mineral magnetic and paleoceanographic changes at Chatham Rise, SW Pacific Ocean. Earth and Planetary Science Letters 163, 247-260.

Lisiecki, L.E., and Raymo, M.E., 2005. A Pliocene-Pleistocene stack of 57 globally distributed benthic $\delta^{18}O$ records. Paleoceanography 20, PA1003, doi:10.1029/2004PA001071.

Liu, K.-K., Chao, S.-Y., Shaw, P.-T., Gong, G.-C., Chen, C.-C., and Tang, T.Y., 2002. Monsoon-forced chlorphyll distribution and primary production in the South China Sea: observations and a numerical study. Deep-Sea Research I 49,1387-1412.

Liu, X., and Flemings, P.B., 2006. Passing gas through the hydrate stability zone at southern Hydrate Ridge, offshore Oregon, Earth and Planetary Science Letters, 241. 211-226.

Liu, Q., Roberts, A.P., Larrasoaña, J.C., Banerjee, S.K., Guyodo, Y., Tauxe, L., and Oldfield, F., 2012. Environmental magnetism: Principles and applications. Reviews of Geophysics 50, RG4002.

Livingstone, D.A., 1963. Chemical composition of rivers and lakes. U.S. Geological Survey Professional Paper 440-G.

Loizeau, J.-L., Arbouille, D., Santiago, S., and Vernet, J.-P., 1994. Evaluation of a wide range laser diffraction grain size analyzer for use with sediments. Sedimentology 41, 353-361.

Long, P.E., and Wood, B.J., 1986. Structures, textures, and cooling histories of Columbia River basalt flows. Geological Society of America Bulletin, 97, 1114-1155.

Lovely, D.R., Coates, J.D., Blunt-Harris, E.L., Phillips. E.J.P., and Woodward, J.C., 1996. Humic substances as electron acceptors for microbial respiration. Nature 382, 445-448.

Lovely, D.R., 1991. Dissimilatory Fe(III) and Mn(IV) reduction. Microbiological Reviews 55, 259-287.

Lowrie, W., and Heller, F., 1982. Magnetic properties of marine limestones. Reviews of Geophysics and Space Physics 20, 171-192.

Lynn, R.J., and Simpson, J.J., 1987. The California Current system: the seasonal variability and its physical characteristics. Journal of Geophysical Research 92, 12947-12966.

Madhu, N.V., Jyothibabu, R., Maheswaran, P.A., Gerson, V.J., Gopalakrashnan, T.C., and Nair, K.K.C., 2006. Lack of seasonality in phytoplankton standing stock (chlorophyll-a) and production in the western Bay of Bengal. Continental Shelf Research 26, 1868-1883.

Madhupratap, M., Gauns, M., Ramaiah, N., Kumar, S.P., Muraleedharan, P.M., de Sousa, S.N., Sardessai, S., and Muraleedharan, U., 2003. Biogeochemsitry of the Bay of Bengal: physical, chemical and primary productivity characteristics of the central and western Bay of Bengal during the summer monsoon 2001. Deep Sea Research Part II 50, 881-896.

Maher, B.A., and Thompson, R., 1995. Paleorainfall reconstructions from pedogenic magnetic susceptibility variations in the Chinese loess and paleosols. Quaternary Research 44, 383-391.

Maher, B.A., Prospero, J.M., Mackie, D., Gaiero, D., Hesse, P.P., and Balkanski, Y., 2010. Global connections between Aeolian dust, climate, and ocean biogeochemistry at the present day and the last glacial maximum. Earth-Science Reviews 99, 61-97.

Mahesh, B.S., and Banakar, V.K., 2014. Change in the intensity of low-salinity water inflow from the Bay of Bengal into the Eastern Arabian Sea from the Last Glacial Maximum to the Holocene: Implications for monsoon variations. Palaeogeography Palaeoclimatology Palaeoecology 397, 31-37.

Mahowald, N., Kohfeld, K., Hansson, M., Balkanski, Y., Harrison, S.P., Prentice, I.C., Schulz, M., and Rodhe, H., 1999. Dust sources and deposition during the last glacial maximum and current climate: A comparison of model results with paleodata from ice cores and marine sediments. Journal of Geophysical Research 104, 15895-15916.

Mahowald, N. M., Baker, A. R. Bergametti, G., Brooks, N., Duce, R.A., Jickells, T.D., Kubilay, N. J., Prospero, J.M., and Tegen, I., 2005. Atmospheric global dust cycle and iron inputs to the ocean. Global Biogeochemical Cycles 19, GB4025, doi:10.1029/2004GB002402.

Mantyla, A.W., and Reid, J.L., 1995. On the origins of deep and bottom waters of the Indian Ocean. Journal of Geophysical Research 100, 2417-2439.

Mallik, T.K., Vasudevan, V., Aby Verghese, P., and Machado, T., 1987. The black sand placer deposits of Kerala Beach, southwest India. Marine Geology 77, 129-150.

Martínez-García, A., Sigman, D.M., Ren, H., Anderson, R.F., Straub, M., Hodell, D.A., Jaccard, S.L., Eglinton, T.I., and Haug, G.H., 2014. Iron fertilization of the subantarctic ocean during the last ice age. Science 343 1347-1350.

Martinson, D.G., Pisias, N.G., Hays, J.D., Imbrie, J., Moore, T.C., and Shackleton, N.J., 1987. Age dating and the orbital theory of the ice ages: Development of a high-resolution 0 to 300,000 year chronostratigraphy. Quaternary Research. 27:1-29.

Mayewski, P.A., Meeker, L.D., Twickler, M.S., Whitlow, S.I., Yang, Q., Lyons, W.B., and Prentice, M., 1997. Major features and forcing of high-latitude northern hemisphere atmospheric circulation using a 110,000-year-long glaciochemical series. Journal of Geophysical Research 102, 26345-26366.

Mazumdar, A., Dewangan, P., Joäo, H.M., Peketi, A., Khosla, V.R., Kocherla, M., Badesab, F.K., Joshi, R., Roxanne, P., Ramamurty, P.B.S., Karisiddaiah, M., Patil, D.J., Dayal, A.M., Hawkesworth, C.J., Avanzinelli, R., Ramprasad, T., 2009. Evidence of paleo cold seep activity from the Bay of Bengal, offshore India. Geochemistry, Geophysics, Geosystems 10, 1–15.

Mazumdar, A., João, H.M., Peketi, A., Dewangan, P., Kocherla, M., Joshi, R.K., and Ramprasad, T., 2012. Geochemical and geological constraints on the composition of marine sediment pore fluid: Possible link to gas hydrate deposits. Marine and Petroleum Geology 38, 35-52.

Mazumdar, A., Peketi, A., Joao, H.M., Dewangan, P., and Ramprasad, T., 2014. Pore-water chemistry of sediment cores off Mahanadi Basin, Bay of Bengal: Possible link to deep seated methane hydrate deposit. Marine and Petroleum Geology 49, 162-175.

McCave, I.N., Bryant, R.J., Cook, H.F., and Coughanowr, C.A., 1986. Evaluation of a laser-diffraction-size analyzer for use with natural sediments. Journal of Sedimentary Petrology 56, 561-564.

McCreary, J.P., Han, W., Shankar, D., and Shetye, S.R., 1996. Dynamics of the East India Coastal Current 2. Numerical solutions. Journal of Geophysical Research 101, 13993-14010.

McHugh, C.M.G., Gurung, D., Giosan, L., Ryan, W.B.F., Mart, Y., Sancar, U., Burckle, L. and Cagatay, M.N., 2008. The last reconnection of the Marmara Sea (Turkey) to the World Ocean: A paleoceanographic and paleoclimatic perspective. Marine Geology 255, 64–82.

McNichol, A. P., Gagnon, A.R., Osborne, E.A., Hutton, D.L., Von Reden, K.F., and R. J. Schneider, 1995. Improvements in procedural blanks at NOSAMS: Reflections of improvements in sample preparation and accelerator operation. Radiocarbon 37, 683–691.

Mehta, V.M., and Lau, K.-M., 1997. Influence of solar irradiance on the Indian monsoon-ENSO relationship at decadal-multidecadal time scales. Geophysical Research Letters 24, 159-162.

Meyers, P.A., 1994. Preservation of elemental and isotopic source identification of sedimentary organic matter. Chemical Geology 114, 289-302.

Milliman, J.D., and Meade, R.H., 1983. World-wide delivery of river sediment to the oceans. Journal of Geology. 91, 1-21.

Milucka, J., Ferdelman, T.G., Polerecky, L., Franzke, D., Wegener, G., Schmid, M., Lieberwirth, I., Wagner, M., Widdel, F., and Kuypers, M.M.M., 2012. Zero-valent sulphur is a key intermediate in marine methane oxidation. Nature doi:10.1038/nature11656ro

Mohanty, R.B., and Panda, T., 2011. Soil respiration and microbial population in a tropical forest soil of Orissa, India. Flora 206, 1040-1044.

Molnar, P., England, P., and Martinod, J., 1993. Mantle dynamics, uplift of the Tibetan plateau, and the Indian monsoon. Reviews of Geophysics 31, 357-396.

Morrill, C., Overpeck, J.T., Cole, J.E., Liu, K.-b., Shen, C., and Tang, L., 2006. Holocene variations in the Asian monsoon inferred from the geochemistry of lake sediments in central Tibet. Quaternary Research 65, 232-243.

Mortlock, R.A., Froelich, P.N., 1989. A simple method for the rapid determination of biogenic opal in pelagic marine sediments. Deep-Sea Research 36, 1415-1426.

Müller, P.J., 1977. C/N ratios in Pacific deep-sea sediments: Effect of inorganic ammonium and organic nitrogen compounds sorbed by clays. Geochimica Cosmochimica Acta 41, 765-776.

Müller, P.J., and Suess, E., 1979. Productivity, sedimentation rate, and sedimentary organic matter in the oceans - I. Organic carbon preservation. Deep-Sea Research 26A, 1347-1362.

Musgrave, R.J., and Hiroki, Y., 2000. Rock magnetism of the diapir sites (Sites 991, 992, 993 and 996), Carolina Rise and Blake Ridge. In Paul, C.K., et al., Proceedings of the Ocean Drilling Program. 164, 401-409.

Musgrave, R.J., Bangs, N.L., Larrasoaña, J.C., Gràcia, E., Hollamby, J.A., and Vega, M.E., 2006. Rise of the base of the gas hydrate zone since the last glacial recorded by rock magnetism. Geology 34, 117-120.

Nealson, K.H., and Saffarini, D., 1994. Iron and manganese in anaerobic respiration: Environmental significance, physiology, and regulation. Annual Review of Microbiology 48, 311-343.

Neretin, L.N., Böttcher, M.E., Jørgensen, B.B. Volkov, I.I., Lüschen, H., and Higenfeldt, K., 2004. Pyritization processes and greigite formation in the advancing sulfidization front in the Upper Pleistocene sediments of the Black Sea. Geochimica et Cosmochimica Acta 68, 2081-2093.

Nesbitt, H.W., and Young, G.M., 1982. Early Proterozoic climates and plate motions inferred from major element chemistry of lutites. Nature 299, 715-717.

Nie, J., King, J.W., and Fang, X., 2008. Tibetan uplift intensified the 400 k.y. signal in paleoclimate records at 4 Ma. Geological Society of America Bulletin 120, 1338-1344.

Niitsuma N., 1986. Paleomagnetic resuls, Nankai Trough and Hapan Trench, Deep Sea Drilling Project Leg 87. Initial Reports of the Deep Sea Drilling Project 87, 757-786.

Nilsson, A., Lee Y.S., Snowball, I., and Hill, M., 2013. Magnetostratigraphic importance of secondary chemical remanent magnetizations carried by greigite (Fe_3S_4) in Miocene sediments, New Jersey shelf (IODP Expedition 313). Geosphere 9, 510-520.

Novosel, I., Spence, G.D., and Hyndman, G.D., 2005. Reduced magnetization produced by increased methane flux at a gas hydrate vent. Marine Geology 216, 265-274.

Nuncio, M., and Prasanna Kumar, S., 2012. Life cycle of eddies along the western boundary of the Bay of Bengal and their implications. Journal of Marine Systems 94, 9-17.

Ohba, T., Kimura, Y., and Fujimaki, H., 2007. High-magnesian andesite produced by two-stage magma mixing: a case study from Hachimantai, northern Honshu, Japan. Journal of Petrology 48, 627-645.

Oppo, D.W. and Sun, Y., 2005. Amplitude and timing of sea-surface temperature change in the northern South China Sea: Dynamic link to the East Asian monsoon. Geology, 33, 785-788.

Orchard, V.A., and Cook, F.J., 1983. Relationship between soil respiration and soil moisture. Soil Biology and Biochemistry 15, 447-453.

Owen, L.A., Finkel, R.C., and Caffee, M.W., 2002. A note on the extent of glaciation throughout the Himalaya during the global Last Glacial Maximum. Quaternary Science Reviews 21, 147-157.

Paul, J.T., Ramaiah, N., Gauns, M., and Fernandes, V., 2007. Preponderance of a few diatom species among the highly diverse microphytoplankton assemblages in the Bay of Bengal. Marine Biology 152, 63-75.

Pedersen, T.F., 1983. Increased productivity in the eastern equatorial Pacific during the last glacial maximum (19,000 – 14,000 yr BP). Geology 11, 16-19.

Peketi, A., Mazumdar, A., Joshi, R.K., Patil, D.J., Srinivas, P.L., and Dayal., A.M., 2012. Tracing the paleo sulfate-methane transition zones and H_2S seepage events in marine sediments: An application of C-S-Mo systematics. Geochemistry Geophysics Geosystems 13, Q10007, doi:10/1029/2012GC004288.

Peters, C., and Dekkers, M.J., 2003. Selected room temperature magnetic parameters as a function of mineralogy, concentration and grain size. Physics and Chemistry of the Earth 28, 659-667.

Peterson, L.C., and Prell, W.L., 1985. Carbonate dissolution in recent sediments of the eastern equatorial Indian Ocean: Preservation patterns and carbonate loss above the lysocline. Marine Geology 64, 259-290.

Peterson, T.D., Whitney, F.A., and Harrison, P.J., 2005. Macronutrient dynamics in an anticyclonic mesoscale eddy in the Gulf of Alaska. Deep Sea Research II, 52, 909-932.

Phillips, S.C., Johnson, J.E., Miranda, E., and Disenhof, C., 2011. Improving CHN measurement in carbonate-rich marine sediments. Limnology and Oceanography: Methods 9, 194-203.

Phillips, S.C., Johnson, J.E., Underwood, M.B., Guo, J., Giosan, L., and Rose, K. , 2014a. Bulk and clay mineral composition of sediments in the Bay of Bengal, Andaman Sea, and Arabian Sea recovered during NGHP Expedition 01. Marine and Petroleum Geology

Phillips, S.C., Johnson, J.E., Giosan, L., and Rose, K., 2014. Monsoon-influenced variation in productivity and lithogenic sediment flux since 110 ka in the offshore Mahanadi Basin, northern Bay of Bengal. Marine and Petroleum Geology 58A, 502-525, doi:10.1016/j.marpetgeo.2014.05.007.

Pilson. M.E.Q., 1998. An Introduction to the Chemistry of the Sea. 2nd Ed. Cambridge University Press. 529 p.

Ponton, C., Giosan, L., Eglinton, T.I., Fuller, D.Q., Johnson, J.E., Kumar, P., and Collett, T.S., 2012. Holocene aridification of India. Geophsical Research Letters, 39, L03704, doi:10.1029/2011GL050722.

Posamentier, H.W., Jervey, M.T., and Vail, P.R., 1988. Eustatic controls on clastic deposition I: Conceptual framework. In Wilgus, C.K., et al. (Eds.) Sea level changes: an integrated approach. Society of Economic Paleontologists and Mineralogists Special Publication 42, 109-124.

Potrema, J.T., Luther, M.E., and O'Brien, J.J., 1991. The seasonal circulation of the Upper Ocean in the Bay of Bengal. Journal of Geophysical Research 96, 12667-12683.

Poulton, S.W., Krom, M.D., and Raiswell, R., 2004. A revised scheme for the reactivity of iron (oxyhydr)oxide minerals towards dissolved sulfide. Geochimica et Cosmochimica Acta 68, 3703-3713.

Prassana Kumar, S., Muraleedharan, P.M., Prasad, T.G., Gauns, M., Ramaiah, N., de Souza, S.N., Sardesai, S., and Madhupratap, M., 2002.Why is the Bay of Bengal less productive during summer monsoon compared to the Arabian Sea? Geophysical Research Letters 29: DOI: 10.1029/2002GL016013

Prassana Kumar, S., Nuncio, M., Narvekar, J., Kumar, A., Sardesai, de Souza, S.N., Gauns, M., Ramaiah, N., and Madhupratap, M., 2004. Are eddies nature's trigger to enhance biological productivity in the Bay of Bengal? Geophysical Research Letters 31, L07309, doi:10.1029/2003GL019274

Prassana Kumar, S., Nuncio, M., Ramaiah, N., Sardesai, S., Narvekar, J., Fernandes, V., and Paul J.T., 2007. Eddy-mediated biological productivity in the Bay of Bengal during fall and spring intermonsoons. Deep-Sea Research I 54, 1619-1640.

Prahl, F.G., Ertel, J.R., Goñi, M.A., Sparrow, M.A., and Eversmeyer, B., 1994. Terrestrial organic carbon contributions to sediments on the Washington margin. Geochimica et Cosmochimica Acta 58, 3035-3048.

Prell, W.L., Hutson, W.H., Williams, D.F., Bé, A.W.H., Geitzenauer, K., and Molfino, B., 1980. Surface circulation of the Indian Ocean during the Last Glacial Maximum, approximately 18,000 yr BP. Quaternary Research 14, 309-336.

Prell, W., and Kutzbach, 1987. Monsoon variability over the past 150,000 years. Journal of Geophysical Research 92, 8411-8425.

Pruysers, P.A., de Lange, G.J., Middleburg, J.J., and Hydes, D.J., 1993. The diagenetic formation of metal-rich layers in sapropel-containing sediments in the eastern Mediterranean. Geochimica et Cosmochimica Acta 57, 527-536.

Pye, K., Dickson, J.A.D., Schiavon, N., Coleman, M.L., and Cox, M., 1990. Formation of siderite-Mg-calcite-iron sulphide concretions in intertidal marsh and sandflat sediments, north Norfolk, England. Sedimentology 37, 325-343.

Pyzik, A.J., and Sommer, S.E., 1981. Sedimentary iron monosulfides: Kinetics and mechanism of formation. Geochimica et Cosmochimica Acta 45, 687-698.

Quade, J., and Cerling, T.E., 1995. Expansion of C_4 grasses in the Late Miocene of northern Pakistan: evidence from stable isotopes in paleosols. Palaeogeography, Palaeoclimatology, Palaeoecology 115, 91-116.

Quinton, E.E., Dahms, D.E., and Geiss, C.E., 2011. Magnetic analyses of soils from Wyoming, constrain rates and pathways of magnetic enhancement for soils from semiarid climates. Geochemistry Geophysics Geosystems Q07Z30 doi:10.1029/2011GC003728.

Rakshit, S., Uchimiya, M., and Sposito, G., 2009. Iron(III) bioreduction in soil in the presence of added humic substances. Soil Science Society of America Journal 73, 65-71.

Rahaman, W., Singh, S.K., Sinha, R., and Tandon, S.K., 2009. Climate control on erosion distribution over the Himalaya during the past ~100 ka. Geology 37, 559-562.

Raich, J.W., and Schleshinger, W.H., 1992. The global carbon dioxide flux in soil respiration and its relationship to vegetation and climate. Tellus 44B, 81-99.

Ramaswamy, V., and Rao, P.S., 2006. Grain size analysis of sediments from the northern Andaman Sea: Comparison of laser diffraction and sieve-pipette techniques. Journal of Coastal Research 22, 1000-1009.

Rao, D.G., Krishna, K.S., and Sar., D., 1997. Crustal evolution and sedimentation history of the Bay of Bengal since the Cretaceous. Journal of Geophysical Research 102, 17747-17768.

Rashid, H., Flower, B.P., Poore, R.Z., and Quinn, T.M., 2007. A ~25 ka Indian Ocean monsoon variability record from the Andaman Sea. Quaternary Science Reviews 26, 2586-2597.

Rashid, H., England, E., Thompson, L., and Polyak, L., 2011. Late glacial to Holocene Indian summer Monsoon variability based upon sediment records taken from the Bay of Bengal. Terrestrial Atmospheric and Oceanic Sciences 22, 215-228.

Raymo, M.E., and Ruddiman, W.F., 1992. Tectonic forcing of late Cenozoic climate. Nature 359, 117-122.

Razjigaeva, N.G., and Naumova, V.V., 1992. Trace element composition of detrital magnetite from coastal sediments of northwestern Japan Sea for provenance study. Journal of Sedimentary Research 62, 802-809.

Reeburgh, 1976. Methane consumption in Cariaco Trench waters and sediments. Earth and Planetary Science Letters 47, 345-352.

Reichart, G.J., Lourens, L.J., and Zachariasse, W.J., 1998. Temporal variability in northern Arabian Sea Oxygen Minimum Zone during the last 225,000 years. Paleoceanography 13, 607-621.

Reimer, P.J., Baillie, M.G.L., Bard, E., Bayliss, A., Bech, J.W., Blackwell, P.G., Bronk Ramsey, C., Buck, C.E., Burr, G.S., Edwards, R.L., Friedrich, M., Grootes, P.M., Guilderson, T.P., Hajdas, I., Heaton, T.J., Hogg, A.G., Hughen, K.A., Kaiser, K.F., Kromer, B., McCormac, F.G., Manning, S.W., Reimer, R.W., Richards, D.A., Southon, J.R., Talamo, S., Turney, C.S.M., van der Plicht, J., and Weyhenmeyer, C.E., 2009. Intcal09 and Marine09 radiocarbon age calibration curves, 0-50,000 years cal BP. Radiocarbon 51, 1111-1150.

Richter T.O., Lassen, S., van Weering, T.C.E., and de Haas, H., 2001. Magnetic susceptibility patterns and provenance of ice-rafted material at Feni Drift, Rockall Trough: implications for the history of the British-Irish ice sheet. Marine Geology 173, 37-54.

Riedinger, N., Pfeifer, K., Kasten, S., Garming, J.F.L., Vogt, C., and Hensen, C., 2005. Diagenetic alteration of magnetic signals by anaerobic oxidation of methane related to a change in sedimentation rate. Geochimica et Cosmochimica Acta. 69, 4117-4126.

Riedinger, N., Formolo, M. J., Lyons, T. W., Henkel, S., Beck, A. and Kasten, S., 2014. An inorganic geochemical argument for coupled anaerobic oxidation of methane and iron reduction in marine sediments. Geobiology 12, 172–181.

Rickard, D., Schoonen, M.A.A., and Luther, G.W., 1995. Chemistry of iron sulfides in sedimentary environments. In: Vairavamurthy, M.,A., and Schoonen, M.A.A. (Eds.), Geochemical transformations of sedimentary sulfur. ACS Symposium Series 612, Washington, D.C., p. 168-193.

Rickard, D.,and Luther III, G.W., 1997. Kinetics of pyrite formation by the H_2S oxidation of iron(II) monosulfide in aqueous solutions between 25 and 125 °C: The mechanism. Geochimica et Cosmochimica Acta 61, 135-147.

Rickers, K., Mezger, K., and Raith, M.M., 2001. Evolution of the continental crust in the Proterozoic Eastern Ghats Belt, India and new constraints for Rodinia reconstruction: implications from Sm-Nd, Rb-Sr and Pb-Pb isotopes. Precambrian Research 112, 183-210.

Riedinger, N., Pfeifer, K., Kasten, S., Garming, J.F.L., Vogt, C., and Hensen, C., 2005. Diagenetic alteration of magnetic signals by anaerobic oxidation of methane related to a change in sedimentation rate. Geochimica et Cosmochimica Acta 69, 4117-4126.

Ritger, S., Carson, B., and Suess, E. (1987) Methane-derived authigenic carbonates formed by pore-water expulsion along the Oregon/Washington margin. GSA Bulletin 98, 147-156.

Roberson, S., and Weltje, G.J., in press. Inter-instrument comparison of particle-size analysers. Sedimentology.

Roberts, A.P., and Turner, G.M., 1993. Diagenetic formation of ferromagnetic iron sulphide minerals in rapidly deposited marine sediments, South Island, New Zealand. Earth and Planetary Science Letters 115, 257-273.

Roberts, A.P., 1995. Magnetic properties of sedimentary greigite (Fe_3S_4). Earth and Planetary Science Letters 134, 227–236.

Roberts, A.P., Florindo, F., Villa, G., Chang, L., Jovane, L., Bohaty, S.M., Larrasoaña, J.C., Heslop, D., and FitzGerald, J.D., 2011. Magetotactic bacterial abundance in pelagic marine environments is limited by organic carbon flux and availability of dissolved iron. Earth and Planetary Science Letters 310, 441-442.

Robinson, S.G., 1986. The late Pleistocene palaeoclimatic record of North Atlantic deep-sea sediments revealed by mineral-magnetic measurements. Physics of the Earth and Planetary Interiors 42, 22-47.

Ruddiman, W.F., 2006. What is the timing of orbital-scale monsoon changes? Quaternary Science Reviews 25, 657-658.

Ruddiman, W.F., and Kutzbach, J.E., 1989. Forcing of late Cenozoic northern hemisphere climate by plateau uplift in southern Asia and the American West. Journal of Geophysical Research 94, 18409–18427.

Sacks, I.S., and Suyehiro, K., 2003. Leg 186 synthesis: drilling the forearc of the northeast Japan arc—causes and effects of subduction plate coupling over 20 m.y. In Suyehiro, K., Sacks, I.S., Acton, G.D., and Oda, M. (Eds.), Proceedings of the Ocean Drilling Program, Scientific Results, 186:1–27 <http://www-odp.tamu.edu/publications/186_SR/VOLUME/SYNTH/SYNTH.PDF>.

Sager, W.W., and Hall, S.A., 1990. Magnetic properties of black mud turbidites from ODP Leg 116, distal Bengal Fan, Indian Ocean. In Cochran, J.R., Stow, D.A.V., et al. (Eds.) Proceedings of the Ocean Drilling Program, Scientific Results 116, 317-336.

Sakuyama, M., and Nesbitt, R.W., 1986. Geochemistry of the Quaternary volcanic rocks of the northeast Japan Arc. Journal of Volcanology and Geothermal Research 29, 413-450.

Sangode, S.J., Suresh, N., and Bagati, T.N., 2001. Godavari source in the Bengal fan sediments: Results from magnetic susceptibility dispersal pattern. Current Science 80, 660-664.

Sarnthein, M., Winn, K., Duplessy, J.-C., and Fontugne, M.R., 1988. Global variations of surface ocean productivity in low and mid latitudes: influence of CO_2 reservoirs of the deep ocean and atmosphere during the last 21,000 years. Paleoceanography 3, 361-399.

Sarnthein, M., and Winn, K., 1990. Reconstruction of low and middle latitude export productivity, 30,000 years BP to present: implications for global carbon reservoirs. In: M.E. Schelschinger (Ed.) Climate-Ocean interaction, Kluwer, Dordrecht, pp 319-342.

Sastri, V.V., Venkatachala, B.S., and Narayanan, V., 1981. The evolution of the east coast of India. Palaeogeography, Palaeoclimatology, Palaeoecology 36, 23-54.

Sato, H., and Amano, K., 1991. Relationship between tectonics, volcanism, sedimentation, and basin development, Late Cenozoic, central part of Northern Honshu, Japan.

Savage, K.E., and Davidson, E.A., 2001. Interannual variation of soil respiration in two New England Forests. Global Biogeochemical Cycles 15, 337-350.

Schoonen, M.A.A., 2004. Mechanisms of sedimentary pyrite formation. In: Amend, J.P., Edwards, K.J., and Lyons, T.W. (Eds.), Sulfur biogechemistry – past and present. Geological Society of America Special Paper 379, p. 117-134.

Schön, J.H., 2004. Physical Properties of Rocks: Fundamentals and Principles of Petrophysics. Pergamon. 600 p.

Schott, F.A., and McCreary, Jr., J.P., 2001. The monsoon circulation of the Indian Ocean. Progress in Oceanography 51, 1-123.

Schott, F.A., Xie, S.-P., and McCreary, Jr., J.P., 2009. Indian Ocean circulation and climate variability. Reviews of Geophysics 47, RG1002, doi:10.1029/2007RG000245.

Schrader, H., 1992. Coastal upwelling and atmospheric CO_2 changes over the last 400,000 years: Peru. Marine Geology, 107: 239-248.

Schulenberg, S.A., 2011. Reconstructing the variability in the Indian Monsoon from the Last Glacial period to present. M.S. Thesis. University of New Hampshire. 52 pp.

Schulte, S.,and Bard, E., 2003. Past changes in biologically mediated dissolution of calcite above the chemical lysocline recorded in Indian Ocean sediments. Quaternary Science Reviews 22, 1757-1770.

Schulz, H., von Rad, U., and Erlenkeuser, 1998. Correlation between Arabian Sea and Greenland climate oscillations of the past 110,000 years. Nature 393, 54-57.

Segarra, K.E.A, Comerford C., Slaughter J., Joye S.B. (2013) Impact of electron acceptor availability on the anaerobic oxidation of methane in coastal freshwater and brackish wetland sediments. Geochimica et Cosmochimica Acta 115, 15–30.

Sengupta, S., Parekh, A., Chakraborty, S., Ravi Kumar, K., and Bose, T., 2013. Vertical variation of oxygen isotope in Bay of Bengal and its relationships with water masses. Journal of Geophysical Research 118, 6411-6424.

Shetye, S.R., Shenoi, S.S.C., Gouveia, A.D., Michael, G.S., Sundar, D., and Nampoothiri, G., 1991. Wind-driven coastal upwelling along the western boundary of the Bay of Bengal during the southwest monsoon. Continental Shelf Research 11, 1397-1408.

Shetye, S.R. Gouveia, A.D., Shenoi, S.S.C., Sundar, D., Michael, G.S., and Nampoothiri, G., 1993. The Western Boundary Current of the Seasonal Subtropical Gyre in the Bay of Bengal. Journal of Geophysical Research 98, 945-954.

Shipboard Scientific Party, 2003. Site 1249. In Tréhu, A.M., Bohrmann, G., Rack, F.R., Torres, M.E., et al. (Eds.) Proceedings of the Ocean Drilling Program, Initial Reports 204, 1-98. doi:10.2973/odp.proc.ir.204.108.2003

Singh, A.D., Jung, S.J.A., Darling, K., Ganeshram, R., Ivanochko, T., and Kroon, D., 2011. Productivity collapses in the Arabian Sea during glacial cold phases. Paleoceanography 26, PA3210, doi:10.1029/2009PA001923.

Sirocko, F.M., Sarnthein, H., Erlenkeuser, H., Lange, H., Arnold, M., and Duplessy, J.-C., 1993. Century-scale events in monsoonal climate over the past 24,000 years. Nature 364, 322-324.

Sirocko, F., Garbe-Schönberg, D., McIntyre, A. and Molfino, B., 1996. Teleconnections between the subtropical monsoons and high-latitude climates during the last deglaciation. Science 272, 526-529.

Slingerland, R., and Smith, N.D., 1986, Occurrence and formation of water-laid placers: Annual Review of Earth and Planetary Sciences 14, 113–147.

Solomon, E.A., Spivack, A.J., Kastner, M., Torres, M.E., and Robertson, G., this issue. Gas hydrate distribution and carbon sequestration through coupled microbial methanogeneis and silicate weathering in the Krishna-Godavari basin, offshore India. Marine and Petroleum Geology

Smirnov, A.V., and Tarduno, J.A., 2000. Low-temperature magnetic properties of pelagic sediments (Ocean Drilling Program Site 805C): Tracers of maghemetization and magnetic mineral reduction. Journal of Geophysical Research 105, 16457-16471.

Southon, J., Kashgarian, M., Fontugne, M., Metivier, M., and Yim, W.W-S., 2002. Marine reservoir corrections for the Indian Ocean and Southeast Asia. Radiocarbon 44, 167-180.

Sperazza, M., Moore, J.N., and Henrix, M.S., 2004. High-resolution particle size analysis of naturally occurring very fine-grained sediment through laser diffractometry. Journal of Sedimentary Research 74, 736-743.

Stein, R., 1990. Organic carbon content/sedimentation rate relationship and its paleoenvironmental significance for marine sediments. Geo-Marine Letters 10, 37-44.

Stoner, J.S, Channell, J.E., and Hillaire-Marcel, C., 1995. Magnetic properties of deep-sea sediments off southwest Greenland: Evidence for major differences between the last two deglaciations. Geology 23, 241-244.

Strickland, J.D., and Parsons, T.R., 1972. Practical handbook of seawater analysis. Bulletin of the Fisheries Research Board of Canada 167, 311 p.

Stuvier, M., and Reimer, P.J., 1994. Extended ^{14}C database and revised CALIB radiocarbon calibration program. Radiocarbon 35, 215-230.

Suzuki, T., 2008. Analysis of titanomagnetite within weathered middle Pleistocene KMT tephra and its application for fluvial terrace chronology, Kanto Plain, central Japan. Quaternary International 178, 119-127.

Subrahmanyam V., Subrahmanyam A.S., Murty G.P.S., and Murthy K.S.R., 2008. Morphology and tectonics of Mahanadi Basin, northeastern continental margin of India from geophysical studies. Marine Geology 253, 63–72.

Subramanian, V., 1980. Mineralogical input of suspended matter by Indian rivers into the adjacent areas of the Indian Ocean. Marine Geology 36, 29-34.

Suess, E., Torres, M.E., Bohrmann, G., Collier, R.W., Greinert, J., Linke, P., Rehder, G., Tre¤hu, A., Wallmann, K., Winckler, G., Zuleger, 1999. Gas hydrate destabilization: Enhanced dewatering, benthic material turnover and large methane plumes at the Cascadia convergent margin. Earth and Planetary Science Letters 170, 1-15.

Suess, E., Torres, M.E., Bohrmann, G., Collier, R.W., Rickert, D., Goldfinger, C., Linke, P., Heuser, A., Sahling, H., Heeschen, K., Jung, C., Nakamura, K., Greinert, J., Pfannkuche, O., Tréhu, A., Klinkhammer, G., Whiticar, M.J., Eisenhauer, A., Teichert, B., and Elvert, M., 2001. Sea floor methane hydrates at Hydrate Ridge, Cascadia margin. In Paull, C.K., and Dillon, W.P. (Eds.), Natural Gas Hydrates: Occurrence, Distribution, and Detection. American Geophysical Union, Geophysical Monogrograph Series 124, 87–98.

Suits, N.S., and Arthur, M.A., 2000. Sulfur diagenesis and partitioning in Holocene Peru shelf and upper slope sediments. Chemical Geology 163, 219-234.

Svensson, A., Biscaye, P.E., and Grousset, F.E., 2000. Characterization of late glacial continental dust in the Greenland Ice Core Project ice core. Journal of Geophysical Research 105, 4637-4656.

Sweeney, R.E., Kaplan, I.R., 1973. Pyrite framboid formation: laboratory synthesis and marine sediments. Economic Geology 68, 618–634.

Taira, A., and Niitsuma, N., 1986. Turbidite sedimentation in the Nankai Trough as interpreted from magnetic fabric, grain size, and detrital modal analyses. Initial Reports of the Deep Sea Drilling Project 87, 611-632.

Taira, A., 2001. Tectonic evolution of the Japanese island arc system. Annual Review of Earth and Planetary Science 29, 109-134.

Takagi, T., 2004. Origin of magnetite- and ilmenite- series granitic rocks in the Japan Arc. American Journal of Science 304, 169-202.

Talley, L.D., 2013. Hydrographic Atlas of the World Ocean Circulation Experiment (WOCE). Volume 4: Indian Ocean, Sparrow, M., Chapman, P., and Gould, J. (Eds.). International WOCE Project Office, Southhampton, UK.

Tatsumi, Y., Otofuji, Y.-I., Matsuda, T., and Nohda, S., 1989. Opening of the Sea of Japan back-arc basin by asthenospheric injection. Tectonophysics 166, 317-329.

Thauer R.K., and Shima S, 2008. methane as fuel for anaerobic microorganisms. Annals of the New York Academy of Sciences 1125, 158–170.

Thompson, L.G., Yao, T., Mosley-Thompson, E., Davis, M.E., Henderson, K.A., and Lin, P.-N., 2000. A high-resolution millennial record of the South Asian Monsoon from Himalayan ice cores. Science 289, 1916-1919.

Torres, M.E., Mix, A.C., Kinports, K., Haley, B., Klinkhammer, G.P., McManus, J., and de Angelis, M.A., 2003. Is methane venting at the seafloor recorded by δ13C of benthic foraminifera shells? Paleoceanography 18, 1062, doi:10.1029/2002PA000824.

Tréhu, A.M., Flemings, P.B, Bangs, N.L., Chevallier, J., Gràcia, E., Johnson, J.E., Liu, X., Riedel, M., and Torres, M.E., 2004. Feeding methane vents and gas hydrate deposits at south Hydrate Ridge, Geophysical Research Letters 31: L23310, doi:10.1029/2004GL021286

Trentesaux, A., Recourt, P., Bout-Roumazeilles, V., and Tribovillard, N., 2001. Carbonate grain-size distribution in hemipelagic sediments from a laser particle sizer. Journal of Sedimentary Research 71, 858-862.

Tripathy, G.R., Singh, S.K., Bhushan, R., and Ramaswamy, V., 2011. Sr-Nd isotope composition of the Bay of Bengal sediments: Impact of climate on erosion in the Himalaya. Geochemical Journal 175-186.

Tripathy, G.R., Singh, S.K., and Ramaswamy, V., 2014. Major and trace element geochemistry of Bay of Bengal sediments: Implications to provenances and their controlling factors. Palaeogeography Palaeoclimatology Palaeoecology 397, 20-30.

Tsuesue, A., 1962. Genetic considerations of magnetite and pyrrhotite in pyritic deposits, Yanahara District, southwestern Japan. Economic Geology 57, 696-977.

Tudhope, A.W., Lea, D.W., Shimmield, G.B., Chilcott, C.P., Head, S., 1996. Monsoon climate and Arabian Sea coastal upwelling recorded in massive corals from Southern Oman. Palaios 11, 347–361.

Ujike, O., and Tsuchiya, N., 1993. Geochemistry of Miocene basaltic rocks temporally straddling the rifting of the lithosphere at the Akita-Yamagata area, northeast Japan. Chemical Geology 104, 61-74.

Unger, D., Ittekkot, V., Schäfer, P., Tiemann, J., and Reschke, S., 2003. Seasonality and interannual variability of particle fluxes to the deep Bay of Bengal: influence of riverine input and oceanographic processes. Deep Sea Research Part II: Topical Studies in Oceanography 50, 897-923.

Urlaub, M., Zervos, A., Talling, P.J., Masson, D.G., and Clayton, C.I., 2012. How do ~2° slopes fail in areas of slow sedimentation? A sensitivity study on the influence of accumulation rate and permeability on submarine slope stability, in: Yamada, Y. et al. (Eds), Submarine Mass Movements and Their Consequences, Advances in Natural and Technological Hazards Research 31, pp. 277-287.

Vail, P.R., Mitchum, R.M., and Thompson, S., 1977. Seismic stratigraphy and global changes of sea level Part 3, Relative changes in sea level from coastal onlap. In Payton, C.E., (Ed.) Seismic stratigraphy: applications to hydrocarbon exploration. American Association of Petroleum Geologists Memoir 26, 63-81.

Vanderaveroet, P., Averbuch, O., Deconinck, J.-F., and Chamley, H., 1999. A record of glacial/interglacial alternations in Pleistocene sediments off New Jersey expressed by clay mineral, grain-size and magnetic susceptibility data. Marine Geology 159, 79-92.

Varkey, M.J., Murty, V.S.N., and Suryanarayana, A., 1996. Physical oceanography of the Bay of Bengal and the Andaman Sea. Oceanography and Marine Biology: an Annual Review 34, 1-70.

Verosub, K.L., and Roberts, A.P., 1995. Environmental magnetism: Past, present, and future. Journal of Geophysical Research 100, 2175-2192.

Versteegh, G.J.M., and Zonneveld, K.A.F., 2002. Use of selective degradation to separate preservation from productivity. Geology 7, 615-618.

Vidya, P.J., and Prasanna Kumar S., in press. The role of mesoscale eddies on the variability of biogenic flux in the northern and central Bay of Bengal. Journal of Geophysical Research doi: 10.1002/j2013JC009060

Vigliotti, L., 1997. Magnetic properties of light and dark sediment layers from the Japan Sea: Diagenetic and paleoclimatic implications. Quaternary Science Reviews 16, 1093-1114.

Vinayachandran, P.N., Matsumoto, Y., Mikawa, T., and Yamagata, T., 1999. Intrusion of the Southwest Monsoon Current into the Bay of Bengal. Journal of Geophysical Research 104, 11077-11085.

Vinayachandran, P.N., and Mathew, S., 2003. Phytoplankton bloom in the Bay of Bengal during the monsoon and its intensification by cyclones. Geophysical Research Letters 30, 1572, doi:10.1029/2002GL016717

Von Huene, R., Langseth, M., Nasu, N., and Okada, H., 1982. A summary of Cenozoic tectonic history along the IPOD Japan Trench transect. Geological Society of America Bulletin, 93:829-846.

Wang, B., Wu, R., and Lau, K.-M., 2001. Interannual variability of the Asian summer monsoon: contrasts between the Indian and the Western North Pacific-East Asian monsoons. Jounral of Climate 14, 4073-4090.

Wang, Y.J., Cheng, H., Edwards, R.L., An, Z.S., Wu, J.Y., Shen, C.-C., and Dorale, J.A., 2001. A high-resolution absolute-dated Late Pleistocene monsoon record from Hulu Cave, China. Science 294, 2345-2348.

Wang, B., and Ho, L., 2002. Rainy season of the Asian-Pacific summer monsoon. Journal of Climate 15, 386-398.

Wang, B., Clemens, S.C., and Liu, P., 2003. Contrasting the Indian and East Asian monsoons: implication on geologic timescales. Marine Geology 201, 5-21.

Wang, P., Clemens, S., Beaufort, L., Braconnot, P., Ganssen, G., Jian, Z., Kershaw, P., and Sarnthein, M., 2005. Evolution and variability of the Asian monsoon system: state of the art and outstanding issues. Quaternary Science Reviews 24, 595-629.

Wang, Y., Cheng, H., Edwards, R.L., Kong, X., Shao, X., Chen, S., Wu, J., Jiang, X., Wang, X., and An, Z., 2008. Millenial- and orbital-scale changes in the East Asian monsoon over the past 224,000 years. Nature 451, 1090-1093.

Weber, M.E., Wiedicke, M.H., Kudrass, H.R., Hübscher, C., and Erlenkeusker, H., 1997. Active growth of the Bengal Fan during sea-level rise and highstand. Geology 25, 315-318.

Wei, K., and Gasse, F., 1999. Oxygen isotopes in lacustrine carbonates of West China revisited: implications for post glacial changes in summer monsoon circulation. Quaternary Science Reviews 18,1315–1334.

Wentworth, C.K., 1922. A scale of grade and class terms for clastic sediments. Journal of Geology 30, 377-392.

Werner, M., Tegen, I., Harrison, S.P., Kohfeld, K.E., Prentice, I.C., Balkanski, Y., Rodhe, H., and Roelandt, C., 2002. Seasonal and interannual variability of the mineral dust cycle under present and glacial climate conditions. Journal of Geophysical Research 107, 4744, doi:10.1029/2002JD002365.

Westgate, J.A., Shane, P., Pearce, N.J.G., Perkins, W.T., and Korisettar, R., 1998. All Toba tephra occurrences across peninsular India belong to the 75,000 yr B.P. eruption. Quaternary Research 50, 107-112.

Wilkin, R.T., and Barnes, H.L., 1996. Pyrite formation by reactions of iron monosulfides with dissolved inorganic and organic sulfur species. Geochimica et Cosmochimica Acta 60, 4167-4179.

Wolff, E.W., Fisher, H., Fundel, F., Ruth, U., Twarloh, B., Littot, G.C., Mulvaney, R., Röthlisberger, R., de Angelis, M., Boutron, C.F., Hansson, M., Jonsell, U., Hutterli, M.A.,Lambert, F., Kaufmann, P., Stauffer, B., Stocker, T.F., Steffensen, J.P., Bigler, M., Siggaard-Andersen, M.L., Udisti, R., Becagli, S., Castellano, E., Severi, M., Wagenbach, D., Barbante, C., Gabrielli, P., and Gaspari, V., 2006. Southern Ocean sea-ice extent, productivity and iron flux over the past eight glacial cycles. Nature 440, 491-496.

Xiao, J.L., Porter, S.C., An, Z.S., Kumai, H., Yoshikawa, S., 1995. Grain size of quartz as an indicator of winter monsoon strength on the Loess Plateau of central china during the last 130,000 yr. Quaternary Research 43, 22–29.

Xu, W., Peacor, D.R., Dollase, W.A., Van Der Voo, R., and Beaubouef, R., 1997. Transformation of titanomagnetite to titanomaghemite: A slow, two-step oxidation-ordering process in MORB. American Mineralogist 82, 1101-1110.

Yamaji, A.,1990. Rapid intra-arc rifting in Miocene northeast Japan. Tectonics 9, 365-378.

Yamazaki, T., Abdeldayem, A.L., and Ikehara, K., 2003. Rock-magnetic changes with reduction diagenesis in Japan Sea sediments and preservation of geomagnetic secular variation in inclination during the last 30,000 years. Earth, Planets, and Space 55, 327-340.

Yoshida, T., 2001. The evolution of arc magmatism in the NE Honshu Arc, Japan. Tohoku Geophysics Journal 36, 131-149.

You, Y., 1998. Intermediate water circulation and ventilation of the Indian Ocean derived from water-mass contributions. Journal of Marine Research 56, 1029-1067.

Yu, L., O'Brien, J., and Yang, J., 1991. On the remote forcing of the circulation in the Bay of Bengal. Journal of Geophysical Research 96, 20449-20454.

Zachos, J., Pagani, M., Sloan, L., Thomas, E., and Billups, K., 2001. Trends, rhythms, and aberrations in global climate 65 Ma to Present. Science 292, 686-693.

Zhao, K., Wang, Y., Edwards, R.L., Cheng, H., and Liu, D., 2010. High-resolution stalagmite δ18O records of Asian monsoon changes in central and southern China spanning the MIS 3/2 transition. Earth and Planetary Science Letters 298, 191-198.

Ziegler, M., Jilbert, T., de Lange, G.J., Lourens, L.J., Reichart, G.J., 2008. Bromine counts from XRF scanning as an estimate of the marine organic carbon content of sediment cores. Geochemisty Geophysics Geosystems 9, Q05009, doi:10.1029/2007GC001932.

Ziegler, M., Lourens, L.J., Tuenter, E, Hilgen, F., Reichart, G.-J.,and Weber, N., 2010. Precession phasing offset between Indian summer monsoon and Arabian Sea productivity linked to changes in Atlantic overturning circulation. Paleoceanography 25, PA3213, doi:10.1029/2009PA001884.

Zhao, X., Oda, H., Wu, H., Yamamoto, T., Yamamoto, Y., Yamamoto, Y., Nakajima, T., Kitamura, Y., and Kanamatsu, T., 2013. Magnetostratigraphic results from sedimentary rocks of IODP's Nankai Trough Seismogenic Zone Experiment (NanTroSEIZE) Expedition 322. In Jovane, L., Herrero-Bervera, E., Hinnov, L. A. & Housen, B. A. (eds) Magnetic Methods and the Timing of Geological Processes. Geological Society, London, Special Publications, 373